Summer 2018

Grain refinement of high alloy stainless steels in sand and directionally solidified castings

Dustin Alan Arvola

Recommended Citation

Arvola, Dustin Alan, "Grain refinement of high alloy stainless steels in sand and directionally solidified castings" (2018). *Masters Theses*. 7793.
https://scholarsmine.mst.edu/masters_theses/7793

GRAIN REFINEMENT OF HIGH ALLOY STAINLESS STEELS IN SAND AND DIRECTIONALLY SOLIDIFIED CASTINGS

by

DUSTIN ALAN ARVOLA

A THESIS

Presented to the Faculty of the Graduate School of the

MISSOURI UNIVERSITY OF SCIENCE AND TECHNOLOGY

In Partial Fulfillment of the Requirements for the Degree

MASTER OF SCIENCE IN METALLURGICAL ENGINEERING

2018

Approved by

Ronald J. O'Malley, Advisor
Simon N. Lekakh
Laura N. Bartlett

PUBLICATION THESIS OPTION

This thesis contains three manuscripts prepared for a conference proceeding and two for journal publication in the style specified by Missouri University of Science and Technology:

Paper I: Pages 48-73 were submitted and accepted for presentation at AISTech in May 2018.

Paper II: Pages 74-108 are currently under review for publication in the International Journal of Metalcasting (IJMC).

Paper III: Pages 109-143 are currently under review for publication in Journal of Materials Engineering and Performance (JMEP).

ABSTRACT

The goal of this research project is to develop an industrially viable melting process that will control the crystallization macrostructure of austenitic grades of cast steels. Titanium nitride (TiN) has proven to be an effective grain refiner of austenite. Theoretical simulation and experimental application has led to the development of a repeatable grain refining melt process for austenitic stainless steel alloys.

Grain refinement of the as-cast structure of *Cr-Ni* stainless steel alloys solidified with primary *FCC, BCC* and dual *FCC/BCC* phases was studied experimentally. Refinement was achieved in both cast ferritic and austenitic grades. Dual solidification of *FCC/BCC* phases resulted in an unrefined macrostructure. It is proposed that solidification sequence can limit the grain refining capability of heterogeneous nuclei.

Two inoculation-based melt practices were developed to study grain refinement in cast austenitic stainless steels. The first includes *in-situ* formation of TiN on to *Mg-Al* spinel oxides, and the second involves master alloy additions containing preformed TiN. The master alloy method extended the equiaxed zone and improved the distribution of TiN in the casting. The *in-situ* method showed more effective grain size refinement.

The effect of the developed grain refining melt practice on the properties of cast superaustenitic stainless steel (similar to *CK3MCuN*) was examined. Heat treatment had no effect on the as-cast grain size. The grain refined alloy exhibited a reduction in segregation after heat treatment; an increase in ultimate tensile strength (+11%), yield strength (+13%), ductility (+8%), hardness (+2%), pitting corrosion; a decrease in impact strength and intergranular corrosion rate in comparison to the unmodified, base alloy.

ACKNOWLEDGMENTS

The greatest lesson I have learned at graduate school is that nothing worthwhile is possible without the help and support of family, friends, and colleagues. It is only by their involvement that graduate school is unequivocally one of the best life decisions I have ever made.

My appreciation for the guidance and technical support provided by my advisors, Dr. Ronald O'Malley, Dr. Simon Lekakh, and Dr. Laura Bartlett, is indescribable. It has been an honor working with such an accomplished group of metallurgists, and I will truly miss them all. A big thanks to the Peaslee Steel Manufacturing Research Center (PSMRC), and participating member companies, for providing the resources necessary to sustain my research project.

Thank you to the university faculty, staff, graduate researchers, and undergraduate students who assisted me during the course of this work. Also to my good friend and officemate, Mark Emmendorfer, for providing input on many of my experimental designs, teaching me how to use most of the foundry equipment, and keeping me sane from the everyday struggles of being a graduate student. I sure do appreciate ya!

I want to thank my parents for providing me with the confidence to persevere through any challenge, both in college and life. I would not be where I am today without their encouragement, love, and support. Finally, I want to give all glory to God for this achievement. Without the strength of my faith, I would have faltered in this task a long time ago. I look forward to how my life will be used to further glorify him until the day he calls me back home.

TABLE OF CONTENTS

Page

SECTION

PAPER

SECTION

LIST OF ILLUSTRATIONS

PAPER I

PAPER II

PAPER III

LIST OF TABLES

SECTION Page

PAPER I

PAPER II

PAPER III

1. INTRODUCTION

1.1. OVERVIEW

The first recorded commercial production of stainless steel used in industry occurred in England around the early 1900's. Development began at the request of a small arms manufacturer that desired to prolong the life of their gun barrels by minimizing erosion. However, the resulting steel was discovered to have superior resistance to chemical attacks due to its high chromium contents which was quite appealing to the cutlery industry at the time. Nearly a hundred years later, through research and development, stainless steel has become a material that offers higher strength, hardness, ductility, and corrosion resistance in comparison to plain carbon steels. It can be manufactured with relative ease and requires minimal maintenance when put into service. These characteristics make stainless steel a favorable choice for use in the construction, automotive, medical, energy, chemical, oil, gas, and food industries.

The microstructure of stainless steel is used to classify the grade which is determined by its chemical composition. These grades include austenitic, ferritic, duplex, martensitic, and precipitation-hardening steels, which each possessing their own unique set of properties. The most popular is the 300-series of austenitic stainless steel which possesses a combination of formability, ductility, toughness, weldability, and superior corrosion resistance in extreme conditions compared to the other grades. It can also maintain its strength at both low and high operating temperatures. It contains a minimum of 16 wt% chromium and 6 wt% nickel. Additional alloying elements such as molybdenum, titanium, or copper can be used to further improve the properties. Austenitic stainless steels are manufactured in a solution-annealed and quenched state to produce a microstructure with a homogeneous distribution of alloying elements throughout the matrix that is also free of carbide precipitates.[1]

However, engineering application of austenitic stainless steels is limited by an inherently low yield stress of 200 – 250 MPa.[1] There are various strengthening mechanisms employed by both foundries and steel mills to increase the strength of steel to a desirable value. These can include grain boundary strengthening by grain refinement, solid solution strengthening by alloying additions, precipitation hardening by heat treatment, and strain hardening by plastic deformation. These mechanisms are characterized by their behavior to impede dislocation motion which directly corresponds to an increase in the hardness and strength of the steel often with a subsequent loss in ductility.[2] Since no solid-solid phase transformations (or a small extent) of single phase austenitic or ferritic stainless steels occur after solidification is complete, these grades cannot be strengthened by heat treatment.[2] Strain hardening by cold work is the conventional method used for austenitic stainless steels and is related to the room temperature transformation of metastable austenite into strain-induced martensite.[3] In the case of cold worked 301 stainless steel, a yield strength of nearly 2,000 MPa was achieved.[3] Consequently, increasing the volume fraction of martensite results in a decrease of both ductility and corrosion resistance. Furthermore, the equipment required to induce the required plastic deformation for cold working may prove to be too costly for steel mills, and foundries casting near net shaped products will be restricted by geometrical tolerances to use this method. Therefore, strengthening austenitic stainless steels with an affordable process without compromising the quality and properties of the casting proves to be a challenge.

The aim of this research is to explore *TiN* as an active inoculant to refine the as-solidified grain structure and as a viable industrial method for improving mechanical properties in austenitic stainless steels. Grain refining methodologies were developed utilizing thermodynamic simulations followed by a series of experimental test pours in the Missouri S&T research foundry. These techniques include the *in-situ* formation of *TiN* on to pre-existing spinel oxides within the melt or by master alloy additions containing preformed *TiN* nuclei. Molds were designed to simulate the conditions observed in sand castings in foundry steel products as well as in continuously cast steels. The chemistries of experimental castings were analyzed utilizing optical emission arc spectroscopy and combustion analysis. The classification of inclusions in the resulting steels was conducted utilizing a scanning electron microscope (SEM) with energy dispersive X-ray spectroscopy (EDS) and in automated feature analysis (AFA) mode. Measurement of the equiaxed grain size and determination of the extent of macrostructure grain refinement for all steels was conducted utilizing optical metallography. The effect of a grain refined structure achieved by the developed melt practice on corrosion and tensile properties, machinability, and sigma phase formation were investigated. Future work is outlined for additional characterization and improvements of the current melt practice moving forward.

1.2. IMPORTANCE OF CAST MACROSTRUCTURE

The as-cast grain size is of critical importance not only for material strength but also for quality-control purposes. The formation of a desired microstructure in the final product is dependent on all steps of the processing route: melting, casting, solid-state forming, and/or heat treatment. It is the post-casting processes that are used to target specified material properties, but each processing route adds significant increases in cost to the final product.[4] Therefore, acquiring better control of the as-cast structure during melting and casting provides considerable economic and technical incentives.[4]

1.2.1. Industrial Processes. The schematic flow chart illustrated in Figure 1.1 shows the iron and steelmaking set-up for two steel mill configurations. Both processes use a continuous caster to turn the molten steel into either beam blanks, rounds, billets, blooms, and/or slabs. Additionally, the molten steel can also be cast into ingot molds. These ingots or blanks can then undergo any combination of heat treatment, rolling, finishing, and/or coating to produce the final product. The main difference between the two configurations occurs during the melting processes.

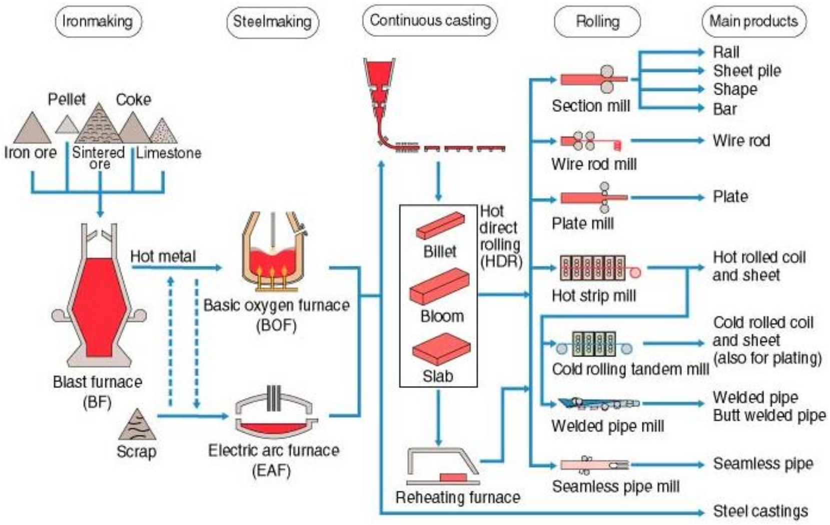

Figure 1.1. Steelmaking process flow chart for a typical steel mill.[5]

The first process is known as an integrated mill which begins by melting iron ore and other constituents in a blast furnace to produce liquid pig iron. This liquid metal is transported to a basic oxygen furnace (BOF) where it is diluted with steel scrap and decarburized by oxygen blowing. Reduction of iron oxide from the slag occurs during decarburization thus improving furnace yield. The transformation of molten iron in the BOF to molten steel is complete once the desired carbon content is achieved. In the second process, a combination of steel scrap and direct reduced iron is melted in an electric arc furnace (EAF) to produce molten steel. Melting of stainless steel and other high alloy grades with oxidable elements in an EAF requires the melt be transferred to an argon oxygen decarburization (AOD) vessel for additional refining steps. These steps include decarburization of the melt by oxygen-argon blowing, reduction of oxidized elements in the slag by silicon or aluminum additions, and desulphurization with lime. The liquid steel produced from the BF-BOF, EAF, and EAF-AOD is then transported to a series of secondary steelmaking stations where the melt can be deoxidized, desulfurized, alloyed, reheated, and/or degassed to a targeted composition and temperature. The melt is then transferred by ladle to the continuous caster where the ladle is tapped into a tundish which feeds into an oscillating, water cooled mold. Billets, blooms, and/or slabs are casted by the mold and then transformed into the final products by rolling.

The schematic flow chart shown in Figure 1.2 illustrates the typical set-up of a steel foundry. Foundries have the capability to produce complex shaped castings, but at a much lower production volume of steel in comparison to a steel mill. Modern steel foundries can use either induction furnaces (IF) or electric arc furnaces (EAF) for melting steel.[7] The furnace is charged with a combination of virgin material, scrap, and alloying additions. The resulting liquid metal is refined to remove elements and gases that may cause casting defects. The melt is tapped from the furnace into a transfer ladle. Adjustments to the melt chemistry can be made either in the furnace, an AOD, or the ladle. Fluxing agents are added to promote the absorption of impurities from the melt into the slag which are removed during deslagging steps. Once at the desired composition and temperature, the melt is poured from the ladle into a sand mold containing a hollow cavity. The metal solidifies in the cavity forming the cast product. After cleaning and inspection, the part is machined, heat treated, coated, and/or assembled into the finished cast product.

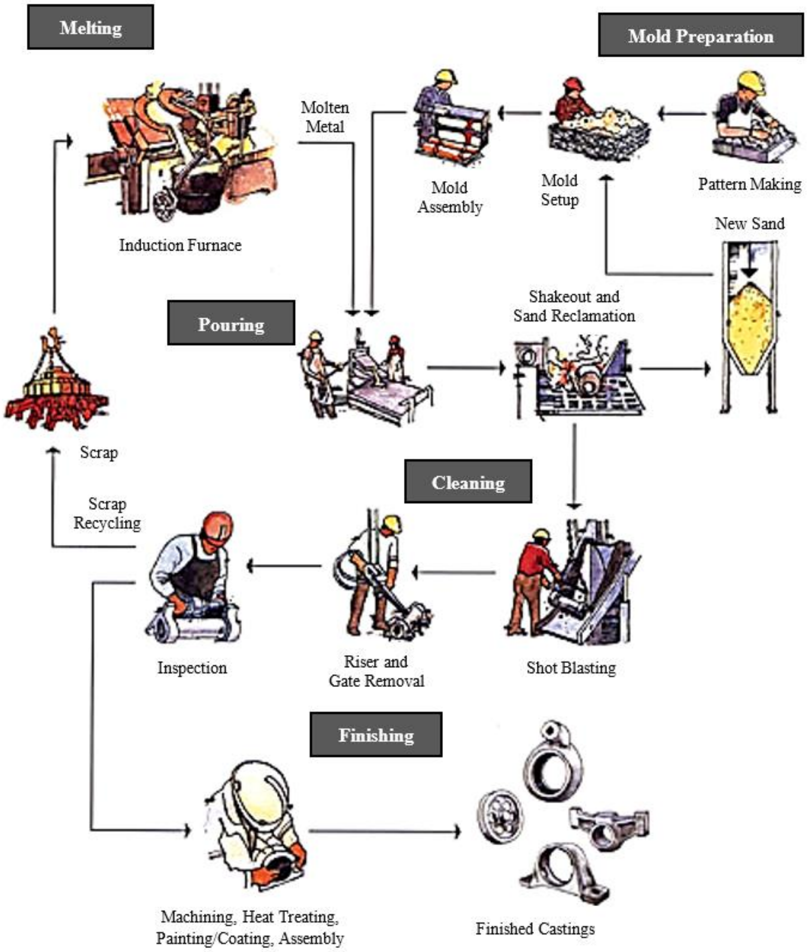

Figure 1.2. Steelmaking process flow chart for a typical steel foundry.[6]

1.2.2. Cast Structure. A solidified steel ingot can consist of three zones which have been labeled with Arabic numerals in Figure 1.3. (1) Near the mold wall there is a thin layer of equiaxed crystals known as the chill zone. (2) The elongated grains that grow out of the chill zone into the liquid metal establishes a columnar zone. (3) Conditions that encourage heterogeneous nucleation and growth within the melt leads to the formation of an equiaxed zone in the center of the ingot which is comprised of equiaxed grains.

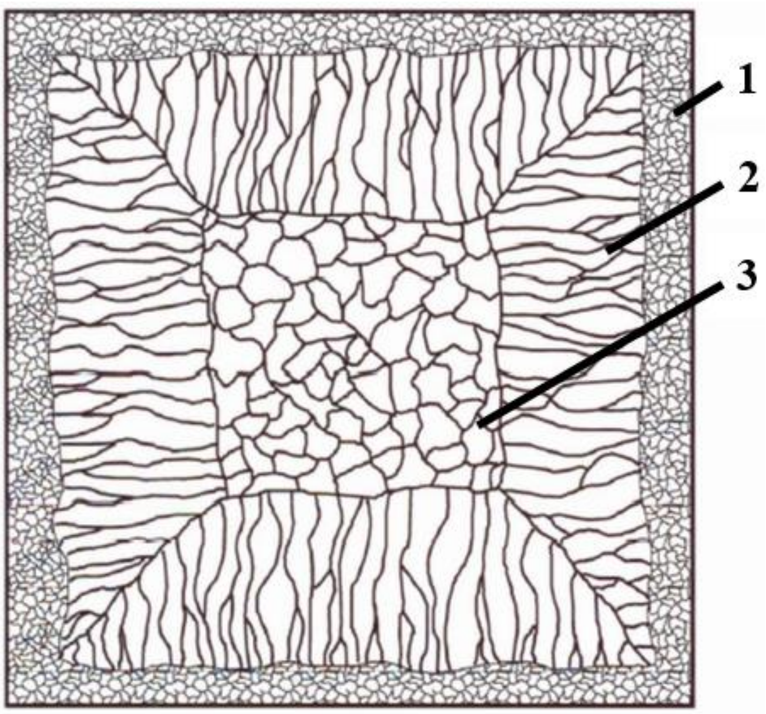

Figure 1.3. Cast structure of steel alloy after solidification.[9]

Cast alloys can be fully columnar, fully equiaxed, or contain all three zones. Inoculation of the liquid metal can be used to promote a large equiaxed zone. Thermal conditions in a water cooled, continuous cast mold tends to favor the formation of a large columnar zone.

1.2.2.1. Chill zone. The liquid metal that first contacts the mold wall is rapidly cooled below its liquidus temperature due to a large temperature difference that drives heat transfer. As a result, the nucleation rate is high and many solid nuclei will begin growing at the mold wall interface forming a layer of small chill grains. Low pouring temperatures and turbulence can promote fragmentation of chill grains into the melt that will survive because of undercooling.[10] These crystal fragments will act as favorable sites for nucleation thus inducing an equiaxed zone. Additionally, if the pouring temperature is too high, the liquid metal will remain above its liquidus temperature for a longer period. Most of the crystal fragments will remelt with nucleation and growth occurring only at the mold wall.[10]

1.2.2.2. Columnar zone. The factor that differentiates whether a grain will continue to grow out of the chill zone is related to the orientation of grain growth from the mold wall.[10] Crystals that grow in their preferred crystallographic orientation, while following the path most parallel but opposite to heat flow, will outgrow neighboring grains that are less favorably oriented. Continued growth of these grains into the melt leads to the formation of the columnar zone. Crystallographic orientation is related to the type of metal solidifying. Therefore, for cubic metals, columnar grains will grow in a <100> direction which is perpendicular to the mold walls and parallel to the largest temperature gradient.[10] This behavior can be seen in Figure 1.4 for dendritic growth of a cubic metal. For symmetric mold geometries, nearly all columnar grains will have the same orientation in the final solidified structure.

1.2.2.3. Equiaxed zone. The equiaxed zone is composed of randomly oriented, equiaxed grains in the center of the casting. Formation of the equiaxed zone is dependent upon alloy composition and on the thermal gradient at the liquid-solid interface during solidification. Alloys that have a large freezing range will have an extensive mushy zone and solidify primarily with an equiaxed structure. Additionally, low thermal gradients by slow cooling the liquid metal also promotes the formation of equiaxed solidification.

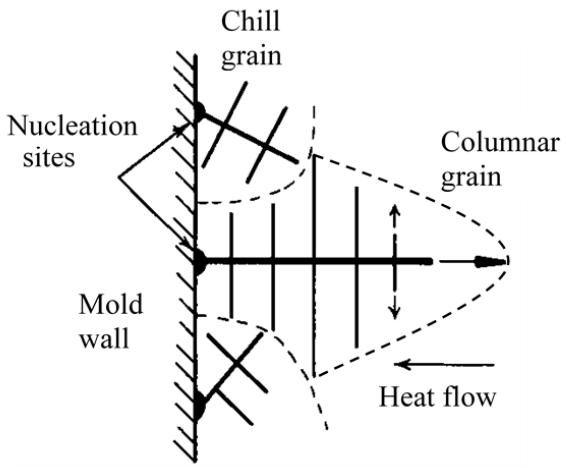

Figure 1.4. Competitive growth of grains at the mold wall interface.[10]

It is thought that the detachment of dendrite side-arms from grains formed at the mold wall provides ‘seed’ particles within the melt that can nucleate and grow new dendrites thus forming equiaxed grains.[10] A certain degree of liquid undercooling must exist to ensure that the detached dendrite side-arms do not dissolve back into the liquid metal. Convection is an important aspect for effective dendrite fragmentation. It provides the fluctuations in temperature necessary to weaken dendrite side-arms, the force required for detachment, and the fluid flow necessary to disperse the fragments throughout the liquid metal. Two common types are natural convection where differences in temperature throughout the liquid metal drives fluid flow or by forced convection where an external force is applied such as mechanical stirring of the liquid metal. Columnar growth stops when columnar grains impinge upon equiaxed grains growing within the melt. Therefore, increasing the size of the equiaxed zone has the direct effect of reducing the extent of the columnar zone.

1.2.3. Effect of Grain Size. Plastic deformation occurs by the shear of close-packed planes of atoms over one another. A certain number of slip systems (planes and directions upon which slip occurs) must exist for plastic deformation to be possible in polycrystalline materials. In general, the more slip systems that are present in a material corresponds to a greater capacity for deformation.[2] Furthermore, strengthening a material requires increasing the number of dislocation barriers to prevent slip. The existence of multiple grains in polycrystalline metals forces the slip plane to be oriented differently from one grain boundary to another. Reducing the grain size increases the number of grain boundaries which produces more changes in direction of the slip path while also lengthening it (i.e. increased ductility). Meanwhile, dislocations cannot cross the grain boundaries but instead are blocked and piled up at the boundaries (i.e. increased strength). This relationship between increasing yield strength with decreasing grain size is demonstrated by the well-known Hall-Petch relationship in Eq. (1):

$$\sigma_y = \sigma_o + k_y d^{-1/2} \tag{1}$$

where: k_y is a material constant related to grain boundary hardening, d is the grain diameter, and σ_o is the Peierls-Nabarro stress or the friction stress to start dislocation motion in a single crystal. Therefore, decreasing the grain size is effective in both increasing strength and ductility which makes it one of the most effective strengthening mechanisms for steels.[2]

1.3. METHODS OF GRAIN REFINEMENT

Grain refinement has been widely studied in research and applied with success in industrial applications for a variety of metals. It has been proven that an equiaxed structure improves castability, reduces segregation and macroporosity, and refines the macro/microstructure which leads to improved mechanical properties such as strength and toughness.[11-13] Some practices like alloying additions and work hardening also improve strength but typically with a subsequent loss in other mechanical properties. Modern grain refining practices of cast steel is more challenging than its nonferrous counterparts contributing to its slow development and adoption in industry. Often the benefits of a refined structure are outweighed by increased production costs and/or deleterious side effects originating from the grain refining practice. However, recent efforts in research continues to reveal novel methods that mitigate these deterrents.

Manipulation of grain size for most steels can be achieved at three different steps throughout the casting or finishing processes: (i) during solidification of the liquid metal by increasing the nucleation rate of the solid, (ii) by mechanical working, and (iii) by heat treatment of steels having polymorphic solid-state transformations, such as FCC→BCC reactions. Grain refinement by mechanical working is limited to forging for net shaped castings. Additionally, heat treatment cannot be effectively employed to promote grain refinement of single phase alloys.[14] Inoculation techniques to refine the solidification structure of austenitic stainless steel castings are crucial because significant cast structure modification of these alloys cannot be achieved by heat treatment or mechanical working of cast, near net shaped components. In steel mill operations, thermomechanical methods that include both mechanical working and heat treatment are employed to control grain size; however, as-cast grain structure is still important to control segregation and porosity. Grain refinement of the as-cast structure results in a casting that has higher strength, more isotropic properties, less segregation and porosity, better feeding, and a higher resistance to hot tearing.[15] The following sections will be a literature review of the solidification-based grain refining practices that have been developed for austenitic stainless steels.

1.3.1. Dynamic Nucleation. The technologies of grain refinement during solidification are commonly categorized into two classes: dynamic nucleation and inoculation.[16] Dynamic nucleation employs a combination of forced convection and fast cooling which promotes an increase of secondary nuclei within the melt. These nuclei are a result of dendrites that break off from the mold wall. An equiaxed structure forms by heterogeneous nucleation from these dendrite fragments. Applied forces that are known to cause grain refinement by promoting dynamic nucleation in solidifying steel are vibration[17,18], mechanical/gas stirring[19], and electromagnetic stirring[20-25]. Dynamic nucleation is feasible for continuous cast steel operations, which have molds that are fixed in shape and size and cast simple geometries. However, this method is difficult to apply in a commercial foundry which can have molds that vary in shape, size, and complexity.

1.3.2. Inoculation. In foundry practice, the inoculation method is more commonly used for refining grain structure. This method introduces or promotes the formation of “foreign” heterogeneous nuclei by controlled precipitation during cooling or melt additions prior to the beginning of solidification. These heterogeneous nuclei must: (i) be stable at steelmaking temperatures, (ii) be well dispersed throughout the melt, (iii) have suitable lattice registry with the primary solid phase, (iv) be readily wet by the solidifying metal (i.e. surface energy minimization), and (v) have an appropriate size and shape that promotes nucleation. A more detailed discussion of the theoretical aspects of heterogeneous nucleation activity will be presented in the following sections of this thesis.

Inoculation is performed either by in-situ formation of nuclei with designed melt additions or by the introduction of a master alloy containing preformed nuclei. The technique of in-situ development has been widely explored in literature for ferritic steels but has been less studied for austenitic steels. Tyas conducted a series of inoculated austenitic stainless steel weld experiments in an attempt to achieve a grain refined structure using nuclei based on lattice disregistry and solubility calculations. The results of these experiments indicated that an equiaxed structure in the weld was achieved by inoculation with Si_3N_4, TaN, or HfC particles (in decreasing order of effectiveness).[26] Siafakas et al. examined the effects of oxides on the as-cast grain size of Al-Ti treated austenitic manganese steels. It was determine that increasing oxide population resulted in a decrease in grain size.[27] Initial grain size was reduced from 605 μm to 305 μm with spinel, 375 μm with olivine, and 497 μm with corundum.[27] Other non-metallic inclusions formed by melt additions that are proven experimentally to be stable, heterogeneous nuclei for the nucleation of austenite phase includes: spinel[28], Ti-containing inclusions[29,30], and rare earth metals (REM)-oxides and sulfides[31-33]. Suito found that TiN has a strong tendency to combine with MgO to form complex inclusions.[34] In the Fe-10% Ni alloy, the population density of $TiN+MgO$ complexes was considerably higher than that of pure TiN or TiN coupled with any of the other oxides (Al_2O_3, ZrO_2, and Ce_2O_3). Lekakh et al. applied this behavior to enhance heterogeneous nucleation and growth of TiN nuclei in a Cr-Ni-Mo austenitic stainless steel. The main mechanism includes first the formation of complex oxides followed by the accelerated co-precipitation of TiN onto the oxide surfaces.[35] Grain size of the as-cast structure was reduced from 2400 μm to 500 μm using this method.

The technique of master alloy addition is a popular way to grain refine aluminum alloys typically by using a Al-Ti-B master alloy.[36] Master alloys offer the flexibility to make the addition at any point prior to casting, thus giving better control of nuclei quantity and size. In literature, the development and application of master alloy for use in the commercial production of cast steel is still being investigated.[33] In particular, the development of REM based master alloys has yielded some positive grain refining results in austenitic and duplex stainless steel alloys. It was discovered that grain refinement of an austenitic stainless steel could be achieved by adding aluminum and powdered Fe-Ce master alloy to the liquid metal prior to solidification. The dominant inclusions observed were complex Ce-aluminates with the best grain refining effect occurring when the inclusions were around 1 μm in diameter.[29] Dahle applied a commercial grain refiner containing Fe-Cr-Si-Ce, known as EGR, to examine its effectiveness in super duplex stainless steel grade S4501.[37] Most of the oxides formed in the melt were Ce containing complexes: $(Ce,Si)O_2$ and $(Al,Ce,Si)_2O_3$. The macrostructure analysis showed a substantial decrease in the length of the columnar zone at approximately 0.07% Ce addition. The same Ce-containing master alloy was also used to refine an austenitic stainless steel grade S254 SMO. A substantial reduction in the dendrite arm spacing was achieved by promoting the formation of Ce-Al oxide inclusions in the steel prior to solidification.[38] Mizumoto et al. created a Fe-Nb-C master alloy that contains NbC precipitates. When the addition of master alloy was 3 wt.% in a SUS316 stainless steel melt, a fine equiaxed structure was achieved and the average grain size was reduced from 2700 μm to 200 μm.[39] Wang et al. suggested the industrial viability of *Fe-Ti-N* master alloy for grain refining 409L ferritic stainless steel. It was reported that the average equiaxed grain size decreased from 1503 μm to 303 μm, and the equiaxed grain zone expanded from 14% to 100% of the casting with an addition of 2.5 wt.% *Fe-Ti-N* master alloy.[40] Much work is still required for development of novel master alloy designs to inoculate austenitic stainless steels.

1.4. THEORETICAL BACKGROUND

The thermodynamics and kinetics of nuclei formation within the liquid metal is covered in this section. Also discussed are the conditions that control the extent of equiaxed and columnar zones in the cast structure.

1.4.1. Thermodynamic Stability. The parameter for evaluating the most stable phase to form within a system undergoing a change of state is known as Gibbs free energy (ΔG). Determination of the minimum value of ΔG for a system at a defined pressure, temperature, and concentration of components in the system is the definition of when equilibrium of the system has been achieved. Derivation of binary and ternary phase diagrams are a result of determining the lowest free energy as each component concentration is varied at a fixed temperature and pressure.[41] Only by repeating this analysis through a series of temperatures can the classic binary and ternary phase diagrams of temperature *vs* component concentration be assembled. These diagrams describe regions of phase stability for solids and liquids that form within the system at corresponding component concentrations and temperatures (fixed pressure). For a multicomponent system, there are many possibilities of phases that can form as temperature, pressure, and/or component concentration are varied. Some of these variables change based on how the system interacts with itself and the environment via reactions.

The formation of titanium nitrides (TiN) and spinel ($MgAl_2O_4$) in molten stainless steel are of particular interest throughout this research. Therefore, the thermodynamics associated with these reactions will be explored. The composition of molten stainless steel contains a fairly large number of alloying elements. Modeling molten steel as a solution that contains multiple dilute solutes provides a viable, yet complex, numerical approach for estimating element solubility and phase stability.[41] The following reaction shown in Eq. (2) is for solid TiN inclusions forming within a stainless steel melt:

$$[Ti] + [N] = TiN_{(s)} \tag{2}$$

where: $[Ti]$ and $[N]$ are the dissolved reactants of titanium and nitrogen in the melt; and $TiN_{(s)}$ is the solid inclusion at equilibrium formed after reaction. The free energy of this reaction in equilibrium can be written as:

$$\Delta G = \Delta G^o + RTln\left(K_{eq}\right) = 0 \tag{3}$$

where: ΔG^o is the standard Gibbs free energy of formation; R is the universal gas constant; T is temperature; and K_{eq} is the equilibrium constant. The equilibrium constant can be written in terms of the reaction and simplified as shown in Eq. (4):

$$K_{eq} = \frac{a_{TiN}}{h_{Ti\ (1\ wt\%)}h_{N\ (1\ wt\%)}} = \frac{1}{f_{Ti}[\%Ti]f_N[\%N]} \tag{4}$$

where: a_{TiN} is the activity of solid titanium nitride formed from the reaction; h_{Ti} and h_N are the 1 wt.% standard state Henrian activities of titanium and nitrogen dissolved in the stainless steel melt; f_{Ti} and f_N are the Henrian activity coefficients; $[\%Ti]$ and $[\%N]$ are the dissolved titanium and nitrogen contents in wt.% in the stainless steel melt. The Henrian activity coefficients are further expanded in Eq. (5) where second order terms are considered negligible:

$$\log f_{Ti} = \varepsilon_{Ti}^{Ti}[\%Ti] + \varepsilon_{Ti}^{N}[\%N] + \varepsilon_{Ti}^{Fe}[\%Fe] + \varepsilon_{Ti}^{Cr}[\%Cr] + \varepsilon_{Ti}^{Ni}[\%Ni] + \cdots \quad (5)$$

where: ε terms are the interaction parameters at a specified temperature. Calculation of the interaction parameters becomes more numerically intensive by increasing the number of alloying elements in the melt. If titanium nitride forms as a pure solid ($a_{TiN} = 1$), dissolved *Ti-N* contents do not obey Henry's Law (f_{Ti}, $f_N \neq 1$), and equilibrium of the reaction is achieved ($\Delta G = 0$), then Eq. (3) can be rewritten into Eq. (6).

$$[\%N] = \left(f_{Ti} f_N [\%Ti] e^{\frac{-\Delta G^o}{RT}}\right)^{-1} \quad (6)$$

This equation describes the *Ti-N* contents and thermal conditions required for titanium nitride to form in a stainless steel melt of specified composition. When the melt composition and temperature are specified, the weight percent nitrogen required to form titanium nitride in the stainless steel melt becomes a function of the weight percent of titanium dissolved. This same procedure can also be applied to predict phase stability of spinel in the stainless steel melt. Some of the potential reactions associated with spinel formation are shown by the reactions in Eq. (7) through Eq. (11).

$$[Mg] + 2[Al] + 4[O] = MgAl_2O_{4(s)} \quad (7)$$

$$[Al] + 3[O] = Al_2O_{3(s)} \quad (8)$$

$$[Mg] + [O] = MgO_{(s)} \quad (9)$$

$$Al_2O_{3(s)} + [Mg] + [O] = MgAl_2O_{4(s)} \quad (10)$$

$$MgO_{(s)} + 2[Al] + 3[O] = MgAl_2O_{4(s)} \quad (11)$$

These reactions listed do not include the multitude of other potential oxides, sulfides, and nitrides that may form within the stainless steel melt either prior to or upon addition of *Mg*, *Al*, and/or *Ti*. Gibbs free energy of each reaction must be calculated according to Eq. (3) and compared in order to approximate the most favorable reaction product to form in the system. However, it is evident by the previous thermodynamic analysis of one reaction (formation of TiN) that the calculations are both intensive and require a great deal of knowledge about the specific reaction. It is for this reason that thermodynamic simulation software was employed to assist with these calculations. This software uses the minimization of Gibbs free energy to predict reaction products which is the same concept that was previously discussed. Additionally, the databases associated with the software contain valuable information such as the interaction parameters which are otherwise difficult to obtain. The thermodynamic software implemented in this research includes FactSage 7.0 and Thermo-Calc 2016a.

1.4.2. Nucleation Theory. Solidification of a metal first begins by the creation of a cluster of atoms with a crystalline structure that forms within the melt. A stable nuclei forms when the cluster is large enough to remain in its crystalline form without dissolving back into the melt. This process is known as nucleation. Nucleation is followed by growth where the nuclei grow as crystals into the melt thus forming a grain structure. In classical theory, homogeneous nucleation occurs when local temperature variations in the melt cause pre-embryonic clusters to appear spontaneously and decay in a melt that is free of impurities. This type of nucleation requires a significant amount of undercooling driven by the volumetric free energy change which is always negative below the equilibrium freezing temperature. The volumetric free energy change decreases with decreasing temperature (undercooling) and with an increase in the radius of the embryo, driving nucleation. However, formation of the solid-liquid interface presents a positive surface energy penalty that increases as the size of the embryo increases and this retards nucleation. The difference in free energy between a spherical, solid embryo in contact with an entirely liquid system is given in Eq. (12):

$$\Delta G_{Hom} = \frac{4}{3}\pi R^3 \Delta G_V + 4\pi R^2 \gamma_{SL} \tag{12}$$

where: R is the radius of the solid, spherical embryo or cluster; ΔG_V is the change in free energy per unit volume between the cluster and the liquid; γ_{SL} is the interfacial energy between the cluster and the liquid. ΔG_{Hom} at or below the equilibrium freezing point is a function of both the interfacial free energy change (always positive) and the bulk or volumetric free energy change (always negative) as shown in Figure 1.5. The maximum $\Delta G_{Hom}(R)$ curve is known as the homogeneous nucleation barrier, ΔG^*.[42] This occurs at a critical radius, R^*, so that when $R < R^*$ dissolution of the solid embryo into the liquid (not a stable nucleus) reduces the free energy and when $R > R^*$ continued growth of the embryo and formation of a stable nucleus reduces the free energy.[42] This behavior is illustrated by the plot shown in Figure 1.5.

Achieving nucleation by large undercooling is unrealistic in common practice. Homogeneous nucleation is predicted to occur at very large undercoolings, often hundreds of degrees, and this is contrary to laboratory/industrial observations. Therefore, the mechanism of heterogeneous nucleation where solidification is initiated on foreign surfaces within the melt (i.e. impurities, fragmented dendrites, or mold wall) is used to describe practical liquid metal systems that possess small undercooling. This can be accomplished only if the interfacial energy term is reduced which is accomplished by having the cluster form in contact with a foreign, solid substrate.

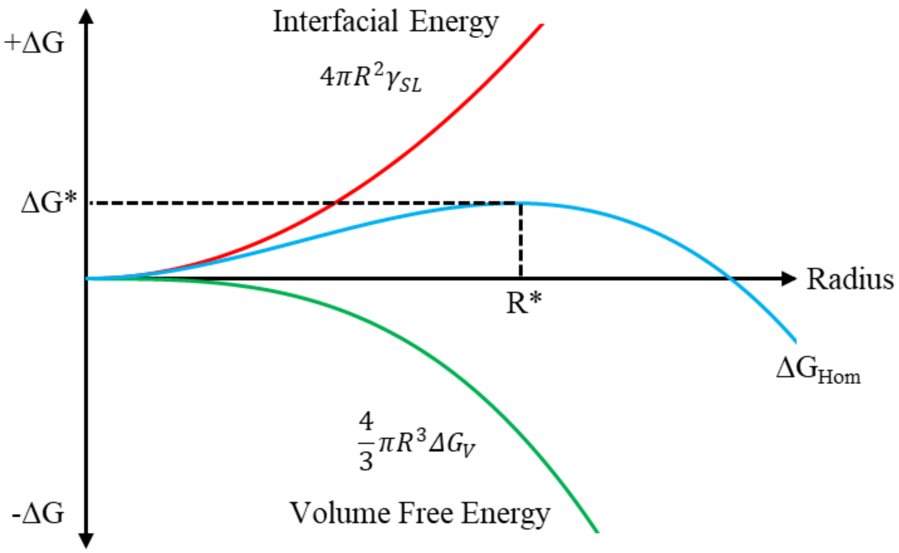

Figure 1.5. Surface, bulk, and total free energies of a spherical solid as function of its radius for a fixed undercooling.

If the foreign substrate has a similar structure and chemistry to that of the nucleating material, then it will be energetically favorable to form a solid nucleus on the foreign surface. The image in Figure 1.6 shows a spherical cluster nucleating on to a foreign substrate. The γ-terms correspond to the interfacial energies associated with the surface tension between the foreign substrate (F), the solid cluster (S), and the liquid metal (L).

The contact angle, θ, represents how well the cluster wets the substrate. Approximating the cluster as a spherical cap with radius, R_{Cap}, implies that the surface energies are isotropic and that gravitational effects can be neglected.[42] Balancing the interfacial energy terms yields the following relationship in Eq. (13).

$$\gamma_{FL} = \gamma_{FS} + \gamma_{SL} \cos\theta \tag{13}$$

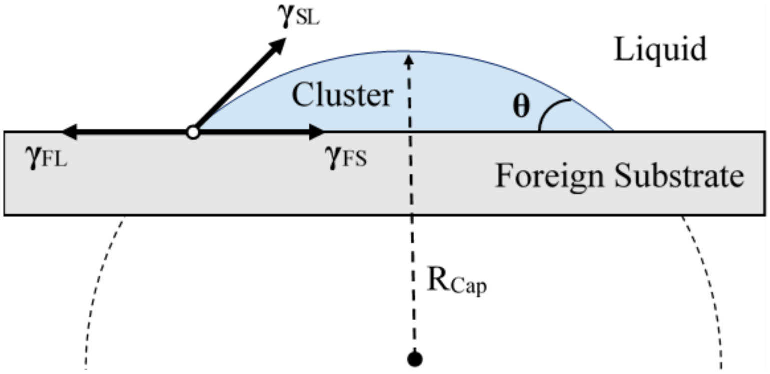

Figure 1.6. Nucleation of a spherical solid cap at a liquid-substrate interface.

The spherical cluster wets the substrate when $0^{o} \leq \theta \leq 90^{o}$ and is non-wetting when $90^{o} \leq \theta \leq 180^{o}$. In general, decreasing the contact angle reduces the number of atoms required to form a critical nucleus thus decreasing the nucleation energy barrier. It is not related to a reduction in the surface energies which remains a constant value. Therefore, the free energy of heterogeneous nucleation for a spherical cluster can be expressed as:

$$\Delta G_{Het} = V_S \Delta G_V + A_{SL}\gamma_{SL} + A_{FS}\gamma_{FS} - A_{FL}\gamma_{FL} \tag{14}$$

where: V_S is the volume of the solid cluster; the A-terms correspond to the surface areas associated with the interaction between the between the foreign substrate (F), the solid cluster (*S*), and the liquid metal (*L*). Eq. (13) can be substituted into Eq. (14) thus simplifying the expression to:

$$\mathit{\Delta} G_{Het} = \frac{(2+\cos\theta)(1-\cos\theta)^2}{4} * \mathit{\Delta} G_{Hom} = \mathrm{f}(\theta) * \mathit{\Delta} G_{Hom} \tag{15}$$

It is revealed that heterogeneous nucleation has the same form as homogeneous nucleation but with an additional geometry factor, $f(\theta)$. This geometry factor is directly related to the shape of the substrate (flat, folded, cavity, etc.) that is being nucleated upon. Furthermore, heterogeneous and homogeneous nucleation share the same critical radius, R^*, that determines when a cluster shrinks or grows in the melt. Thus, the heterogeneous nucleation barrier is determined by the geometry factor which can range between $0 \leq f(\theta) \leq 1$. A geometry factor of 0 correspond to perfect wetting such that no nucleation barrier exists and solidification is limited only by growth.[42] A geometry factor of 1 corresponds to complete non-wetting on to the substrate, and is equivalent to homogeneous nucleation. Therefore, any geometry factor less than 1 will always result in a nucleation barrier that is lower than that of homogeneous nucleation (i.e. $\mathit{\Delta} G^*_{Het} < \mathit{\Delta} G^*_{Hom}$). The geometry factor, $f(\theta)$, can also be written as a ratio of the volumes of the spherical cap and a full sphere shown in Eq. (16).[42]

$$\mathrm{f}(\theta) = {V_{Sphere}}\Big/{\tfrac{4}{3}\pi {R_{Cap}}^3} = \left({R_{Sphere}}\big/{R_{Cap}}\right)^3 \tag{16}$$

This form of the geometry factor can be used to approximate any substrate geometry so long as the corresponding radius of the cap can be measured through contact angles 0º ≤ $\theta \leq$ 180º. The term R_{Sphere} for a corresponding substrate geometry is measured at θ = 180º, and is a fixed value. The term R_{Cap} for a corresponding substrate geometry varies through values 0º ≤ $\theta <$ 180º, and results in $R_{Cap} > R_{Sphere}$ which causes the geometry factor to be any value between $0 \leq f(\theta) < 1$. This approach of measuring cap radius and comparing against the radius of a sphere for a corresponding substrate geometry was used in combination with a surface evolver - fluid interface tool (SE-FIT®) software for this research. The results of this software are shown in Figure 1.7 for a flat surface substrate where the trend reveals that geometry factor is directly proportional to the contact angle.

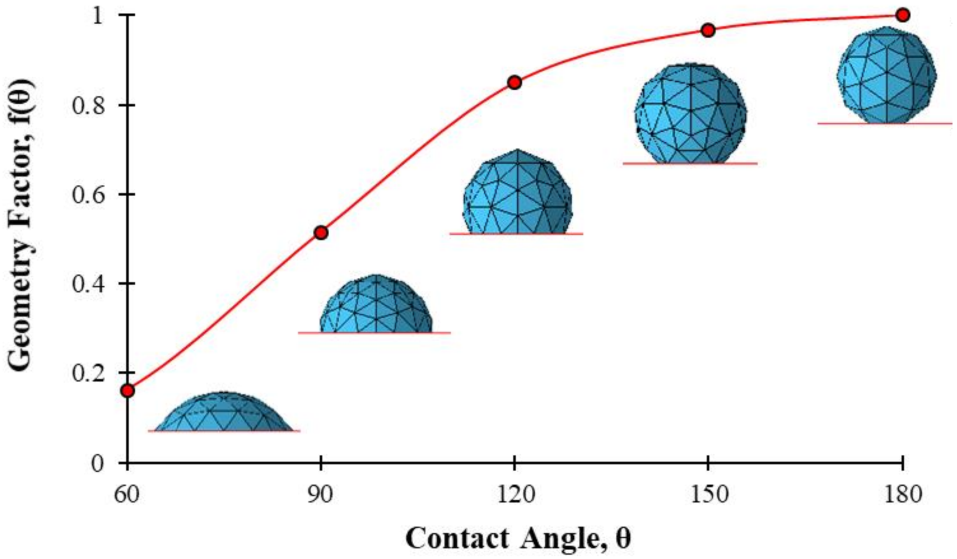

Figure 1.7. Simulated geometry factor of a flat surface substrate using SE-FIT® software.

The accuracy of using Eq. (16) with the surface evolver software compared to the theoretical *f(θ)* values shown in Eq. (15) for a flat surface substrate were compared. These results are shown in Table 1 with the percent difference in Eq. (15) theoretical values *vs* Eq. (16) simulated software values being highlighted in green. Differences in the geometry factor of the two methods are small. Therefore, the surface evolver software provides a relatively easy method for determining the geometry factor of complex substrate geometries. Additional discussion of the theoretical aspects of heterogeneous nucleation activity can be found in the works of Chalmers, Flemings, and Kurz and Fisher.[43-45]

1.4.3. Effective Heterogeneous Nuclei. The effectiveness of heterogeneous nucleation behavior is related to the similarity of the lattice parameters shared between the nuclei substrate and the nucleated solid, which is known as crystallographic disregistry or misfit. This mechanism is widely accepted as a means to explain why some inclusions promote nucleation (low %misfit) while others do not (high %misfit).

Table 1.1. Comparison of geometry factors calculated using theoretical Eq. (15) and simulated Eq. (16).

	f(θ)		
Contact Angle, θ	Theoretical	SE-FIT® Software	%Difference
180	1.00	1.00	0%
150	0.99	0.97	2%
120	0.84	0.85	1%
90	0.50	0.52	3%
60	0.16	0.16	0%

Bramfitt modified the Turnbull-Vonnegut equation to calculate planar disregistry between two phases of differing atomic arrangements.[46] Bramfitt used this equation, along with experimental results to study the effect of oxides, carbides, and nitrides on the heterogeneous nucleation behavior of liquid iron, proposing that a lattice mismatch less than 12% constitutes a potent nucleant agent. However, the authors performed ab initio calculations of adsorption energy for Fe atoms on to the surfaces of carbides and nitrides at the early stages of nucleation.[47] It was found that Fe adsorption on to the nuclei substrate is closely related to the number of valence electrons in the carbides and nitrides, and less dependent upon lattice parameter and surface energy of phases.

Regardless, calculating disregistry is a common technique for initial screening of potential heterogeneous nuclei. A list of the calculated crystallographic misfit values for a variety of compounds with ferrite and austenite is provided in Table 1.2.[48] Some of these compounds have not been tested experimentally but are suggested as potential nucleant agents for ferrite and/or austenite phase based purely on the calculated lattice disregistry. Even though disregistry can provide a valuable initial estimate of nucleation potency, it does not fully describe the mechanisms of nucleation and growth. Other important factors that influence inoculation potency includes nuclei number density, particle geometry, solute concentration at the solid-liquid interface, and solute diffusivity.[27] Additionally, stability of the nuclei at steelmaking temperatures (>1500 ^{o}C) and the amount of supersaturation in the melt required to form the nuclei (i.e. quantity of additions that need to made) are also contributing reasons that only a limited number of heterogeneous nuclei are known to be effective for grain refining steel alloys. Therefore, not all of the compounds listed in Table 1.2 are feasible as inoculants for industrial application.

1.4.4. Solidification Morphologies. Understanding growth morphologies first begins with identifying the conditions that cause an instability of the growing solid-liquid interface. Often the stability criteria are dependent upon mathematical functions that describe whether perturbation of the solid-liquid interface is amplified or damped over time. For columnar growth in a pure substance (i.e. no segregation), the temperature always increases with distance ahead of the solid-liquid interface into the melt such that heat flow is opposite to the direction of solidification.[45] When a perturbations (peaks and valleys) form on an initially smooth, planar interface, the temperature gradient in the liquid increases and in the solid decreases. This results in more heat flowing into the tips of the perturbation peaks which causes the peaks to dissolve back into the melt thus stabilizing planar growth. The opposite behavior occurs in equiaxed growth where the free crystals form away from the mold wall within the undercooled melt.[45] Latent heat produced during equiaxed solidification flows from the solid into the liquid (negative thermal gradient). Increasing the amplitude of the perturbation peaks causes a steeper thermal gradient between the solid and the undercooled liquid which allows the peak tips to reject more heat thus increasing the growth rate. The solid-liquid interface during equiaxed solidification is always morphologically unstable.

The stability criterion becomes much more complex for alloys because the local equilibrium melting point can vary at the solid-liquid interface. This is typically caused by the rejection of solute from the solid into the liquid which accumulates and forms an enriched liquid boundary layer ahead of the solid-liquid interface. This solute-rich boundary layer possesses a liquidus temperature that increases with distance from the interface as the solute concentration decreases which is shown in Figure 1.8. The liquid is constitutionally undercooled when the actual liquid temperature (T_A) ahead of the interface is lower than the local equilibrium solidification temperature (T_L) which leads to instability of the interface. This zone of constitutional undercooling has been shaded in Figure 1.8, and is purely a consequence of compositional differences in the liquid causing metastability. It should be apparent from Figure 1.8 that the conditions necessary for the existence of this zone are strictly dependent upon the thermal gradient of the liquid temperature at the interface and the thermal gradient of liquidus temperature change in the melt.

Table 1.2. Crystallographic misfit of compounds with FCC- and BCC-Iron.[48]

Precipitate	Crystal Type	Misfit with Ferrite (%)	Misfit with Austenite (%)
MnS	Cubic	28.9	1.3
AlN	Hexagonal	8.5	3.5
TiN	Cubic	4.6	7.7
Al_2O_3	Hexagonal	17.4	7.7
SiO_2	Tetragonal	22.7	3.6
TiC	Cubic	6.8	16.1
VN	Cubic	2.1	13.5
BN	Hexagonal	12.6	31.3
Ti_2O_3	Hexagonal	26.8	0.4
NbC	Cubic	10.3	13.3
NbN	Hexagonal	3.3	18.8
Ferrite	Bcc	-	-
Austenite	Fcc	-	-

Consequently, these thermal gradients also govern the growth morphologies.[45] If the thermal gradient of the liquid (dT_A/dZ) is greater than the slope of liquidus temperature (dT_L/dZ), then no zone of constitutional undercooling would exist since the liquid temperature (T_A) would be greater than the liquidus temperature (T_L). Any perturbations forming at the interface would dissolve back into the melt resulting in stable planar growth. The opposite scenario allows for the existence of a zone of constitutional undercooling such that any perturbations that form at the unstable interface will not dissolve since it is surrounded by undercooled liquid. These perturbations proceed to grow dendritically, and the growth rate can be accelerated by increasing the amount of undercooling.

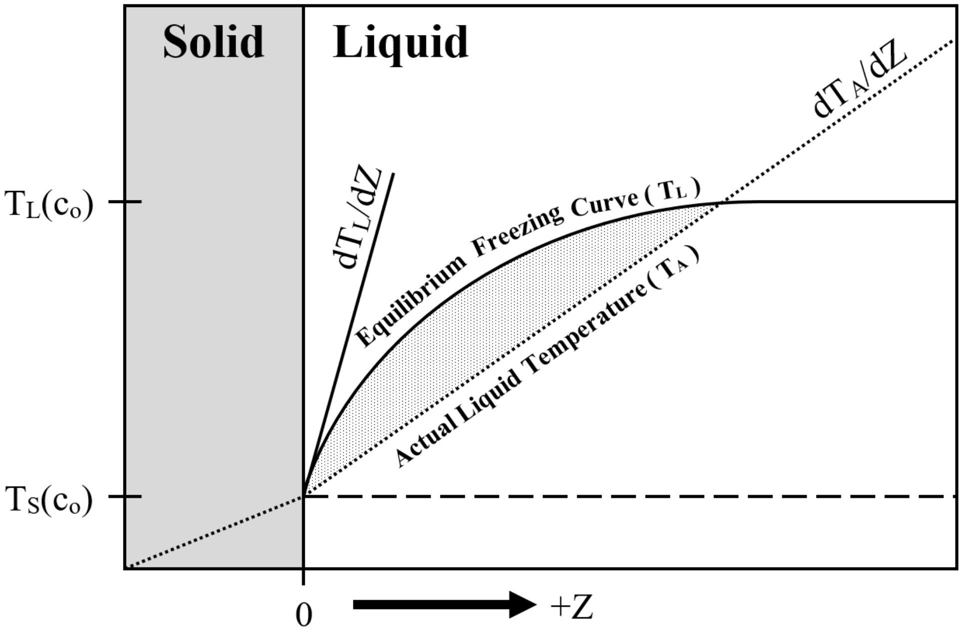

Figure 1.8. Constitutional undercooling that occurs in alloys.

The criterion for constitutional undercooling where the thermal gradient of the liquid (*dT_A/dZ*) is less than the slope of liquidus temperature (*dT_L/dZ*) thus resulting in instability can be rewritten such that:[45]

$$\frac{G}{V} < \frac{mc_o(k-1)}{k * D} \tag{17}$$

where: G is the temperature gradient in K/mm at the solid-liquid interface in the liquid; V is the solidification/growth rate of the solid-liquid interface in mm/s; m is the liquidus slope in K/wt.%; c_o is the initial alloy composition in wt.%; k is the partition coefficient that defines the extent of solute segregation; D is the diffusion coefficient in mm^2/s. It can be observed from Eq. (17) that high solidification velocities and/or low thermal gradients will increase the extent of the constitutionally undercooled region thus promoting instability. The morphology of perturbations that continue to grow because of the constitutionally undercooled liquid ahead of the solid-liquid interface is dependent upon the thermal gradient (G) in the melt and the growth rate (V) of the solid interface as is shown in Figure 1.9.

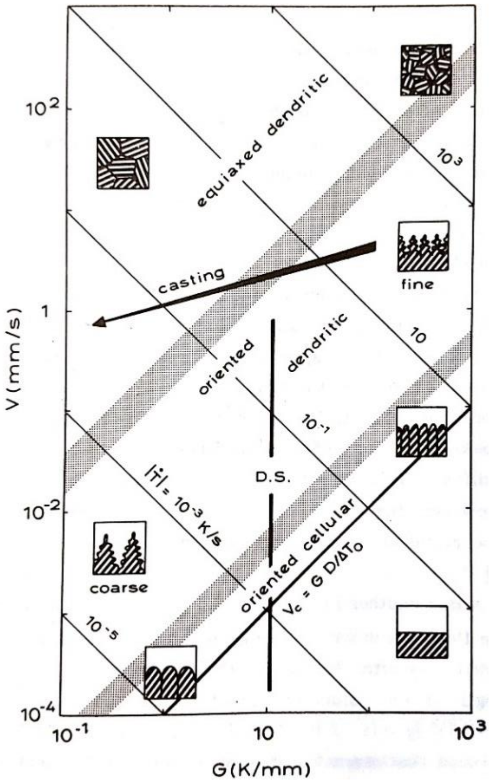

Figure 1.9. Summary of single-phase solidification morphologies with some degree of liquid undercooling at different growth rates (V) and thermal gradients (G).[45]

The product of $G*V$ is the cooling rate, $\dot{T}$, which controls how fine or coarse the microstructure will be. Cellular microstructures persist at high G/V ratios assuming there is some degree of liquid undercooling that causes instability of the growing planar interface. The cells begin to develop secondary arms at low thermal gradients, and at even lower thermal gradients tertiary arms (i.e. dendrites) begin to form.[37] The transition from cellular to columnar dendritic to equiaxed dendritic morphology occurs as the solidification rates are increased. The directional solidification method (*D.S.*) can be used to adjust solidification rate at a fixed thermal gradient thus achieving a desired microstructure with optimum properties. In a sand casting, the G and V terms tend to be interrelated by the heat flux out of the mold and the thermal properties of the metal.[45] Therefore, only the G/V conditions close to the arrow in Figure 1.9 can be utilized for modifying the morphology (only columnar and/or equiaxed dendritic microstructure). Additional discussion of the theoretical aspects of growth morphologies can be found in the works of Chalmers, Flemings, and Kurz and Fisher.[43-45]

1.4.5. Columnar-to-Equiaxed Transition (CET). A more detailed model beyond just G/V conditions is required to describe the transition from columnar dendritic to equiaxed dendritic microstructure when heterogeneous nuclei are present in the melt. Equiaxed grain structure is typically enhanced by either strong convection (fragmentation of dendrites from the mold wall into the melt) or inoculation treatment (introducing heterogeneous nuclei into the melt). The earliest work to thermally and chemically model the CET under realistic casting conditions was performed by J.D. Hunt.[49] In his work, the interaction of the columnar front with equiaxed grains formed by heterogeneous nuclei was examined. Using an analytical approach to study single-phase dendritic and eutectic columnar growth in an Al-Cu alloy, J.D. Hunt was able to describe a variety of variables that effect the position of the CET in the solidified alloy. These variables include growth velocity, temperature gradient, alloy composition, number of nuclei, and type of nuclei. Hunt suggested that growing columnar grains can only be stopped if a critical volume fraction of equiaxed grains exist in the melt ahead of the growing columnar front. This volume fraction was theoretically estimated to be 0.49 which corresponds to the value of the thermal gradient G in Eq. (18) required to stop columnar growth (i.e. fully equiaxed growth occurs):

$$G < 0.617 {N_o}^{1/3} \left\{ 1 - \frac{(\Delta T_N)^3}{(\Delta T_C)^3} \right\} \Delta T_C \tag{18}$$

where: N_o is the heterogeneous nuclei density per unit volume; ΔT_N is the undercooling required for heterogeneous nucleation; and ΔT_C is the constitutional undercooling at the dendrite tips. Considering the thermal conditions and redistribution of alloying elements in multi-component alloys, Eq. (18) was rewritten to a form in Eq. (19), which is known as the Hunt's Criterion for CET:

$$G/V^{0.5} < 0.617 {N_o}^{1/3} C_o \left\{ \frac{8m(k-1)\Gamma}{D} \right\} \tag{19}$$

where: V is the dendrite tip velocity; C_o the alloy composition; m the liquidus slope; k the distribution coefficient; D the liquid diffusion coefficient; and Γ the Gibbs-Thomson parameter. This equation is similar to the criterion for constitutional undercooling previously discussed, but has been modified to include heterogeneous nuclei density within the melt. It can be observed from this equation that fully equiaxed dendritic growth will dominate at low thermal gradients and/or high growth rates (established by mold and alloy conditions), high heterogeneous nuclei densities (controlled by convective flow or inoculation treatments), and high undercooling (controlled by alloy composition).

1.5. AUSTENITIC STAINLESS STEEL

The composition, properties, and solidification behavior of the austenitic alloys investigated in this research are discussed in this section.

1.5.1. Composition and Properties. These stainless steels are known to be formable, weldable, non-magnetic, operate under extreme temperature conditions without losing their strength and ductility (cryogenic to red-hot temperatures), and have high corrosion resistance. The most common grades produced are the 300-series with the most popular being 304 and 316 stainless steel. Chromium, molybdenum, and nitrogen contribute to the 300-series corrosion resistance properties while nickel and other austenite stabilizers are used to stabilize the austenitic structure. Other elements can be added to achieve specific material properties such as copper which promotes resistance of the alloy to sulfuric acid. Austenitic stainless steels can be soft (yield strength of 200 MPa) or made remarkably strong by cold working (yield strengths over 2,000 MPa).[3] The relative weaknesses of this alloy are less resistant to cyclic oxidation than ferritic grades, are prone to stress corrosion cracking (SCC) if corrosion cannot be resisted, and a susceptibility to thermal fatigue. All of these weaknesses can be mitigated with the proper precautions.

In general, the appropriate stainless steel grade is selected based on its ability to resist corrosion in the environment it is to be used in. The alloy that yields the cheapest production cost is the next important criteria for selecting an appropriate grade. Although the ferritic stainless steels have comparable corrosion resistance at a fraction of the cost of austenitic stainless steels, their lack of toughness, ductility, and susceptibility to high-temperature embrittling phases make them unsuitable for some applications. Martensitic grades are an adequate substitute for austenitic grades if mechanical properties and more important than corrosion resistance. However, in comparison with other stainless steels, austenitic grades are superior in both corrosion resistance while maintaining excellent mechanical properties. The austenitic alloys can have compositions anywhere in the region labeled 'Austenite' shown in Figure 1.10.[3] In this research, the primary stainless steel grades of interest are 316L (low carbon) and superaustenitic (similar composition to CK3MCuN). These alloys have base compositions of *16Cr-10Ni-2Mo* for 316L and *19Cr-17Ni-6Mo* for superaustenitic. The superaustenitic alloy offers superior corrosion resistance in comparison to the 300-series austenitic grades because of its higher alloying contents including chromium, molybdenum, nitrogen, and copper.

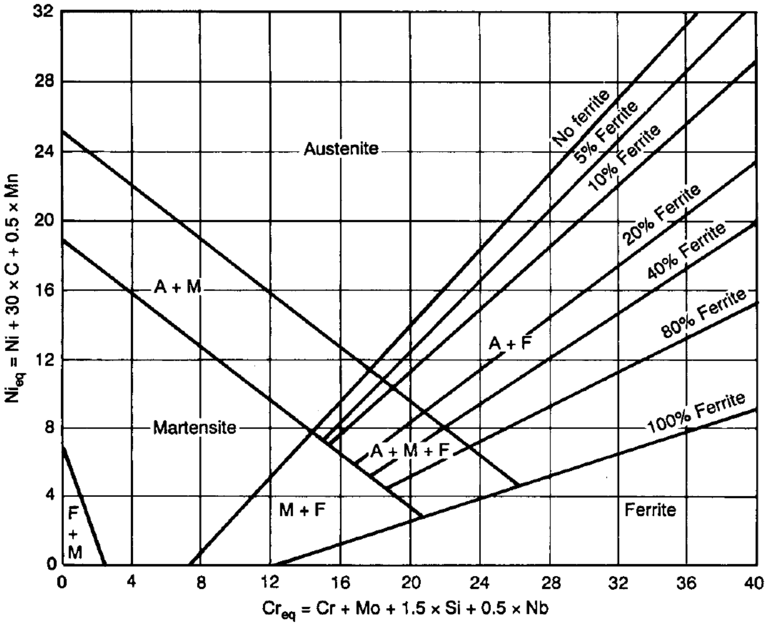

Figure 1.10. Schaeffler-Delong diagram showing the phases present in solidified, as-cast stainless steel at room temperature.[3]

1.5.2. Solidification Behavior. The phase diagram provided in Figure 1.11 illustrates the differences in solidification between austenitic and ferritic grades. Ferritic grades have higher chromium contents which stabilizes *δ-ferrite* while austenitic grades have higher nickel contents which stabilizes *γ-austenite*. These two grades will often solidify with only a single phase from liquid to room temperature. Therefore, grain refinement by heat treatment in these alloys is not possible.

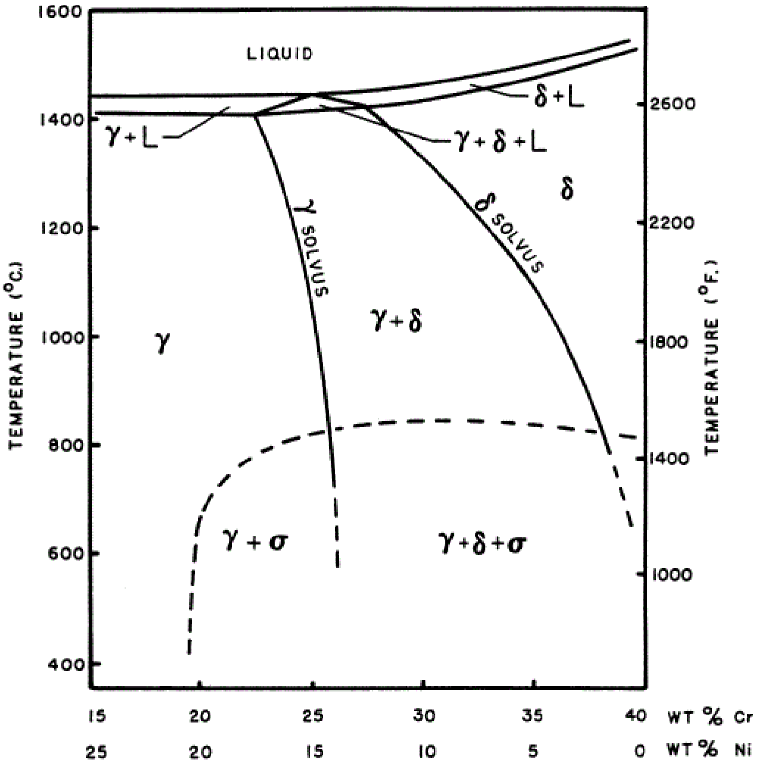

Figure 1.11. *Fe-Cr-Ni* pseudo-binary phase diagram for stainless steel at 60 wt.% *Fe*.[3]

Due to the high alloying contents of stainless steel, segregation of elements to the interdendritic regions is inevitable. The extent of segregation is largely dependent upon alloy composition and cooling rate from the melt to room temperature. At lower temperatures, these segregated regions can decompose to form *Mo*-rich σ-phase given the stainless steel possesses some amount of molybdenum in its composition. This phase is brittle and is detrimental to the alloys mechanical properties such as toughness, ductility, and corrosion resistance. Furthermore, carbon and nitrogen in the alloy have a high affinity with chromium which can result in the formation of chromium carbides and nitrides once these elements reach supersaturation in austenite.[3] These phases precipitate at the grain boundaries since grain boundary diffusion at lower temperatures occurs much more rapidly than diffusion through the bulk. As a result, the grain boundaries are depleted of chromium in the solid solution which results in preferential corrosion at the grain boundaries. Other secondary phases that have the potential to form in austenitic stainless steels are outlined in Table 1.3.

Table 1.3. Potential secondary phases that form in austenitic stainless steel.[3]

Precipitate	Crystal Type	Composition
NbC	Fcc	NbC
NbN	Fcc	NbN
TiC	Fcc	TiC
TiN	Fcc	TiN
Z-phase	Tetragonal	CrNbN
$M_{23}C_6$	Fcc	$Cr_{16}Fe_5Mo_2C$
M_6C	Diamond Cubic	$(FeCr)_{21}Mo_3C$; Fe_3Nb_3C; M_5SiC
σ-phase	Tetragonal	Fe, Ni, Cr, Mo
Laves phase	Hexagonal	Fe_2Mo, Fe_2Nb
χ-phase	Bcc	$Fe_{36}Cr_{12}Mo_{10}$
G-phase	Fcc	$Ni_{16}Nb_6Si_7$, $Ni_{16}Ti_6$ Si_7

Heat treatment of austenitic stainless steels is imperative for optimizing the mechanical and corrosion properties of the alloy. Heat treatment allows for the dissolution of secondary phases followed by homogenization of the matrix by grain boundary and bulk diffusion. Redistribution of chromium and molybdenum greatly reduces preferential corrosion at the grain boundaries thus improving overall corrosion resistance of the alloy. However, effective heat treatments of austenitic grades require high temperatures (> 1,000 ^oC) and long holding times (minimum of 4 hours) because the large atomic number elements *Cr* and *Mo* diffuse slowly. Therefore, these processes can be quite costly.

1.6. PURPOSE STATEMENT

The goal of this research project is to develop an industrially viable melting process that will control the crystallization macrostructure of austenitic grades of cast steels. Titanium nitride (*TiN*) has proven to be an effective grain refiner of austenite, and spinel ($MgAl_2O_4$) is known to be a favorable site for the epitaxial growth of titanium nitride. Theoretical simulation and experimental application has led to the development of a repeatable grain refining melt process for austenitic stainless steel alloys. The general methodologies of thermodynamic simulation, heat design, and analysis method of the final casting which was conducted as a part of this research will be reviewed. More specific topics and analysis methods pertaining to this research are discussed in the attached publications. This includes other simulation softwares, experimental techniques such as differential scanning calorimetry (DSC), and the variety of methods used to characterize the properties of superaustenitic stainless steel alloy.

2. METHODOLOGY

2.1. THERMODYNAMIC SIMULATION

The following thermodynamic software packages were used to simulate phases formed in the experimental heats of this research.

2.1.1. FactSage Software. Figure 2.1 shows the precipitation sequence of inclusions simulated with FactSage 7.0 using FactPs and FSstel databases during ladle treatment of a stainless steel melt for three dissolved nitrogen contents. This includes the initial formation of spinel inclusions in the melt, followed by *TiN* co-precipitation on spinel in the melt before solidification begins. These thermodynamic predictions are used to estimate the quantity of *TiN* and *Mg-Al* spinel oxides that form in the melt prior to solidification. This proves useful when targeting the formation of a specific amount of nuclei and other potential inclusions that may form within the melt.

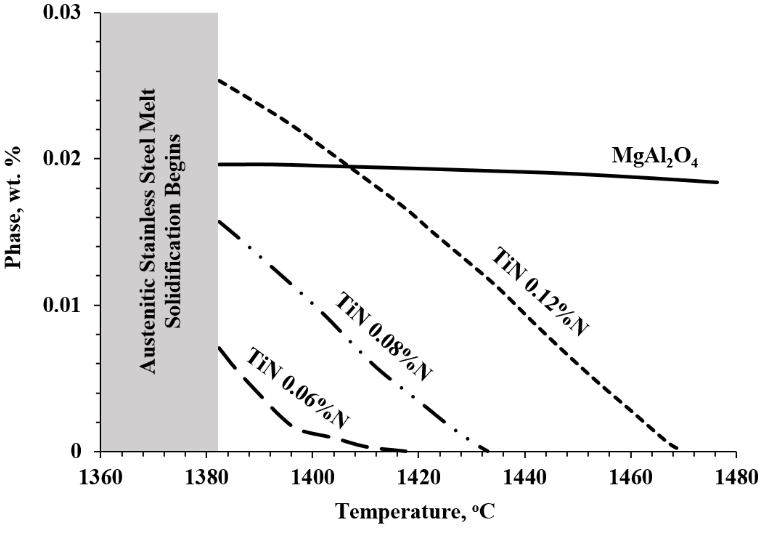

Figure 2.1. Simulated precipitate formation during ladle treatment of the melt prior to solidification.

This software was also used to generate phase stability diagrams for both *Mg-Al* spinel and *TiN* precipitates in the stainless steel melt which are shown in Figure 2.2 and Figure 2.3 respectively. These diagrams prove useful when optimizing the amount of melt additions required to form the desired nuclei. It shows the regions of dissolved *Mg-Al* and *Ti-N* in the melt that is necessary to form the desired phase. In the case of spinel oxide, the incorrect ratio of *Mg-Al* additions will result in either the formation of magnesia, alumina, nonstoichiometric formation of spinel, or the elements will remain dissolved in the solid solution. In the optimized scenario, the only phase to form from these additions will be spinel oxide.

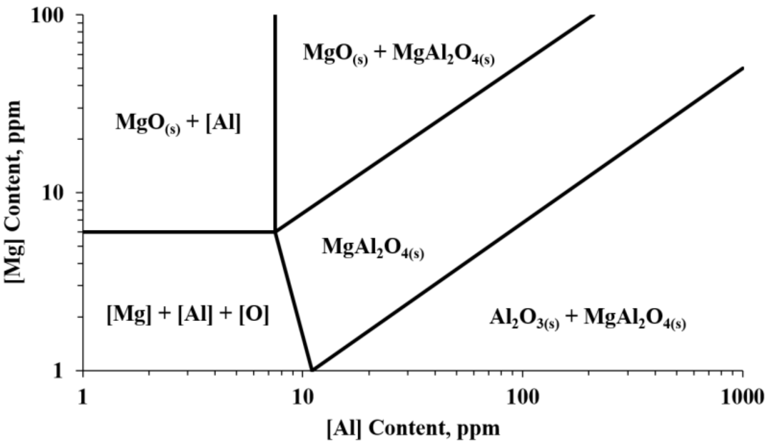

Figure 2.2. Simulated phase stability diagram for *Mg-Al* spinel oxide in austenitic stainless steel melt.

Sequential addition of *Mg-Al* (forming spinel oxide first) followed by addition of titanium (nitrogen is already in the melt) will prevent the oxidation of titanium thus improving recovery. This is illustrated in Figure 2.3 which shows the equilibrium curve for *TiN* formation shifts right as the dissolved oxygen content in the melt is increased. This means that larger titanium additions are required to form *TiN* precipitates because the dissolved titanium is being tied up in the formation of titanium oxides. Therefore, oxygen control is a crucial aspect of the designed grain refining melt treatment.

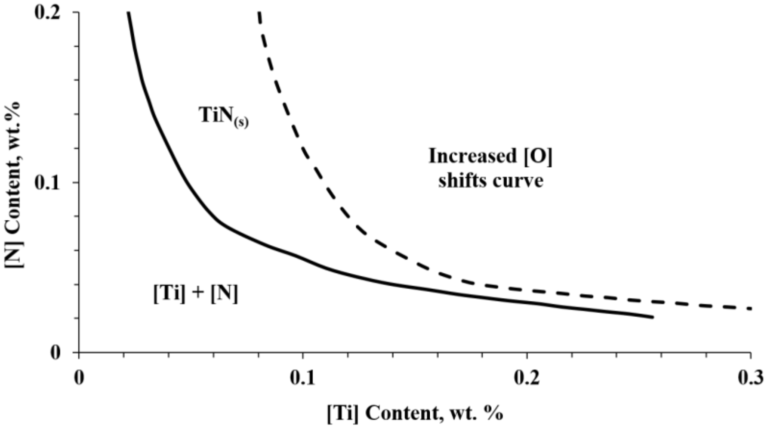

Figure 2.3. Simulated phase stability diagram for *TiN* precipitate in austenitic stainless steel melt.

2.1.2. Thermo-Calc Software. This software was particularly useful in the design of *Ni*-based master alloys because of the availability of TCNI8: Ni-Alloys v8.0 database. Additional solidification simulations of the stainless steel melt were performed with Thermo-Calc 2016a software using TCFE8: Steels/*Fe*-Alloys database. These results were occasionally compared with FactSage 7.0 simulations to verify phase formation during solidification of the melt and cooling of the casting. Figure 2.4 shows a solidification simulation of a stainless steel melt performed with Thermo-Calc 2016a. This particular alloy demonstrated the simultaneous solidification of two solid phases (austenite and ferrite) from the liquid which was then followed by solid-solid transformations (ferrite→austenite) upon cooling of the casting to room temperature.

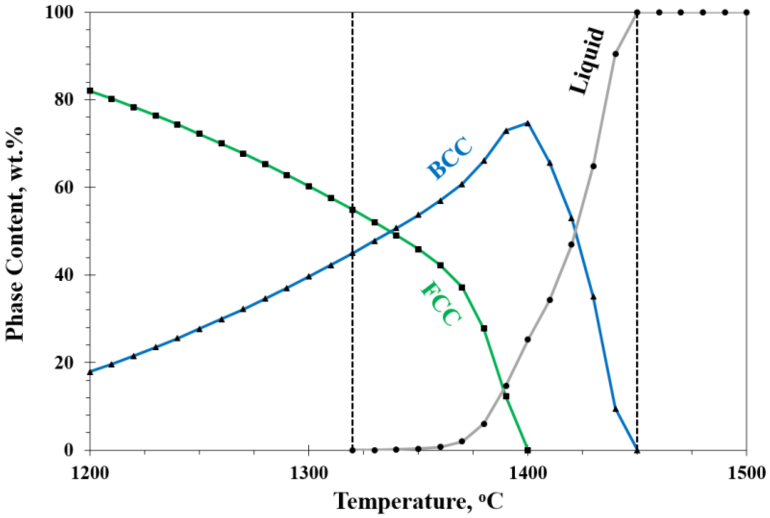

Figure 2.4. Simulated solidification sequence of solid phases in austenitic stainless steel melt.

2.2. HEAT DESIGN

The charge materials used, melting procedure, and mold design of each experimental heat is detailed in this section.

2.2.1. Charge Materials. Experimental heats assembled with synthetic, pure charge materials consisted of specific quantities of induction iron, low carbon ferrochrome, electrolytic nickel, ferromolybdenum, electrolytic manganese, and ferrosilicon. These materials were melted in a 45 kg (100 lb) capacity induction furnace. Grain refining additions consisted of nitride ferrochrome, ferrotitanium, nickel magnesium, and pure aluminum. The most common composition investigated in this research was 316L alloy, however, superaustenitic alloy (similar to CK3MCuN composition) was also explored. Industrial sponsors provided two industrial charge materials that were from different operations: foundry and mini-mill. These compositions are confidential, but result in a fully austenitic cast structure.

2.2.2. Melt Practice. Theoretical development, simulation, and experimentation, performed in past research for this project, has proven that titanium nitride is an effective grain refiner of 316L austenitic stainless steel castings. Furthermore, the presence of spinel precipitates in the melt act as heterogeneous nuclei for the nucleation and growth of titanium nitride. This co-precipitation is favorable to occur because the lattice disregistry between spinel and titanium nitride is low.[50] Therefore, a grain refining melt process was developed that implements the epitaxial growth of titanium nitride on spinel particles in 316L austenitic stainless steel melts. Illustration of this designed melting procedure is shown in Figure 2.5. The other processing route for grain refining treatment of the melt includes the addition of master alloy containing preformed *TiN* nuclei into the ladle which is also shown in Figure 2.5. The top of the induction furnace is shrouded in argon gas to prevent interaction with the atmosphere. The charge is melted, de-oxidized with aluminum, calcium treated, and argon stirred, to produce a melt with low dissolved oxygen, sulfur, and inclusion contents.

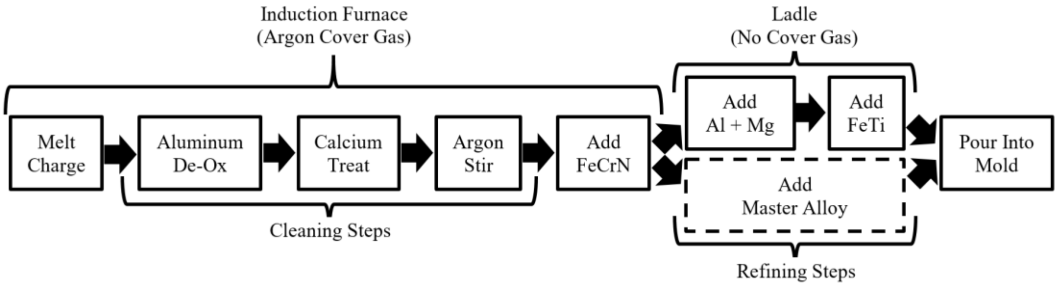

Figure 2.5. Designed grain refining melt process.

Argon stirring helps remove de-oxidation reactant products, and pre-existing inclusions out of the melt. Nitrogen is then dissolved into the melt using an addition of nitrided ferrochrome alloy in the furnace. The melt is deslagged, and the furnace is tapped into a ladle. Ideally, most of the dissolved oxygen picked up by the melt during the furnace to ladle transfer is consumed by the formation of spinel upon the first ladle addition of aluminum and magnesium. Therefore, the second ladle addition of titanium has little potential to oxidize. Titanium reacts with the dissolved nitrogen in the melt to form titanium nitride, which co-precipitates on the surfaces of existing spinel particles. The melt is then poured into a no-bake sand mold at a temperature that is approximately 100 ^{o}C superheat. A low superheat minimizes the number of inclusions formed prior to solidification and is used to keep the inclusions well-dispersed throughout the casting.

Two sand mold designs were used in this project and are shown in Figure 2.6. These molds produce a heavy section, cylindrical casting with dimensions of 100 mm (4 in.) diameter and a 200 mm (8 in.) height. An insulated riser dome is used to manage thermal conditions within the mold to ensure that final solidification of the liquid metal occurs in the riser thus minimizing porosity in the casting. The riser dome has approximate dimensions of 150 mm (6 in.) diameter and 100 mm (4 in.) height. For the bottom chilled mold (Figure 2.6(a)), the bottom of the vertical cylinder is designed with a rim that has a 5” (127 mm) diameter and ¼” (6 mm) height which maximizes contact area of the casting with the water cooled, chill plate thus increasing the cooling rate. A side gating system was used to prevent additional heating of the chill plate when pouring. For the sand mold (Figure 2.6(b)), the combined height of the pouring cup and sprue is greater than 300 mm (12 in.) to ensure complete filling of the mold cavity. It is a bottom-filled gating system with the runner positioned tangent to the cylindrical mold cavity to promote mixing inside the mold which helps keep inclusions well-dispersed throughout the solidified casting.

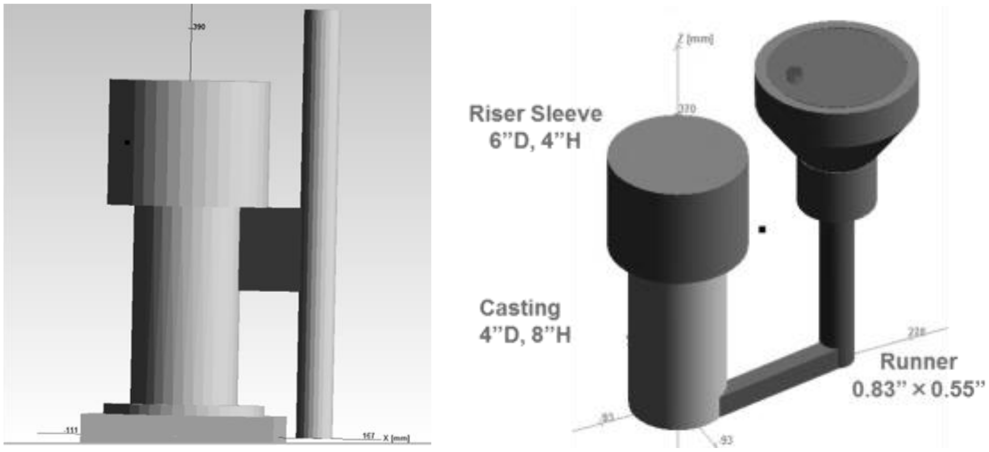

(a) (b)

Figure 2.6. CAD model of (a) bottom chilled mold and (b) no-bake sand mold.

2.3. PRIMARY ANALYSIS

Every casting produced in this research underwent the same primary analysis outlined in this section. This includes chemical composition, inclusion analysis, and etching the macrostructure. Details of additional analyzes performed are covered in the publications attached to this thesis.

2.3.1. Chemical Composition. Chemistry values of the experimental castings were verified using a Spectrometer, LECO C-S combustion analyzer, and LECO N-O combustion analyzer. Samples were taken from the casting at heights of 1 inch, 3 inch, and 5 inch with relation to the bottom of the mold. The chemistry at each height was sampled three to five times, and then averaged into a single chemistry value. The chemistry value from each height was then averaged together to estimate the chemistry of the overall casting. Additional chemistry samples were taken from the induction furnace and ladle sometimes even at every step in the melt process outlined in Figure 2.5.

2.3.2. Inclusion Analysis. ASPEX SEM/EDX was used to classify and quantify large populations of inclusions. Samples were taken from the casting at heights of 1 inch, 3 inch, and 5 inch with relation to the bottom of the mold. Additional samples were taken from the furnace and ladle. A set of 2,000 inclusions were recorded for each sample. This provided information about inclusion density present throughout the casting. It also provided insight into the evolution of inclusions through each step of the melt process. Inclusion analyzer software developed by the university was used to process ASPEX data. This software provided a variety of statistics in regard to the inclusions contained within the sample being analyzed (inclusion composition via EDX, content, size, nearest neighboring distance, etc.). It also produced ternary plots that were used to identify the primary class of inclusion families within the sample. A sample ternary diagram produced by the inclusion analyzer software is provided in Figure 2.7. This plot shows both the composition and size of the recorded inclusions. ASPEX was also used to gather qualitative information such as SEM images of extracted inclusions, segregated regions, polished samples, and fracture surface. Additional information and procedures of ASPEX inclusion analysis are discussed in detail by Harris et al..[51]

2.3.3. Macro-etched Images. The extent of grain refinement was determined by sectioning and macro-etching each casting to reveal the macrostructure. A solution of 5 parts hydrochloric acid, 2 parts hydrogen peroxide, and 3 parts distilled water was used for etching these samples. Samples had to be cut from the cast, milled, and surface ground before being etched. The etching solution would dissolve the grain boundaries thus revealing the grain structure. Optical images of the macrostructure were taken using a combination of red, green, and/or blue light filters to reveal grain orientations. Each color of light is reflected by different grain orientations thus allowing each grain to be differentiated from one another.

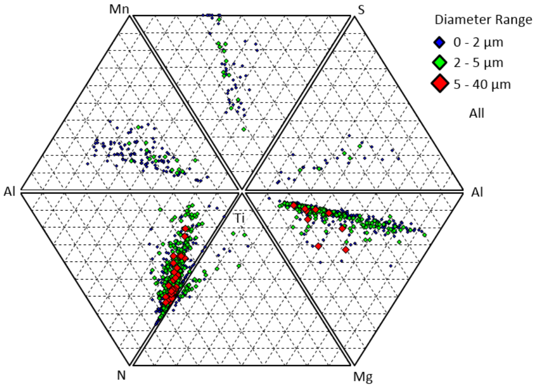

Figure 2.7. Ternary diagram of sample taken from the casting produced by inclusion analyzer software using ASPEX data.

Two macro-etched, vertical cross-sections of austenitic stainless steel castings showing the difference between a columnar and equiaxed structure are provided in Figure 2.8.

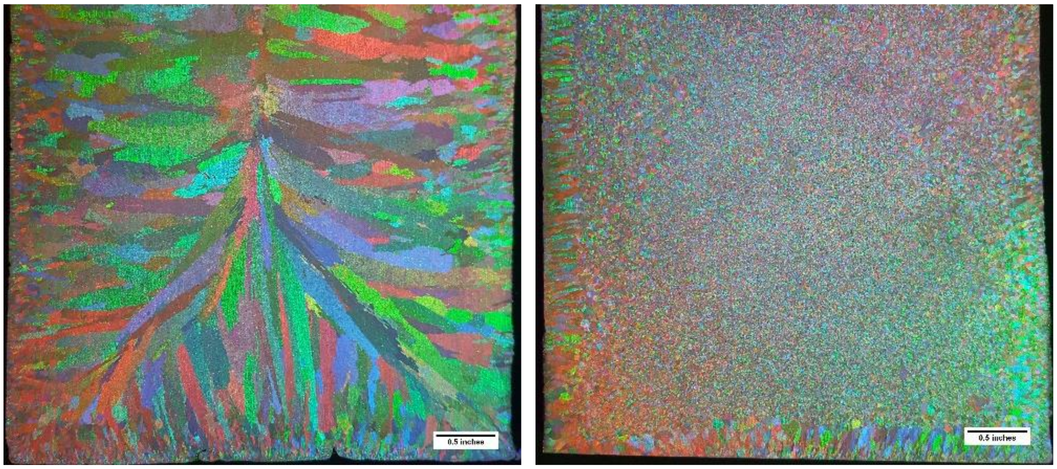

Figure 2.8. Etched macrostructure of austenitic stainless steel showing a columnar structure (left) and an equiaxed structure (right).

3. SUMMARY OF PAPERS

PAPER I: Effect of Phase Solidification Sequence in Stainless Steel on Grain Refining Efficiency

Paper I was submitted and presented at the AISTech Conference in Philadelphia, Pennsylvania on May 8, 2018. Grain refinement of the as-cast structure of *Cr-Ni* stainless steel alloys solidified with primary *FCC*, *BCC* and mixed *FCC/BCC* phases was experimentally studied using a melt treatment that promotes the formation of heterogeneous nuclei. Refinement of the primary solid phases was achieved in both cast ferritic and austenitic grades. However, imposing a mixed solidification sequence of *FCC* and *BCC* phases resulted in a macrostructure without a recognizable Columnar-to-Equiaxed Transition zone (CET). This behavior was explained by the independence of growth between the primary ferrite and secondary austenite phases which results in more difficult thermal and growth conditions for equiaxed growth of the secondary phase.

PAPER II: Two Inoculation Methods for Refining As-cast Grain Structure in Austenitic 316L Steel

Paper II is currently under review for submission to International Journal of Metalcasting (IJMC). Two inoculation methods were utilized to introduce titanium nitride (*TiN*) particles into an AISI 316L steel melt to refine the as-cast grain structure during solidification. The first inoculation method is based on *in-situ* formation of heterogeneous nuclei by *TiN* co-precipitation on preexisting *Mg-Al* spinel inclusions. The second inoculation method used a newly developed master alloy that contains *TiN* precipitates which was added in the ladle during furnace tapping. Grain refinement of the cast macrostructure was observed with both methods. The *in-situ* method provided finer equiaxed grains than the master alloy method, while a thicker zone with columnar grains next to the chill was observed. The master alloy method eliminated the need for spinel, gave better control of the amount and size of heterogeneous nuclei, and reduced clustering tendency in comparison to the *in-situ* method. However, the *in-situ* formed nuclei method is more effective to refine grain size. The effects of contact angle and nuclei surface geometry on the activity of heterogeneous nucleation were discussed.

PAPER III: Effect of Grain Refining on Properties of Superaustenitic Stainless Steel

Paper III is currently under review for submission to Journal of Materials Engineering and Performance (JMEP). A grain refined structure in high alloy *19Cr-17Ni-6Mo* superaustenitic stainless steel was achieved by applying melt inoculation treatment. Another casting of the same alloy was cast without an inoculation treatment. These castings were subjected to a typical homogenization heat treatment that is used in industry for superaustenitic steels. No coarsening or additional refining of the as-cast grain structure were observed in either the base or grain refined steels. It was found that the grain refined structure was more effective at reducing interdendritic segregation after heat treatment than the unmodified steel. Characterization of the properties for both scenarios in the heat-treated condition revealed improvements in ultimate tensile strength, ductility, yield strength, machinability, and intergranular corrosion rate for the refined material. However, the refined scenario experienced a subsequent decrease in toughness and an increase in mass loss from pitting corrosion likely caused by the grain refining additions.

PAPER

I. EFFECT OF PHASE SOLIDIFICATION SEQUENCE IN STAINLESS STEEL ON GRAIN REFINING EFFICIENCY

Dustin A. Arvola, Ronald J. O'Malley, Simon N. Lekakh, Laura N. Bartlett

Missouri University of Science and Technology

Materials Science & Engineering Dept.

1400 N Bishop, Rolla, MO, U.S.A., 65409

Keywords: solidification, columnar, equiaxed, macrostructure, grain refinement, CET

ABSTRACT

Grain refinement of the as-cast structure of *Cr-Ni* stainless steel alloys solidified with primary *FCC*, *BCC* and mixed *FCC/BCC* phases was experimentally studied using a melt treatment that promotes the formation of heterogeneous nuclei. This melt treatment was designed using solidification simulations with FactSage 7.0 thermodynamic software. Refinement of the primary solid phases was achieved in both cast ferritic and austenitic grades. However, imposing a mixed solidification sequence of *FCC* and *BC*C phases resulted in a macrostructure without a recognizable Columnar-to-Equiaxed Transition zone (CET). Non-metallic inclusions in the casting were analyzed using automated SEM/EDS method, and compared with the thermodynamic simulations. A computational fluid dynamics (CFD) analysis was employed using ANSYS 18.1 Fluent software to simulate

the thermal gradient (*G*) and isotherm velocity (*V*) in the casting, and their values were plotted on a Hunt's criteria map and compared qualitatively to experimental CET position for the different steels.

1. INTRODUCTION

The macrostructure of a stainless steel casting is typically characterized by three distinct regions of grain structure. The first is the chill zone, which occurs at the mold interface where solidification begins. These grains tend to be small in size because of high solidification rates and high undercooling of the melt near the mold wall. Some of these grains manage to continue growing into the melt as dendrites. These dendrites form the second zone, which contains a columnar grain structure. If favored, these grains will grow until all the liquid metal is fully consumed. However, this columnar growth can be impeded by the formation of equiaxed grains in the third zone in the melt ahead of the growing columnar dendrites. Equiaxed grains can form when thermal conditions are favorable and/or effective heterogeneous nuclei are present to encourage the nucleation of solid within the melt. Grain refinement promotes a large equiaxed zone which, in some cases, can completely suppress growth of the columnar zone.[1] This manipulation of grain size and shape affects both the castability and mechanical properties of the final steel casting, and is therefore a crucial aspect of the casting process.[2,3]

Numerous studies have been conducted to better understand how to control the Columnar-to-Equiaxed Transition zone (CET) in a variety of metals. One grain refining technique commonly used in industry to control CET in aluminum alloys is the use of a TiB_2 inoculant to introduce solid heterogeneous nuclei in the liquid metal or by forming heterogeneous nuclei in-situ in the liquid.[4,5] This solidification-based grain refining technique is a flexible and low-cost method for steel mills and steel foundries to improve the properties of their final product compared to heat treatment, which is high cost. However, for heterogeneous nucleation to be effective, several factors must be taken into consideration. (1) The nuclei must survive long enough for nucleation of the desired phase to occur. Preferably, the nuclei should be stable at the temperature when inoculation occurs thus limiting the potential for dissolution of the solid particle back into the melt. (2) The nuclei must have a low lattice disregistry or similar crystal structure with the nucleating phase. (3) A low interfacial energy that promotes nucleation of the desired phase on to the surface of the nuclei must exist. In comparison to nonferrous metals, steels have a significantly higher melting temperature. Therefore, the types of inclusions that satisfy the previously listed factors while also surviving at steelmaking temperatures are limited.[6-8] In addition, alloying elements in steel can affect both solidification behavior and solid-state reactions. This makes selecting an effective heterogeneous nucleant even more difficult because of the potential for multiple phases changing, forming, competing, and/or interacting in the melt upon solidification.

In this study, a grain refining process was applied to three Cr-Ni stainless steel alloys that each target a different solidification sequence: primary ferrite, primary austenite, and mixed ferrite→austenite (F→A) solidification mode. The purpose of these experiments was to determine the effect of solidification sequence on grain refining capability for a specifically designed grain refining melt practice. The tools used for this investigation include thermodynamic software, SEM/EDS inclusion classification, EBSD grain orientation, and Differential Scanning Calorimetry (DSC). A computational fluid *dynamics (CFD) analysis was performed using ANSYS 18.1 Fluent software to estimate the thermal gradient (G) and isotherm velocity (V) vs. position in the mold during solidification. These values of G and V were then plotted using Hunt's Criterion to estimate the grain refining capability for stainless steel alloys with ferritic, austenitic, and mixed F→A solidification modes.*

2. METHODOLOGY

2.1. GRAIN REFINING PROCESS

Grain refinement of cast ferritic stainless steel by titanium nitride has proven to be highly effective in recent studies.[9,10] Research conducted by the authors has shown that titanium nitride nuclei can grain refine as-cast austenitic stainless steels[11] as well as ferritic stainless steels. The authors also performed thermodynamic simulations to predict the precipitation sequence of heterogeneous nuclei during solidification of the melt. In this study, a grain refining method based on *in-situ* formation of titanium nitrides (TiN) on preexisting ($MgO{\cdot}Al_2O_3$) spinel inclusions using a controlled sequence of melt additions prior to casting.[11] This co-precipitation is favorable because the lattice disregistry between spinel and TiN is low (5.1%).[12] TiN co-precipitated on spinel inclusions then act as suitable heterogeneous nucleation sites for both solid ferrite and solid austenite phases based on a low lattice disregistry between TiN and the solid ferrite (3.9%) or solid austenite (7.7%) phases.[11] TiN is also stable in liquid steel at relatively low concentrations of dissolved titanium and nitrogen when compared to other potential heterogeneous nuclei.[9]

Schematic plot of the designed melting procedure is shown in Figure 1 and has been adopted for the use in this experiment. Figure 2 shows the precipitation sequence of inclusions simulated using FactSage 7.0 during ladle treatment of a stainless steel melt for three dissolved nitrogen contents. This includes the initial formation of spinel inclusions in the melt, followed by *TiN* co-precipitation on spinel in the melt before solidification begins.

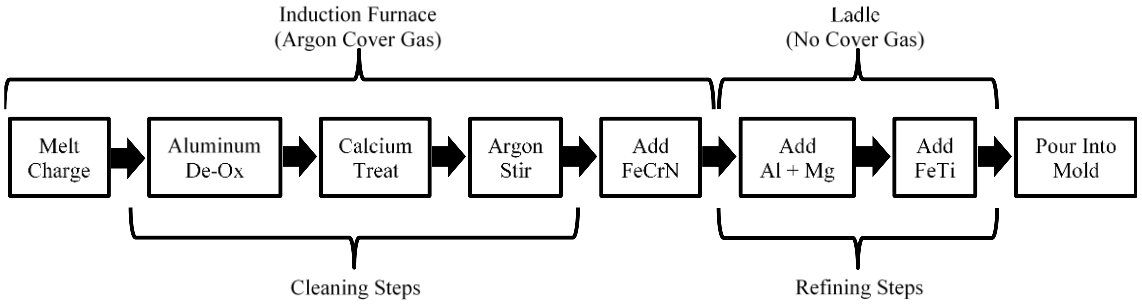

Figure 1. Designed solidification-based, grain refining melt practice targeting co-precipitated *TiN* nuclei.

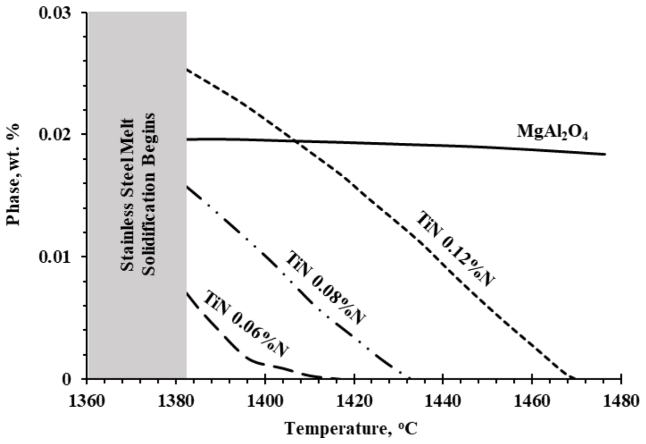

Figure 2. FactSage 7.1 simulated inclusion formation during ladle treatment of the melt prior to solidification.

2.2. EXPERIMENTAL SET-UP AND PROCEDURE

The charge for each experimental heat consisted of specific quantities of induction iron, low carbon ferrochrome, electrolytic nickel, ferromolybdenum, electrolytic manganese, and ferrosilicon. These materials were melted in a 45 kg (100 lb) capacity induction furnace. The top of the induction furnace was covered and shrouded in argon gas to reduce oxygen pickup from the atmosphere. The charge material was melted, de-oxidized with aluminum, calcium treated, and argon stirred to produce a melt with low dissolved oxygen, sulfur, and inclusion contents. Argon stirring was employed to remove de-oxidation products and pre-existing inclusions from the melt. Nitrogen was then dissolved into the melt using a nitrided ferrochrome alloy in the furnace. The melt was deslagged, and the furnace was then tapped into a ladle. The dissolved oxygen picked up by the melt during the furnace to ladle transfer was consumed by the oxidation of aluminum and magnesium during stage one ladle treatment to form spinel. The second ladle addition of ferrotitanium to introduce titanium to the melt was therefore protected from reoxidation improving Ti recovery. The titanium reacted with the dissolved nitrogen in the melt to form TiN, which then co-precipitated on the surfaces of the existing spinel inclusions. The melt was then poured into a no-bake sand mold at an aim temperature that was approximately 100 ^{o}C above the liquidus of the alloy. A consistent superheat was used to control the amount and size of inclusions prior to solidification in the mold, and to help prevent flotation or clustering of inclusions to keep the inclusions well-dispersed throughout the casting.

A CAD model of the no-bake sand mold is shown in Figure 3. This mold produces a heavy section, cylindrical casting with dimensions of 100 mm (4 in.) diameter and a 200 mm (8 in.) height. An insulated riser dome is used to manage thermal conditions within the mold to ensure that final solidification of the liquid metal occurs in the riser thus minimizing porosity in the casting. The riser dome has approximate dimensions of 150 mm

(6 in.) diameter and 100 mm (4 in.) height. The combined height of the pouring cup and sprue is greater than 300 mm (12 in.) to ensure complete filling of the mold cavity. It is a bottom-filled gating system with the runner positioned tangent to the cylindrical mold cavity to promote mixing inside the mold which helps keep inclusions well-dispersed throughout the solidified casting.

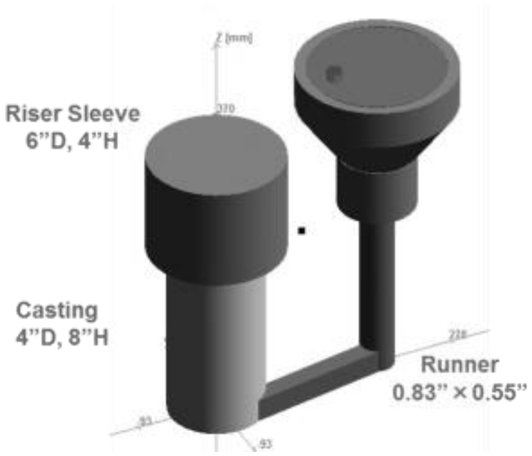

Figure 3. CAD Model of No-Bake Sand Mold.

2.3. TARGETED CHEMISTRY

Three experimental heats were performed using the same melt practice and amounts of additions made for cleaning and refining steps. Selected spinel and *TiN* content at liquidus were defined in previous research conducted for grain refining trials of CF3M (316L) grade stainless steel using similar mold design and grain refining practice. The only difference between the three heats described in this article is the initial metallic charge used to establish the base chemistry of the melt. The targeted base chemistries of these heats are listed in Table 1.

Table 1. Targeted base chemistry and inclusion content of experimental heats, wt.%.

Heat #	*C*	*Si*	*Mn*	*Cr*	*Mo*	*Ni*	$MgO\cdot Al_2O_3$	*TiN*	Primary Phase(s)
1	0.02	1.18	0.53	17.7	2.0	16.3	≈ 0.006	≈ 0.09	FCC
2	0.02	1.35	0.60	19.3	2.3	9.5			BCC+FCC
3	0.02	1.40	0.60	25.9	2.3	0.0			BCC

These chemistry values were selected based on equilibrium cooling calculations using Thermo-Calc 2016a software.[13] TCFE8: Steels/Fe-Alloys database was chosen for calculation of liquid and solid solutions in the melt. The results of phase content versus temperature calculated from the simulations can be seen in the plots of Figure 4.

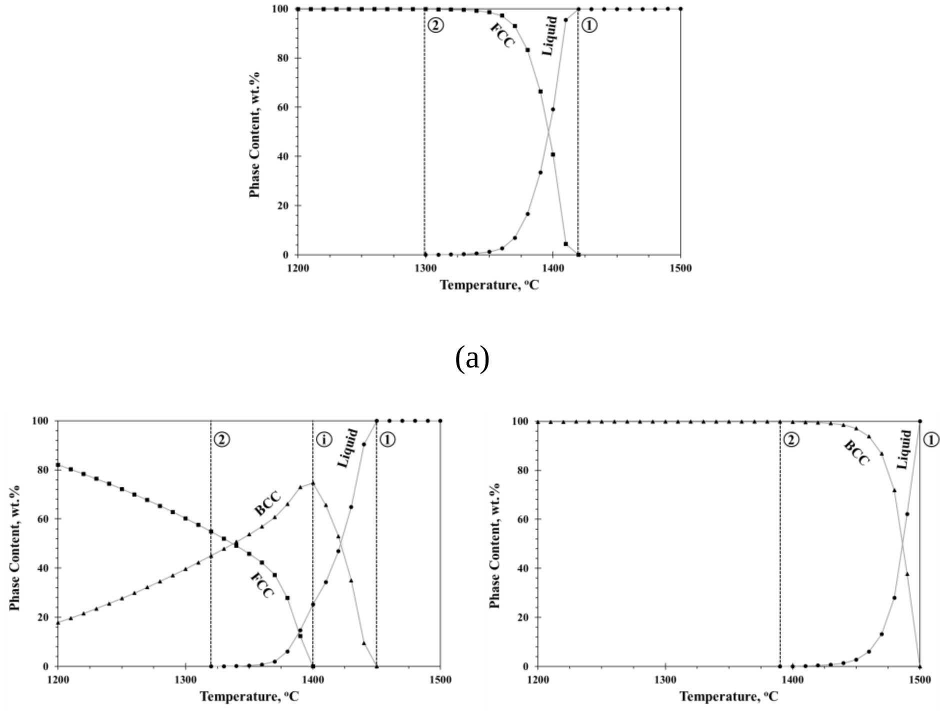

(a)

(b)

(c)

Figure 4. Phase formation upon equilibrium solidification and cooling of the melt at 1773 K (1500 °C) to 1473 K (1200 °C) for (a) Heat #1, (b) Heat #2, and (c) Heat #3.

From the plots, each heat exhibits a different solidification mode and cooling behavior. Austenitic heat #1 and ferritic heat #3 demonstrates a single-phase solidification mode from liquidus to solidus (①→②) temperatures. Heat #2 illustrates a more complex solidification and cooling path. The melt begins to solidify primary *δ-ferrite* phase at liquidus temperature till it reaches an intermediate temperature (①→ⓘ). At the intermediate temperature, secondary *γ-austenite* phase begins to solidify from the liquid. A series of phase transformations are possible from the intermediate to solidus (ⓘ→②) temperatures. Primary *δ-ferrite* phase begins to disappear in tandem with the liquid phase as secondary *γ-austenite* phase continues to form. This is a classical scenario of a peritectic reaction that has been observed to occur in certain grades of steel.[14] The peritectic phase transition has been interpreted to occur in the following series of events.[14,15] A thin film of *γ-austenite* begins to form at the interface between the liquid and *δ-ferrite* dendrite due to the peritectic reaction as a result of liquid super-saturation. Peritectic transformation starts once the *δ-ferrite* dendrite surface is completely covered with a thin *γ-austenite* film. These transformations occur by solid-solid reaction of the *δ-ferrite* dendrite to *γ-austenite* by diffusion through the peritectic phase and/or by continued solidification of *γ-austenite* into the liquid. However, regardless of the overall decline in the *δ-ferrite* phase, the formation of *δ-ferrite* phase from the liquid and/or by a eutectic reaction is also possible. Once the liquid disappears at solidus temperature, solid-solid transformation of *δ-ferrite* to *γ-austenite* continues till equilibrium is achieved or the temperature decreases to the point where diffusion can no longer drive the transformation. Potential reactions and transformations from the plots in Figure 4 are outlined in Table 2.

Table 2. Potential solidification and cooling behavior of experimental heats from simulations.

	Potential Reactions & Transformations				
Heat #	1600^{o}C→①	①→②	①→ⓘ	ⓘ→②[14,15]	②→1200^{o}C
1	L	L → γ	-	-	γ
2	L	-	L → δ	L → δ L→ δ + γ L + δ → γ L → γ δ → γ	δ → γ
3	L	L → δ	-	-	δ

3. RESULTS

3.1. CASTING CHEMISTRY AND INCLUSION ANALYSIS

Chemistry values were obtained using a Spectrometer, LECO C-S combustion analyzer, and LECO N-O combustion analyzer. Samples were taken at heights of 1 inch, 3 inch, and 5 inch with relation to the bottom of the casting. The chemistry at each height was sampled three to five times, and then averaged into a single chemistry value. The chemistry value from each height was then averaged together to estimate the chemistry of the overall casting. These values are summarized in Table 3. Actual casting chemistries nearly match the targeted base chemistry for each experimental heat.

Table 3. Casting chemistry from each experimental heat, wt.%.

Heat #	*C*	*Si*	*Mn*	*Cr*	*Mo*	*Ni*
1	0.038 ± 0.01	1.33 ± 0.04	0.43 ± 0.01	17.8 ± 0.1	2.1 ± 0.05	15.7 ± 0.1
2	0.034 ± 0.01	1.42 ± 0.03	0.51 ± 0.01	19.0 ± 0.2	2.3 ± 0.05	8.7 ± 0.1
3	0.036 ± 0.01	1.72 ± 0.04	0.57 ± 0.01	25.4 ± 0.1	2.5 ± 0.04	0.2 ± 0.0

Keeping all conditions the same for each heat is of crucial importance in examining the effect that changing charge chemistry, and therefore solidification sequence, has on the grain refining efficiency of the current developed grain refining process. This process targets the formation of *TiN* inclusions as heterogeneous nuclei. An analysis of samples taken at the center of each casting was performed to verify that similar nuclei conditions were achieved in each heat design. Counting and classifying inclusions was performed using an ASPEX SEM/EDX automated inclusion analyzer. A rule file was established with a carbon content limit to prevent recording porosity on the sample. A total of 2,000 inclusions were counted on a scan area between 5 to 8 mm^2 for each sample. Inclusions statistics for each sample are shown in Table 4.

Table 4. ASPEX inclusion analysis statistics taken from the center of the casting for each experimental heat.

Heat #	Scan Area, mm^2	Inclusion Total Area, µm^2	Inclusion Content, %	Inclusion Average Diameter, µm	NND of Inclusions, µm	Inclusion Density, #/mm^2
1	7.903	8,568	0.108	2.01 ± 1.15	23.2 ± 21.6	250
2	5.232	5,443	0.104	1.63 ± 0.90	22.6 ± 16.3	374
3	6.454	6,889	0.107	1.77 ± 1.09	22.7 ± 18.2	307

The total area of inclusions recorded was divided by the scan area to estimate inclusion content. These values were consistent for each heat at approximately 0.1%. This means that each sample has a similar area fraction of inclusions. The average diameter and nearest neighboring distance (NND) of the recorded inclusions is also similar between samples. Small average diameter (< 3μm) and large NND (> 20μm) suggests that the inclusions are well-dispersed throughout the casting. However, the differences in inclusion density for each sample indicates that the inclusions in heat #1 were better distributed throughout the casting than in heat #2. Classification of the types of inclusions recorded for each sample are summarized by the bar chart in Figure 5. This chart shows the cumulative element content for the total number of inclusions recorded.

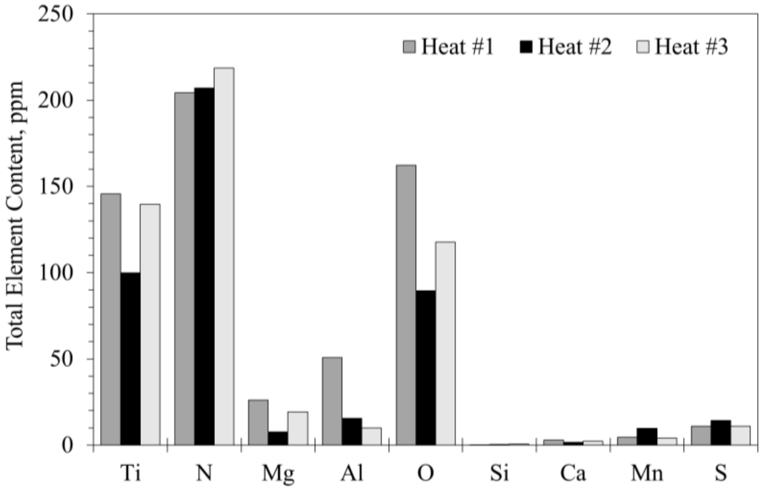

Figure 5. Cumulative element content found within all the inclusions recorded during ASPEX inclusion analysis.

The main elements found within the recorded inclusions are *Ti-N-Mg-Al-O*. Since the grain refining process made additions in steps, the elements *Mg-Al-O* are from spinel inclusions and the elements *Ti-N* are from *TiN* inclusions. This has also been verified by plotting the composition of each inclusion on to the ternary plots shown in Figure 6. These plots show that the two main types of inclusions are grouped around the *Ti*-*N* binary (*TiN*) and within the *Ti*-*Al*-*Mg* ternary (spinel). Formation of manganese sulfides contributed to trace amounts of *Mn*-*S* elements. It is possible that a small amount of metastable titanium oxide formed in the melt with dissolved oxygen that was not consumed during the formation of spinel. However, most of the titanium reacted with the dissolved nitrogen to form *TiN* as is shown in the ternary plots of Figure 6. An energy-dispersive X-ray spectroscopy (EDS) line scan of a typical inclusion with *TiN* co-precipitated on a spinel inclusion is shown in Figure 7. This type of inclusion was observed in all three experimental castings.

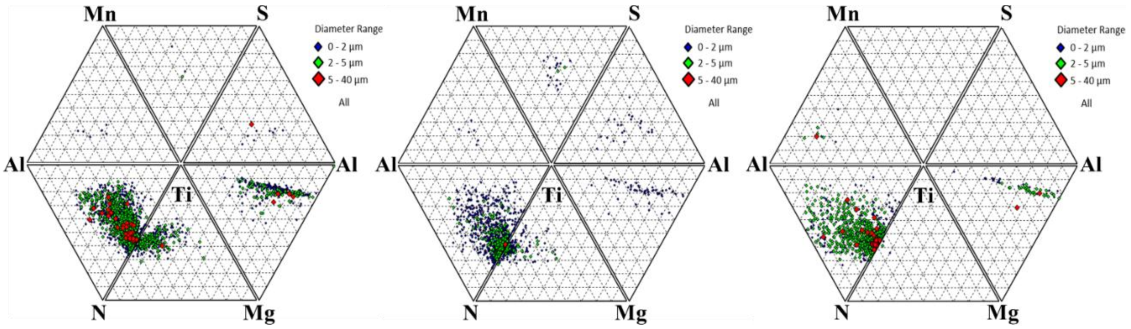

(a) (b) (c)

Figure 6. Ternary plots of inclusion composition recorded from a sample taken at the center of the casting during ASPEX inclusion analysis for (a) Heat #1, (b) Heat #2, and (c) Heat #3.

3.2. COMPARISON OF THE GRAIN STRUCTURE

Each casting was sectioned and macro-etched to reveal the extent of grain refinement. The sample is a vertical cross-section of the casting from the bottom to a height of 125 mm (5 in). Each sample was etched at room temperature in a solution of 5 parts hydrochloric acid, 2 parts hydrogen peroxide, and 3 parts distilled water. Macrostructure photos were taken optically using red and green light filters to expose grain orientations. Resulting photos of the samples are shown in Figure 8.

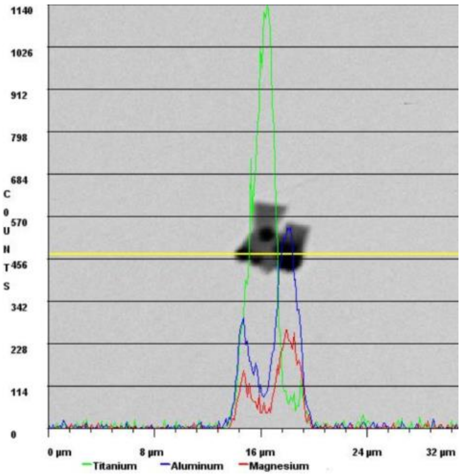

Figure 7. EDS line scan of *TiN* co-precipitated onto spinel inclusions formed in each casting of the experimental heats.

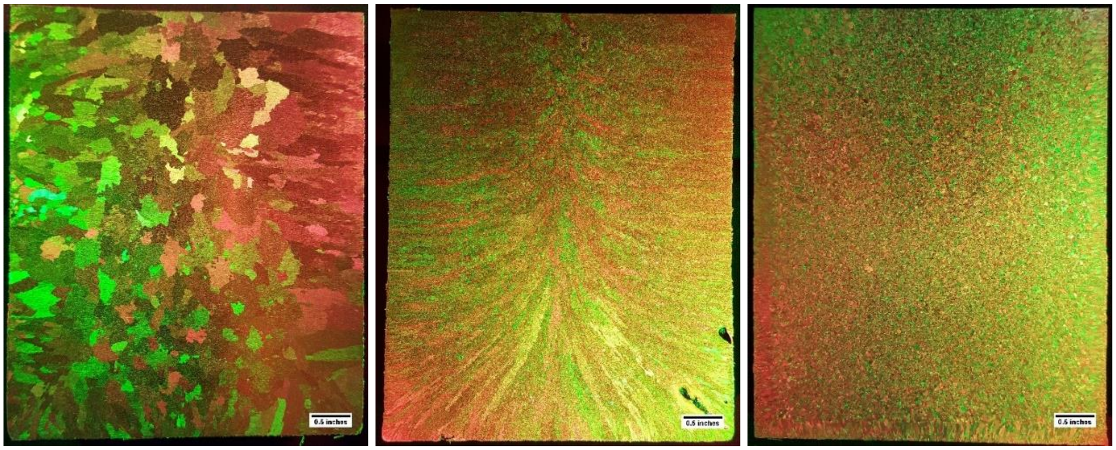

(a) (b) (c)

Figure 8. Optical image of etched macrostructure: vertical section, cast cylinder for (a) Heat #1, (b) Heat #2, and (c) Heat #3.

A grain refined macrostructure was achieved in the castings where a single-phase solidification mode was promoted in the melt (i.e. one solid phase solidifies from the liquid). A superimposed structure of columnar and equiaxed crystals persisted when dual-phase solidification mode was favored in the melt (i.e. two solid phases present with liquid). Additional optical images shown in Figure 9 were taken at the center of each casting at 15x magnification with a Dino-Lite Digital Microscope using red, green, and blue light filters. The effect of lattice disregistry of *TiN* with austenite compared to ferrite can be observed by the difference of heat #1 with coarser grains and heat #3 with finer grains. It is well known that *TiN* has a lower disregistry with ferrite phase than austenite phase making it a more effective heterogeneous nuclei during the solidification of ferritic stainless steel.[16] However, heat #2 exhibited a combination of fine, round grains surrounded by directional, columnar crystals. EBSD mapping shown in Figure 10 verified the structure in heat #2 had 0.5 to 2 mm diameter grains dispersed among larger, elongated crystals.

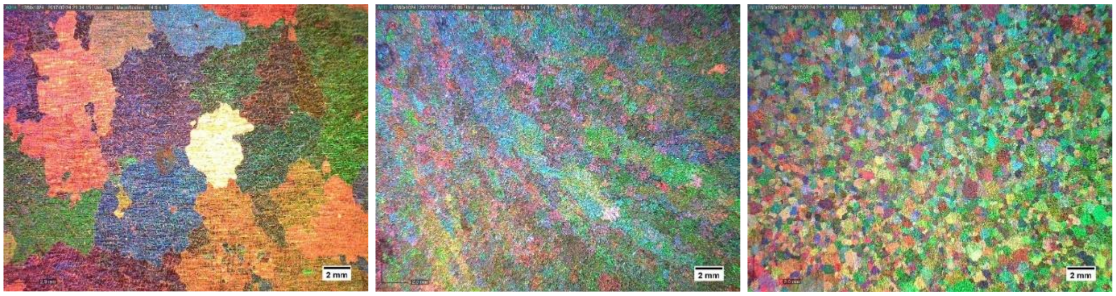

(a) (b) (c)

Figure 9. Dino-Lite image of etched macrostructure at the center of each casting
(a) Heat #1, (b) Heat #2, and (c) Heat #3.

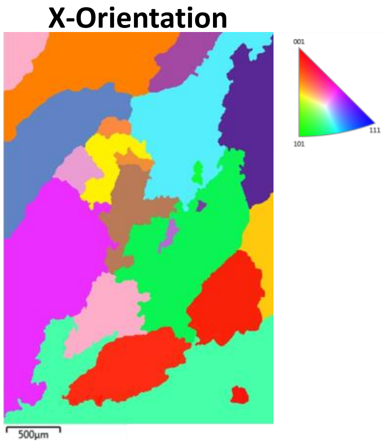

Figure 10. Localized EBSD map showing grain size in sample taken from Heat #2.

3.3. DIFFERENTIAL SCANNING CALORIMETRY

Differential Scanning Calorimetry (DSC) (TA Instruments SDT-Q600) was performed on each heat to verify the results from the solidification simulations illustrated in Figure 4. This was done to verify that heat #2 undergoes a mixed ferrite-austenite (FA) solidification mode. Small (0.1 – 0.15 g) samples were taken from each casting. DSC tests were performed in an argon atmosphere during the heating cycle from room temperature to 1500 ^{o}C and then cooled back to room temperature at a rate of 10 ^{o}C/min during the cooling cycle. The raw results obtained from the DSC test during the cooling cycle are shown in Figure 11.

This data was used for determination of transformation temperatures and latent heat. The peaks in Figure 11 represents the temperatures where a phase change is occurring and latent heat of the transformation overcomes the sensible heat. The point at which the slope of the line drastically changes upon solidification and the peak begins is the liquidus temperature. Solidus temperature is located at the tail end of the peak when the slope of the line goes from negative to approximately zero. These curves indicate that the steels from each experimental heat exhibits different solidification behaviors.

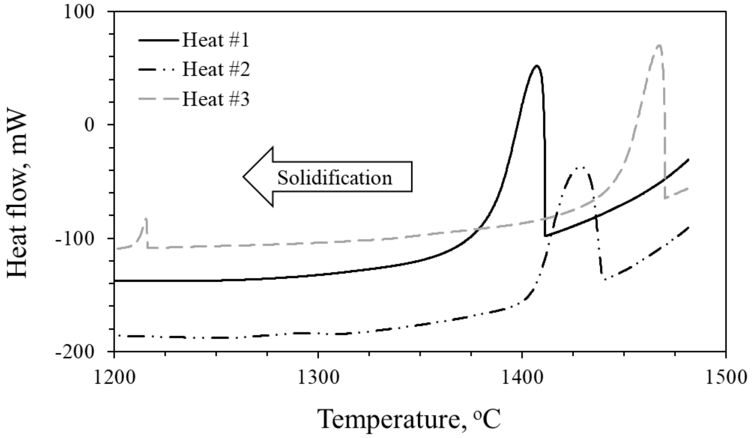

Figure 11. DSC analysis performed for experimental steels showing heat flow upon solidification.

Most notably, the liquidus and solidus temperatures of the dual-phase solidification mode heat #2 occurs in between the liquidus and solidus temperatures of the single-phase solidification mode heat #1 and heat #3. This is the same trend that was observed in the previous Thermo-Calc simulations. Shown in Table 5, the liquidus and solidus temperatures from the DSC analysis of each material are compared against the simulated values. In addition, latent heat values calculated from the DSC data were compared for each steel. Thermodynamic simulation predicted the difference in latent heat during solidification for heat #1 (L→FCC) and heat #3 (L→BCC) is approximately 30 J/g. The difference in latent heat values between heat #1 and heat #3 calculated from DSC data is 31 J/g. However, the difference in latent heat values between heat #1 and heat #2 calculated from the DSC data is 16 J/g which resulted from the mixed F→A solidification mode.

Table 5. Comparison of the liquidus and solidus temperatures determined from simulations and experimental data.

	Thermo-Calc Temperature, °C		DSC Analysis Temperature, °C	
Heat #	Liquidus	Solidus	Liquidus	Solidus
1	1420	1300	1412	1354
2	1450	1320	1440	1396
3	1500	1390	1470	1416

Both the simulated results and the DSC data suggests that heat #2 solidifies with two phases in the liquid: ferrite and austenite. It is unclear from the DSC data which is the primary phase. However, based on quenching experiments performed by Fu et al. to classify solidification mode of stainless steel by chromium and nickel equivalences, heat #2 will solidify by a mixed F→A solidification mode.[17]

4. DISCUSSION

The structure of heat #2 in Figure 9(b) is peculiar in that it appears to contain both columnar and equiaxed grains without a visible, classic CET. This type of behavior has been observed before in several weld experiments dealing with austenitic stainless steels that favor a dual-phase solidification mode of primary ferrite and secondary austenite.[18-20] In some of these steels, ferrite transformed to austenite by solid-solid reactions upon cooling. Welding experiments using austenitic stainless steel with a primary ferrite solidification mode were conducted by Villafuerte et al. to investigate similar etched grain structures.[21] In type 321 steel welds, it was found that the etched structure consisted of equiaxed primary ferrite grains dispersed randomly in a matrix of columnar austenite grains. It was concluded that titanium-rich inclusions, believed to be *TiN*, found at the center of ferrite dendrites acted as heterogeneous nuclei in the formation of equiaxed ferrite grains. The cause of the columnar austenite grains was attributed to solidification conditions (G and V) of the secondary austenite phase that may not intersect with the CET curve, thus producing only a columnar structure.[21] Another factor considered is that the low fraction of liquid remaining when the secondary austenite phase forms cannot nucleate and grow enough equiaxed austenite grains to stop the heat flow driven growth of columnar austenite grains.[21]

Another experiment by Inoue et al. investigated solidification morphologies of stainless steel welds by examining the relationship of growth direction between ferrite and austenite.[22] In the liquid pool, primary ferrite dendrites reject nickel into the liquid thus favoring austenite formation in the interdendritic regions. This austenite nucleated epitaxially from existing austenite grains outside of the melt zone and formed new austenite dendrites which grew in the interdendritic region between ferrite dendrite boundaries. This model predicts that the austenite growing in the interdendritic region is not crystallographically restricted by the growing primary ferrite phase. This implies that the austenite phase will continue to follow a preferential growth direction determined by the direction of heat flow even when the growth direction of the primary ferrite phase changes.[22] Inoue et al. referred to this growth mechanism as “Independent Two-phase Growth”. This concept was verified by casting two ingots of austenitic stainless steel containing 19 wt.% *Cr* and 11 wt.% *Ni*. The first ingot was base material while the second ingot targeted the formation of *TiN* inclusions to refine the primary ferrite phase.

Unrefined, lacy or vermicular ferrite was observed in the first casting while fine, equiaxed ferrite containing *TiN* at the center formed in the second casting. However, columnar grains of secondary austenite phase were observed in both castings making up an overall unrefined macrostructure.[22] Therefore, because of this growth independence, solidification of equiaxed ferrite grains and columnar austenite grains can occur simultaneously. Furthermore, according to the explanation given by Villafuerte et al., the solidification conditions of the secondary austenite phase will favor the growth of columnar grains as opposed to the nucleation and growth of austenite from the surfaces of *TiN* inclusions. This solidification mechanism is significantly different from the classical descriptions of peritectic and eutectic growth in two-phase alloys where prime phase crystallography is dominating. Yet, independent two-phase growth fits to the experimentally observed macrostructure in heat #2. To verify this hypothesis, the thermal conditions of phase solidification in the experimental casting were simulated.

The earliest work to thermally and chemically model the CET under realistic casting conditions was performed by J.D. Hunt.[23] In his work, the interaction of the columnar front with equiaxed grains formed by heterogeneous nuclei was examined. Using an analytical approach to study single-phase dendritic and eutectic columnar growth in an Al-Cu alloy, J.D. Hunt was able to describe a variety of variables that effect the position of the CET in the solidified alloy. These variables include growth velocity, temperature gradient, alloy composition, number of nuclei, and type of nuclei. Hunt suggested that growing columnar grains can only be stopped if a critical volume fraction of equiaxed grains exist in the melt ahead of the growing columnar front. This volume fraction was theoretically estimated to be 0.49 which corresponds to the value of the thermal gradient G in Eq. (1) required to stop columnar growth:

$$G < 0.617{N_o}^{1/3}\left\{1-\frac{(\Delta T_N)^3}{(\Delta T_C)^3}\right\}\Delta T_C \tag{1}$$

where: N_o is the heterogeneous nuclei density per unit volume, ΔT_N is the undercooling required for heterogeneous nucleation, and ΔT_C is the constitutional undercooling at the dendrite tips. Considering the thermal conditions and redistribution of alloying elements in multi-component alloys, Eq. (1) was rewritten to a form in Eq. (2), which is known as the Hunt's Criterion for CET:

$$G/V^{0.5} < 0.617{N_o}^{1/3}C_o\left\{\frac{8m(k-1)\Gamma}{D}\right\} \tag{2}$$

where: V is the dendrite tip velocity, C_o the alloy composition, m the liquidus slope, k the distribution coefficient, D the liquid diffusion coefficient, and Γ the Gibbs-Thomson parameter.

The authors estimated the values for G and V for stainless steel solidification within a mold by using computational fluid dynamics (CFD) through ANSYS 18.1 Fluent software to simulate the temperature field of the liquid metal during the solidification of the casting.[24] This same approach was used in this study. However, instead of tracking the solidification of a single solid phase, simulations were performed for the sequential solidification of two solid phases in the liquid (primary and secondary). It was assumed that solidification of the primary phase would occur up until approximately 0.5 volume fraction where the secondary phase would then appear. The results shown in Figure 12 for primary phase (red squares) and secondary phase (black triangles) at different locations from the wall towards the center of the cylindrical casting. Because latent heat upon solidification releases energy and the mold has a low thermal conductivity, heat will accumulate in the liquid metal thus causing solidification velocity of the secondary phase to be significantly lower which favors columnar growth. This graph also has two qualitative CET lines for *FCC* and *BCC* solidifying steels. These two lines have different positions because of the difference in nucleation activity of *TiN* nuclei for *FCC* and *BCC* crystals. At the same thermal conditions, heterogeneously nucleated *BCC* will favor the formation of an equiaxed structure. Assuming independent two-phase growth model, this Hunt's map explains the structure observed in heat #2. For heat #2, the primary *BCC* phase would be near the necessary amount of equiaxed grains required to stop columnar growth of the primary *BCC* phase for all points (red squares) above the intersection of the CET (*BCC*) curve. Assuming independent columnar growth of the secondary *FCC* phase, the thermal and growth conditions of the remaining liquid will not be sufficient to favor an equiaxed *FCC* structure.

It can be seen from the Hunt map that both phases experience different thermal gradient and growth velocity conditions. Since the growth of the ferrite phase does not affect the growth of the austenite phase, it is reasonable that complete grain refinement in dual-phase steels can only be achieved by stopping columnar growth of both phases. The observed superimposed or "mottled" structure in heat #2 suggests that grain refining conditions were achieved only for the primary ferrite phase. However, the secondary austenite phase path in Figure 12 suggests that a large columnar zone will be established before the conditions for equiaxed austenite growth are established. Therefore, the absence of a well-defined CET occurs and the existence of a superimposed structure of both equiaxed ferrite and columnar austenite grains prevails. This structure was observed in the macrograph for ferrite-austenite solidification mode heat #2 while a traditional CET was established in the single-phase solidification mode austenitic heat #1 and ferritic heat #3. More effective grain refinement techniques are needed to move the CET curve into an area that will favor the formation of a refined structure in steels with a mixed ferrite-austenite solidification mode.

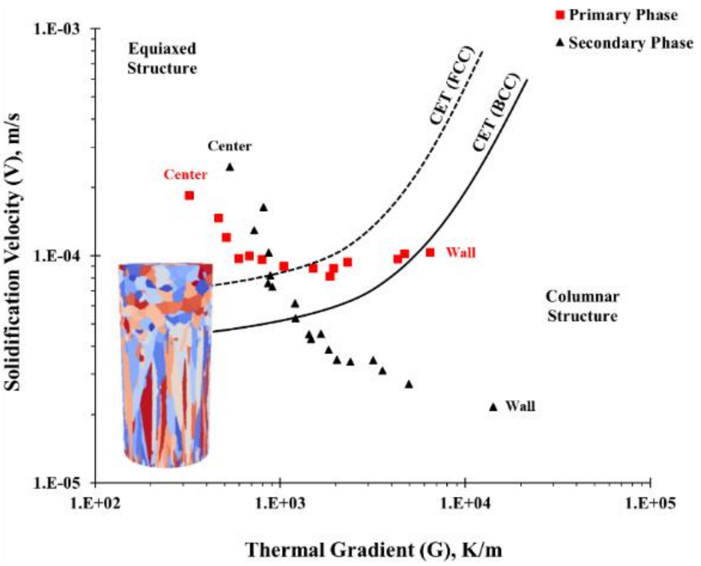

Figure 12. CFD simulated thermal and growth conditions for primary and secondary phases occurring within the mold vs. qualitative CET lines plotted based on observed CET position for FCC and BCC phases.

5. CONCLUSION

The effect on grain refining capability of heterogeneous nuclei in stainless steel was investigated for three experimental heats each targeting a different solidification sequence.

Preliminary analysis of solidification sequence using thermodynamic software indicates that austenitic heat #1 and ferritic heat #3 will solidify by single-phase solidification mode while heat #2 exhibits a dual-phase ferrite→austenite solidification mode. This analysis was validated by DSC analysis and observations reported in literature. The presence of similar nuclei in each heat was verified by ASPEX inclusion analysis. Images taken of the etched macrostructure for each casting shows that heat #1 and heat #3 achieved grain refinement while heat #2 did not. This was explained by the independence of growth between the primary ferrite and secondary austenite phases which results in more difficult thermal and growth conditions for equiaxed growth of the secondary phase. The absence of a CET and a mix of equiaxed ferrite grains and columnar austenite grains in the final structure can therefore be explained. This was validated by observing intersections on a G-V Hunt map using CFD simulated thermal gradients, *G*, and growth velocities, *V*, for each solidifying phase in the mold vs. Hunt's Criterion of a qualitative CET line plotted for both solid phases.

REFERENCES

1. X. Yin, Y. Sun, Y. Yang, X. Bai, M. Barati, and A. Mclean, "Formation of Inclusions in Ti-Stabilized 17Cr Austenitic Stainless Steel," *Metallurgical and Materials Transactions B*, Vol. 47, No. 6, December 2016, pp. 1-11.

2. J.W. Morris, Jr., "The Influence of Grain Size on the Mechanical Properties of Steel," *International Symposium on Ultrafine Grained Steels*, Fukuoka, Japan, September 2001.

3. B.S. Murty, S.A. Kori, and M. Chakraborty, "Grain refinement of aluminium and its alloys by heterogeneous nucleation and alloying," *International Materials Reviews*, Vol. 47, No. 1, July 2013, pp. 3-29.

4. D.A. Pineda and M.A. Martorano, “Columnar to equiaxed transition in directional solidification of inoculated melts,” *Acta Materialia*, Vol. 61, No. 5, March 2013, pp. 1785-1797.

5. H.B. Dong and P.D. Lee, “Simulation of the columnar-to-equiaxed transition in directionally solidified Al-Cu alloys,” *Acta Materialia*, Vol. 53, No. 3, February 2005, pp. 659-668.

6. J.F. Wallace, "Grain Refinement of Steels,” *JOM*, Vol. 15, No. 5, May 1963, pp. 372-376.

7. G.W. Form and J.F. Wallace, “Solidification of Metals: General Principals,” *Transactions of the American Foundrymen's Society*, Vol. 68, 1960, pp. 145-156.

8. G.K. Turnbull, D.M. Patton, G.W Form, and J.F. Wallace, "Grain Refinement of Steel Castings and Weld Deposits,” *Transactions of the American Foundrymen 's Society*, Vol. 69, 1961, pp. 792-804.

9. C. Wang, H. Gao, Y. Dai, J. Wang, and B. Sun, “Solidification structure refining of 409L ferritic stainless steel using Fe-Ti-N master alloy,” *Metals and Materials International*, Vol. 18, No. 1, February 2012, pp. 47-53.

10. K. Kimura, S. Fukumoto, G. Shigesato, and A. Takahashi, “Effect of Mg Addition on Equiaxed Grain Formation in Ferritic Stainless Steel,” *ISIJ International*, Vol. 53, No. 12, January 2013, pp. 2167–2175.

11. S. Lekakh, J. Ge, V. Richards, R. O’Malley, and J. Terbush, "Optimization of Melt Treatment for Austenitic Steel Grain Refinement," *Metallurgical and Materials Transactions B*, Vol. 48, No. 1, February 2017, pp. 406-419.

12. J.H. Park, “Effect of inclusions on the solidification structures of ferritic stainless steel: Computational and experimental study of inclusion evolution,” *Calphad*, Vol. 35, No. 4, December 2011, pp. 455-462.

13. Thermo-Calc thermodynamic software, Thermo-Calc Software Inc., Sweden. www.thermocalc.com/

14. S. Moon, R. Dippenaar, and S. Kim, “The peritectic phase transition of steel during the initial stages of solidification in the mold,” *AISTech Conference*, Cleveland, Ohio, May 2015.

15. D.M. Stefanescu, “Microstructure Evolution during the Solidification of Steel,” *ISIJ International*, Vol. 46, No. 6, July 2006, pp. 786-794.

16. T. Inada, “TiN Inclusion Formation during the Solidification of Stainless Steel,” *Master’s Thesis*, Massachusetts Institute of Technology, June 1999.

17. J.W. Fu, Y.S. Yang, J.J. Guo, and J.C. Ma, “Formation of two-phase coupled microstructure in AISI 304 stainless steel during directional solidification,” *Journal of Materials Research*, Vol. 24, No. 7, July 2009, pp. 2385-2390.

18. J.C. Lippold and W.F. Savage, “Solidification of Austenitic Stainless Steel Weldments-Part 1,” *Welding Journal*, Vol. 58, No. 12, December 1979, pp. 362s-374s.

19. G.L. Leone and H.W. Kerr, “The Ferrite to Austenite Transformation in Stainless Steels,” Welding Journal, Vol. 61, No. 1, January 1982, pp. 13s-21s.

20. J.C. Ma, Y.S. Yang, W.H. Tong, Y. Fang, Y. Yu, and Z.Q. Hu, “Microstructural evolution in AISI 304 stainless steel during directional solidification and subsequent solid-state transformation,” *Materials Science and Engineering A*, Vol. 444, No. 1, January 2007, pp. 64-68.

21. J.C. Villafuerte and H.W. Kerr, “Grain structures in gas tungsten-arc welds of austenitic stainless steels with ferrite primary phase,” *Metallurgical Transactions A*, Vol. 21, No. 3, March 1990, pp. 979–986.

22. H. Inoue H. and T. Koseki, “Clarification of Solidification Behaviors in Austenitic Stainless Steels Based on Welding Process,” *Nippon Steel Technical Report*, Vol. 95, No. 11, January 2007, pp. 62-70.

23. J.D. Hunt, “Steady state columnar and equiaxed growth of dendrites and eutectic,” *Materials Science and Engineering*, Vol. 65, No. 1, July 1984, pp. 75-83.

24. S. Lekakh, R. O'Malley, M. Emmendorfer, and B. Hrebec, “Control of Columnar to Equiaxed Transition in Solidification Macrostructure of Austenitic Stainless Steel Castings,” *ISIJ International*, Vol. 57, No. 5, May 2017, pp. 824-832.

II. TWO INOCULATION METHODS FOR REFINING AS-CAST GRAIN STRUCTURE IN AUSTENITIC 316L STEEL

Dustin A. Arvola, Simon N. Lekakh, Ronald J. O'Malley, Laura N. Bartlett

Missouri University of Science and Technology

Materials Science & Engineering Dept.

1400 N Bishop, Rolla, MO, U.S.A., 65409

Keywords: austenitic stainless steel, solidification, heterogeneous nucleation, titanium nitride, grain refinement

ABSTRACT

Two inoculation methods were utilized to introduce titanium nitride (*TiN*) particles into an AISI 316L steel melt to refine the as-cast grain structure during solidification. The design of the experimental melt treatments and grain refining additions was performed using thermodynamic simulations. The first inoculation method is based on *in-situ* formation of heterogeneous nuclei by *TiN* co-precipitation on preexisting *Mg-Al* spinel inclusions. This method included a two-stage melt treatment using spinel forming additions followed by an addition of titanium in the ladle just prior to pouring. The second inoculation method used a newly developed master alloy that contains *TiN* precipitates which was added in the ladle during furnace tapping. In this method, protective conditions to prevent full dissolution of the *TiN* nuclei before the onset of solidification were determined by thermodynamic simulations.

Grain refinement of the cast macrostructure was observed with both methods. The *in-situ* method provided finer equiaxed grains than the master alloy method, while a thicker zone with columnar grains next to the chill was observed. A scanning electron microscope (SEM) with automated feature analysis (AFA) was used to quantify the resulting inclusions. The master alloy method eliminated the need for spinel, gave better control of the amount and size of heterogeneous nuclei, and reduced clustering tendency in comparison to the *in-situ* method. However, the *in-situ* formed nuclei method is more effective to refine grain size. The effects of contact angle and nuclei surface geometry on the activity of heterogeneous nucleation were discussed. It is proposed that clustering *TiN* particles provides numerous sharp, concave corners which favors the heterogeneous nucleation of austenite grains. This is illustrated by SEM images of extracted *TiN* particles and electron backscatter diffraction (EBSD) analysis of grain orientation.

1. INTRODUCTION

Grain refinement is one of the few strengthening mechanisms of steel that improves both strength and toughness without the need for additional alloying elements and heat treatments which can be costly.[1] This has led to interest in producing fine-grained (from 1 μm to 5 μm) and ultrafine-grained (less than 1 μm) cast and wrought steels that can be commercially produced. Manipulation of grain size for most steels can be achieved at three different steps throughout the casting or finishing processes: (i) during solidification of the liquid metal by increasing the nucleation rate of the solid, (ii) by mechanical working, and (iii) by heat treatment of steels having polymorphic solid-state transformations, such as *FCC*→*BCC* reactions. Grain refinement by mechanical working is limited to forging for net shaped castings. Additionally, heat treatment cannot be effectively employed to promote grain refinement of single phase alloys.[2] Inoculation techniques to refine the solidification structure of austenitic stainless steel castings are crucial because significant cast structure modification of these alloys cannot be achieved by heat treatment or mechanical working of cast, near net shaped components. In steel mill operations, thermomechanical methods that include both mechanical working and heat treatment are employed to control grain size; however, as-cast grain structure is still important to control segregation and porosity. Grain refinement of the as-cast structure results in a casting that has higher strength, more isotropic properties, less segregation and porosity, better feeding, and a higher resistance to hot tearing.[3]

The technologies of grain refinement during solidification are commonly categorized into two classes: dynamic nucleation and inoculation.[4] Dynamic nucleation employs a combination of forced convection and fast cooling which promotes an increase of secondary nuclei within the melt. These nuclei are a result of dendrites that break off from the mold wall. An equiaxed structure forms by heterogeneous nucleation from these dendrite fragments. Applied forces that are known to cause grain refinement by promoting dynamic nucleation in solidifying steel are vibration[5,6], mechanical/gas stirring[7], and electromagnetic field[8-13]. Dynamic nucleation is feasible for continuous cast steel operations, which have molds that are fixed in shape and size and cast simple geometries. However, this method is difficult to apply in a commercial foundry which can have molds that vary in shape, size, and complexity.

In foundry practice, the inoculation method is more commonly used for refining grain structure. This method introduces or promotes the formation of “foreign” heterogeneous nuclei by controlled precipitation during cooling or melt additions prior to the beginning of solidification. These heterogeneous nuclei must: (i) be stable at steelmaking temperatures, (ii) be well dispersed throughout the melt, (iii) have suitable lattice registry with the primary solid phase, (iv) be readily wet by the solidifying metal (i.e. surface energy minimization), and (v) have an appropriate size and shape that promotes nucleation. A more detailed discussion of the theoretical aspects of heterogeneous nucleation activity can be found in the works of Chalmers, Flemings, and Kurz and Fisher.[14-16] Classical analysis of heterogeneous nucleation activity, between a "foreign" solid and the melt, is based on purely geometrical assumptions that are characterized by wetting angle. It predicts the lowest interfacial free energy for nucleation to occur at the interface between the foreign, solid substrate and the melt. The effectiveness of heterogeneous nucleation behavior is also linked to the similarity of the lattice parameters shared between the nuclei substrate and the nucleated solid, which is known as crystallographic disregistry. Bramfitt modified the Turnbull-Vonnegut equation to calculate planar disregistry between two phases of differing atomic arrangements.[17] Bramfitt used this equation, along with experimental results to study the effect of oxides, carbides, and nitrides on the heterogeneous nucleation behavior of liquid iron, proposing that a lattice mismatch less than 12% constitutes a potent nucleant agent. However, the authors performed *ab initio* calculations of adsorption energy for *Fe* atoms on to the surfaces of carbides and nitrides at the early stages of nucleation.[18] It was found that *Fe* adsorption on to the nuclei substrate is closely related to the number of valence electrons in the carbides and nitrides, and less dependent upon lattice parameter and surface energy of phases.

Regardless, calculating disregistry is a common technique for initial screening of potential heterogeneous nuclei. A list of the calculated lattice disregistry for a variety of compounds with austenite is provided in Table 1. All listed compounds have melting points that exceed steelmaking temperatures (>1700 °C) and lattice disregistry values that are less than 20%. Some of these compounds have not been tested experimentally but are suggested as potential nucleant agents for austenite phase based purely on the calculated lattice disregistry.

Table 1. Lattice disregistry of compound interfaces with austenite at 1600 °C.

Compound	Melting Temperature, °C	Lattice Disregistry, %	Ref
HfC	3,900	8.84	[19]
TaN	3,090	1.96	
$Si3N4$	2,715	0.45	
$CeAlO_3$	> 2,000	4.65	[20]
$Ce_{0.73}La_{0.27}O_{1.87}$	> 2,000	6.26	
$MgAl_2O_4$	2,135	9.36	[21]
TiN	2,930	7.7	[22]
TiC	3,160	16.1	[23]
NbN	2,573	18.8	
NbC	3,490	13.3	

Even though disregistry can provide a valuable initial estimate of nucleation potency, it does not fully describe the mechanisms of nucleation and growth. Other important factors that influence inoculation potency includes nuclei number density, particle geometry, solute concentration at the solid-liquid interface, and solute diffusivity.[21] The previously mentioned high temperature stability requirement limits the number of effective nuclei that are available for steel in comparison to non-ferrous castings. In addition, effective nuclei for grain refining δ-*Fe* tend to be less potent for nucleating γ-*Fe*. This implies an inherent difficulty to nucleate austenite phase in comparison to ferrite phase. In addition, the large difference in density between liquid *Fe* and many inclusions promotes the floatation of inclusions to the slag layer resulting in a rapid decrease in nuclei number density over time. These factors alone provide a considerable challenge for the development of a commercially viable grain refining melt practice for steels, especially for austenitic products.

In industry, inoculation is performed either by *in-situ* formation of nuclei with designed melt additions or by the introduction of a master alloy containing preformed nuclei. The technique of *in-situ* development has been widely explored in literature for ferritic steels but has been less studied for austenitic steels. Tyas conducted a series of inoculated austenitic stainless steel weld experiments in an attempt to achieve a grain refined structure using nuclei based on lattice disregistry and solubility calculations. The results of these experiments indicated that an equiaxed structure in the weld was achieved by inoculation with Si_3N_4, *TaN*, or *HfC* particles (in decreasing order of effectiveness).[19] Siafakas et al. examined the effects of oxides on the as-cast grain size of *Al-Ti* treated austenitic manganese steels. It was determine that increasing oxide population resulted in a decrease in grain size.[21] Initial grain size was reduced from 605 μm to 305 μm with spinel, 375 μm with olivine, and 497 μm with corundum.[21] Other non-metallic inclusions formed by melt additions that are proven experimentally to be stable, heterogeneous nuclei for the nucleation of austenite phase includes: spinel[24], *Ti*-containing inclusions[25,26], and rare earth metals (REM)-oxides and sulfides[27-29]. Suito found that *TiN* has a strong tendency to combine with *MgO* to form complex inclusions.[30] In the *Fe*-10% *Ni* alloy, the population density of *TiN*+*MgO* complexes was considerably higher than that of pure *TiN* or *TiN* coupled with any of the other oxides (Al_2O_3, ZrO_2, and Ce_2O_3). The authors applied this behavior to enhance heterogeneous nucleation and growth of *TiN* nuclei in a *Cr-Ni-Mo* austenitic stainless steel. The main mechanism includes first the formation of complex oxides followed by the accelerated co-precipitation of *TiN* onto the oxide surfaces.[22] Grain size of the as-cast structure was reduced from 2400 μm to 500 μm using this method. This principle was used in the current study of the grain refinement methods by in-situ forming *TiN* onto preexisting spinel inclusions.

The technique of master alloy addition is a popular way to grain refine aluminum alloys typically by using a *Al-Ti-B* master alloy.[31] Master alloys offer the flexibility to make the addition at any point prior to casting, thus giving better control of nuclei quantity and size. In literature, the development and application of master alloy for use in the commercial production of cast steel is still being investigated.[29] In particular, the development of REM based master alloys has yielded some positive grain refining results in austenitic and duplex stainless steel alloys. It was discovered that grain refinement of an austenitic stainless steel could be achieved by adding aluminum and powdered *Fe-Ce* master alloy to the liquid metal prior to solidification. The dominant inclusions observed were complex *Ce*-aluminates with the best grain refining effect occurring when the inclusions were around 1 μm in diameter.[25] Dahle applied a commercial grain refiner containing *Fe-Cr-Si-Ce*, known as EGR, to examine its effectiveness in super duplex stainless steel grade S4501.[32] Most of the oxides formed in the melt were *Ce* containing complexes: $(Ce,Si)O_2$ and $(Al,Ce,Si)_2O_3$. The macrostructure analysis showed a substantial decrease in the length of the columnar zone at approximately 0.07% *Ce* addition. The same *Ce*-containing master alloy was also used to refine an austenitic stainless steel grade S254 SMO. A substantial reduction in the dendrite arm spacing was achieved by promoting the formation of *Ce-Al* oxide inclusions in the steel prior to solidification.[20] Mizumoto et al. created a *Fe-Nb-C* master alloy that contains *NbC* precipitates. When the addition of master alloy was 3 wt.% in a SUS316 stainless steel melt, a fine equiaxed structure was achieved and the average grain size was reduced from 2700 μm to 200 μm.[33] Wang et al. suggested the industrial viability of *Fe-Ti-N* master alloy for grain refining 409L ferritic stainless steel. It was reported that the average equiaxed grain size decreased from 1503 μm to 303 μm, and the equiaxed grain zone expanded from 14% to 100% of the casting with an addition of 2.5 wt.% *Fe-Ti-N* master alloy.[34] Much work is still required for development of novel master alloy designs to inoculate austenitic stainless steels.

In this article, two methods of solidification-based grain refinement of cast austenitic 316L stainless steel are investigated. The first method is based on the in-situ formation of TiN by co-precipitation onto preexisting spinel inclusions in the melt. The second is based on a newly developed master alloy addition that contains preformed TiN nuclei.

2. METHODOLOGY

2.1. *IN-SITU* GRAIN REFINEMENT METHOD

The first method applied in Heat #1 is designed to target the *in-situ* formation of *TiN* precipitates in the melt as potential austenite nucleation sites. However, *Mg-Al* spinel is formed within the melt first, followed by the co-precipitation of *TiN* onto these spinel inclusions to increase efficiency of inoculation.[35] The advantages of this co-precipitation method includes initial deoxidation of the melt when forming spinel which reduces the potential to develop undesired titanium oxides. In the deoxidized melt, the growth of TiN is accelerated in the presence of spinel surfaces thus minimizing the required chemical supersaturation of Ti and N to form TiN nuclei.[22] Another advantage of this designed process is that inoculation additions can be made at low melt superheat. This could be done for minimizing clustering of the inclusions.[22] To design this complex melt treatment, thermodynamic calculations were performed using FactSage 7.0 software with FactPS and FSstel databases.[36] Base 316L steel had (wt. %): 0.02C, 0.7Si, 1Mn, 17Cr, 2Mo, 12Ni. The simulated targeted melt additions for *in-situ* method of grain refining (Heat #1) is outlined in Table 2.

Table 2. Targeted additions into 316L stainless steel melt for two inoculation methods, wt.%.

		Nuclei Formers			
Heat #: Method	Process Stage	*Mg*	*Al*	*Ti*	*N*
Heat #1: *In-situ*	Pre-treatment	0.01	0.07	-	0.084
	Inoculation	-	-	0.10	-
Heat #2: Master Alloy	Pre-treatment	-	0.02	-	0.056
	Inoculation	-	0.05	0.10	0.02

Nitrogen was added into the furnace. The first ladle additions of Mg-Al induced the formation of spinel. The second inoculation treatment with titanium addition promotes formation of TiN during melt cooling (Figure 1). Co-precipitation will occur between spinel and *TiN* because of well matching lattice parameters of these two phases.[37,38] This sequence represents the *in-situ* method used in Heat #1 in which grain refinement is activated by heterogeneous nucleation of primary austenite phase from the surfaces of *TiN* nuclei. Effective nucleation will promote growth of equiaxed primary austenite grains within the melt below liquidus temperature.

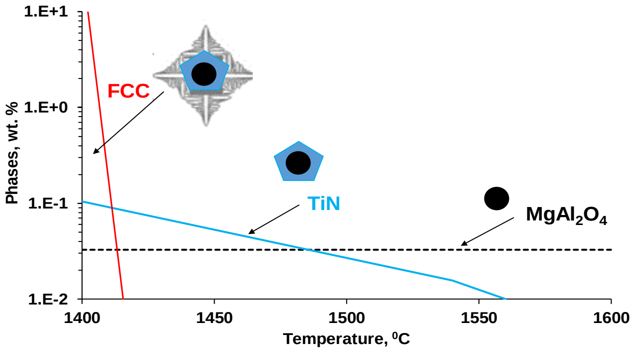

Figure 1. Heat #1: simulated *in-situ* formation of complex heterogeneous nuclei by *Mg-Al* additions into the melt, followed by *Ti* addition.

2.2. MASTER ALLOY DEVELOPMENT

The developed master alloy targeted the following design requirements: (i) a high density of preformed *TiN* particles of an optimal size and space distribution in the metal matrix and (ii) a matrix melting temperature lower that a liquidus temperature of steel that ensure rapid dispersion of the nuclei upon addition in the steel melt. Low melting temperature of the master alloy matrix is important for late stage application such as in the ladle, tundish, and/or in the mold. The master alloy must also be designed to avoid contaminating elements and harmful impurities for stainless steel. Preliminary evaluation of the master alloy design targeting these requirements was done using Thermo-Calc 2016a software with TCNI8: *Ni*-Alloys v8.0 database.[39] This master alloy had *Fe*-*Ni*-*Cr* matrix with active *Ti*-*Al*-*N* elements. The simulated precipitated phases *vs* temperature for the master alloy are shown in Figure 2(a). The formation of *TiN* in the master alloy occurs within the melt prior to matrix solidification. Predicted solidus and liquidus temperatures of the matrix were 1084°C and 1257°C respectively. The differential thermal analysis (DTA) test was performed to experimentally determine the matrix melting temperature (Figure 2(b)). The master alloy has a liquidus temperature of the matrix that is significantly less than the liquidus temperature of 316L stainless steel (1426°C) and the recorded liquidus temperature was close to the predicted.

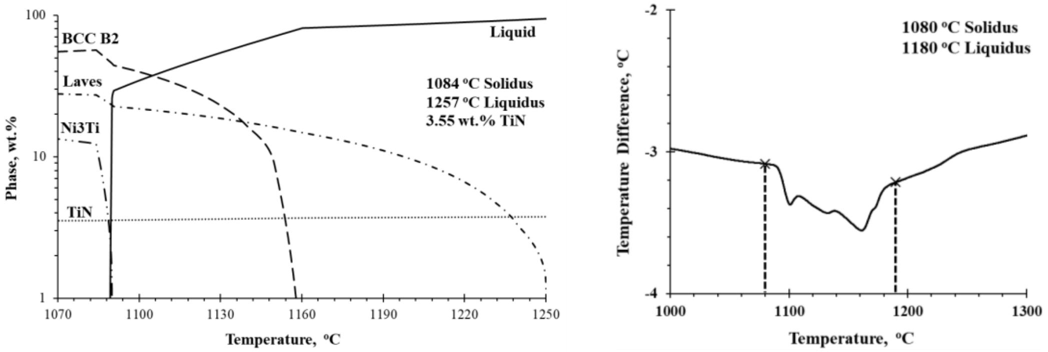

(a) (b)

Figure 2. Simulated phase formation upon equilibrium solidification and cooling of the master alloy (a) and DTA analysis indicating liquidus and solidus temperatures of the matrix of master alloy (b).

An ASPEX SEM/EDX automated inclusion analyzer was used to classify phases within the master alloy.[40] Three distinct phases were identified in the microstructure at the higher magnification seen in Figure 3(a). The element content and classification of these phases are outlined in Table 3. A high density of *TiN* inclusions was observed at lower magnification in Figure 3(b).

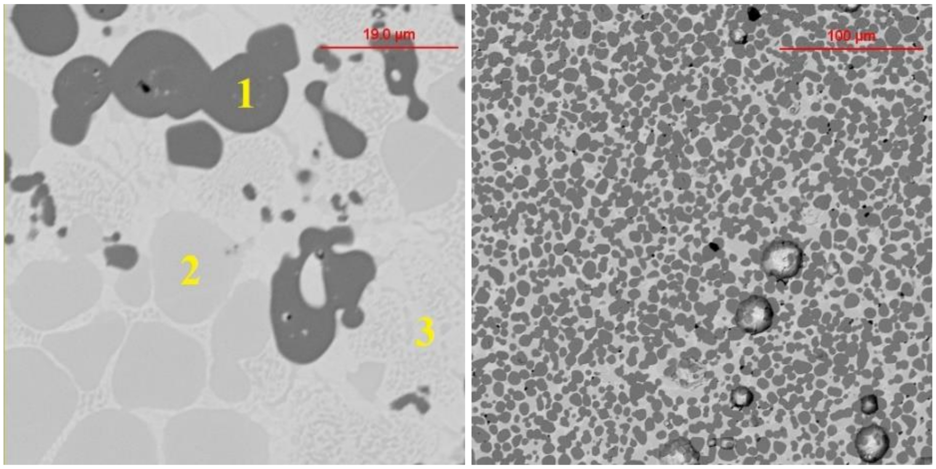

(a) (b)

Figure 3. SEM images used to identify phases (a) and observe *TiN* particle density (b).

Table 3. Phase classification and element content in master alloy microstructure shown in Figure 3(a), wt.%.

Phases	*Fe*	*Ti*	*Ni*	*Cr*	*Al*	*N*
1. Titanium nitride	0.1	55.3	0.8	0.1	0.1	43.5
2. Matrix dendrites	21.0	20.6	47.6	2.8	6.7	-
3. Matrix interdendritic	43.3	12.5	32.5	7.9	1.9	-

ASPEX SEM/EDX automated inclusion analyzer was also used to classify and measure the size of 2000 precipitates in the master alloy. The resulting ternary diagram and precipitate size distribution plot are shown in Figure 4. Most of the recorded precipitates are classified as *TiN* inclusions. The average diameter of these inclusions was around 6 μm with a large standard deviation and a positive skew in the size distribution. The percentage of the scan area that was covered by *TiN* inclusions was approximately 14%. This master alloy satisfied most of the design criteria; however, future improvements to the master alloy production process are needed to better control the size of the *TiN* particles. A diameter between 1 - 3 μm will be an optimal size.

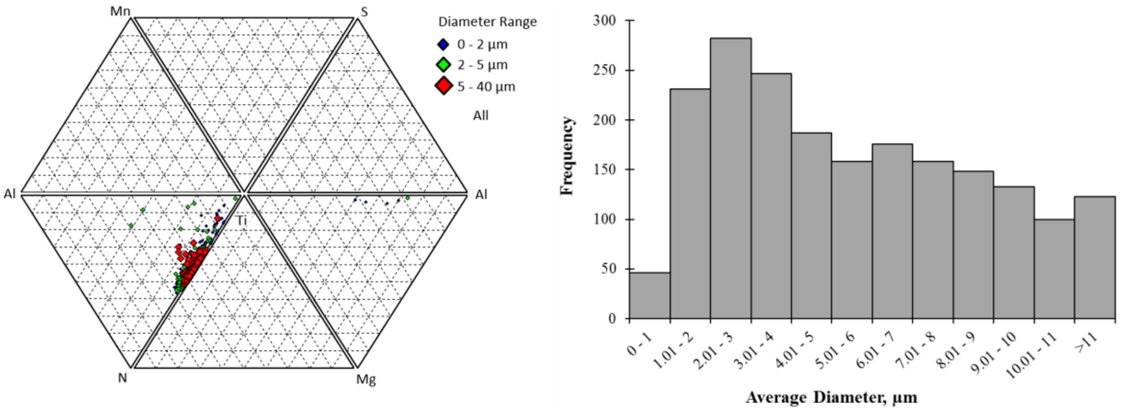

(a) (b)

Figure 4. Ternary diagram (a) and size distribution of *TiN* precipitates in master alloy (b).

2.3. MASTER ALLOY GRAIN REFINEMENT METHOD

The master alloy has pre-formed *TiN* precipitates and the goal of the designed master alloy inoculation method was to provide survivability of these precipitates in the melt until solidification started. The FactSage software was used to simulate this grain refining method which included stabilizing melt pre-treatment with *Al* and *N* in the furnace and inoculation by master alloy in the ladle (Table 2). Simulated results of *TiN* stability after an addition of master alloy in the ladle for Heat #2 is shown in Figure 5. For simplicity, alumina formed after pre-treatment is not shown on this graph. It is assumed that the melt temperature was 1550 ^oC in the ladle. Therefore, the master alloy is added at a temperature where the *Ti* and *N* contents of the melt are above the predicted *TiN* equilibrium line. This means that *TiN* is stable, and the preformed *TiN* precipitates from the master alloy will survive in the melt.

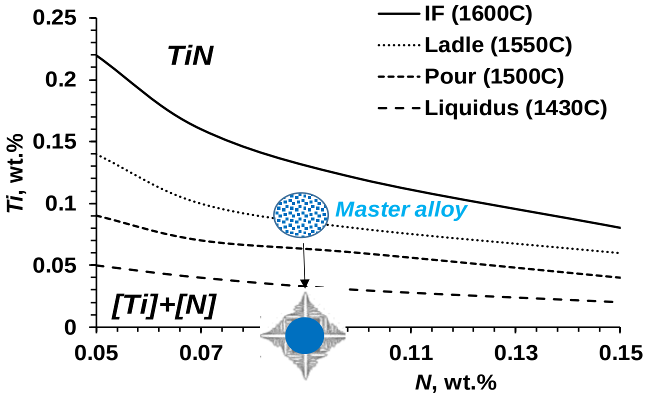

Figure 5. *TiN* stability diagram was used to predict the survivability of nuclei by introducing the master alloy into the stainless steel melt.

2.4. EXPERIMENTAL HEATS

Experimental heats were conducted in a 100 lb coreless induction furnace using the two grain refinement methods discussed previously. The base elements for these heats targeted the composition of 316L austenitic stainless steel. The charge materials used for each experimental heat consisted of specific quantities of induction iron, low carbon ferrochrome, electrolytic nickel, ferromolybdenum, electrolytic manganese, and ferrosilicon. Grain refining additions for Heat #1 included aluminum, nickel magnesium, and ferrotitanium. Grain refining additions for Heat #2 included the master alloy discussed previously. Melting was done under an argon gas cover at a flowrate of 1 scfm. Nitrogen content of the melt was adjusted using nitrided ferrochrome in the furnace just before tapping into the ladle. The heterogeneous nuclei forming elements and master alloy additions used in these heats are described in proceeding sections of this article with the corresponding chemistries listed in Table 2.

A general outline of the casting process for Heat #1 and Heat #2 is shown in Figure 6. For both heats, the charge was melted in the furnace under an argon gas cover and heated to a temperature of 1600 °C. The melt was then deoxidized with aluminum, desulphurized with calcium, and argon stirred to remove reaction products to clean the melt. The simulated results of these melt cleaning steps were not discussed in this article. Nitrided ferrochrome was then added in the furnace to increase the dissolved nitrogen content of the melt. This nitrogen is required for the *in-situ* formation of *TiN* in Heat #1 and to partially prevent dissolution of the preformed *TiN* precipitates introduced later in the ladle by master alloy in Heat #2. The melt temperature was increased in the furnace to 1640 °C and then tapped into a preheated ladle.

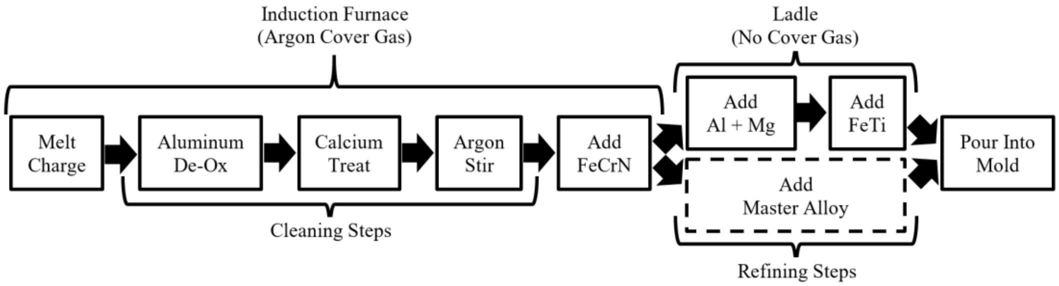

Figure 6. Designed *in-situ* (Heat #1) and master alloy (Heat #2) grain refining melt practices.

In the in-situ method (Heat #1), the ladle was transported to the pouring position where aluminum and magnesium was plunged into the melt at a temperature of 1540^{o}C and stirred vigorously, thus promoting the formation of spinel. Immediately after stirring, an addition of ferrotitanium was plunged into the melt and stirred. In Heat #2, the master alloy was plunged into the ladle during furnace tap to ensure adequate melting of the addition. Immediately after tapping, the melt was stirred vigorously and then the ladle was transported to the pouring position where it was poured into the mold at a temperature of approximately 1540 °C.

The mold design is shown in Figure 7. It is a no-bake, silica sand mold with an incorporated water-cooled, copper chilling plate at the bottom of the mold cavity that promotes a columnar structure in the solidified steel. The casting produced from this mold is a vertical cylinder with a 4” (101 mm) diameter and 8” (203 mm) height. The bottom of the vertical cylinder is designed with a rim that has a 5” (127 mm) diameter and ¼” (6 mm) height which maximizes contact area of the casting with the chill plate, thus increasing the cooling rate. An insulating riser with a 6” (152 mm) diameter and 4” (101 mm) height was incorporated at the top of the vertical cylinder to prevent shrinkage porosity within the casting. A side gating system was used to prevent additional heating of the chill plate when pouring. Thermal gradient and growth velocities of austenite corresponding to this mold design were simulated by the authors and reported elsewhere.[35] A typical unrefined macrostructure with an extended columnar zone produced by this mold design is shown in Figure 8(a).

3. EXPERIMENTAL RESULTS

The chemistry of each casting was determined using optical emission arc spectroscopy (OES) and a LECO combustion analyzer for determination of O/N and C/S as shown in Table 4. Both castings had a carbon content of 0.03 wt.%. The results conform to the composition specifications of the ASTM standard A351/A351M-16 grade CF3M, which corresponds to an AISI 316L stainless steel alloy. In Heat #1, *Mg* and *Ti* recovery was 60% and 80%, and *N* recovery was 84% in Heat #2.

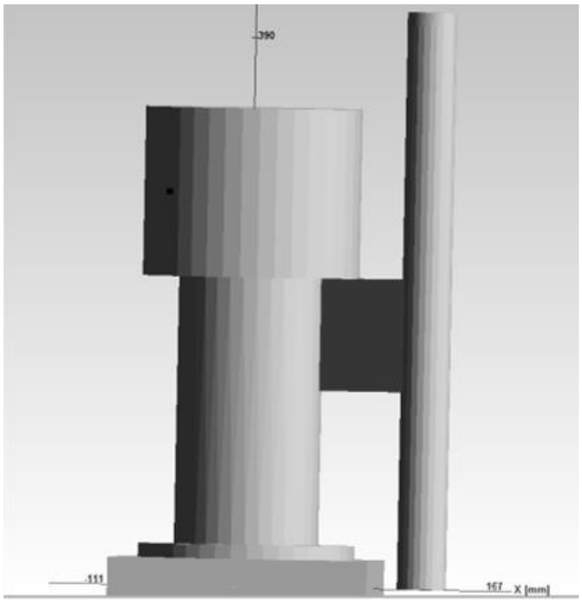

Figure 7. CAD model of casting in no-bake sand mold, with bottom *Cu*-water cooled chill.

Table 4. Casting chemistries from experimental heats, wt.%.

Heat: Method	Base Elements					Nuclei Formers			
	Si	*Mn*	*Cr*	*Mo*	*Ni*	*Mg*	*Al*	*Ti*	*N*
Heat #1: *In-situ*	0.79	0.83	16.8	1.87	11.6	0.006	0.07	0.08	0.087
Heat #2: Master Alloy	0.56	0.99	17.2	1.69	12.4	0.000	0.07	0.11	0.064

The extent of grain refinement was determined by sectioning and macro-etching each casting to reveal the macrostructure. A solution of 5 parts hydrochloric acid, 2 parts hydrogen peroxide, and 3 parts distilled water was used for etching these samples. Optical images of the macrostructure were taken using a combination of red, green, and/or blue light filters to reveal grain orientations. Each macro is a vertical cross-section through the center line of the casting from the bottom, where the chill plate is located, to a height of 5” (125 mm) from the chill plate. The macrostructure of the base casting and the experimental castings produced by the in-situ method in Heat #1 and by the master alloy method in Heat #2 are shown in Figure 8.

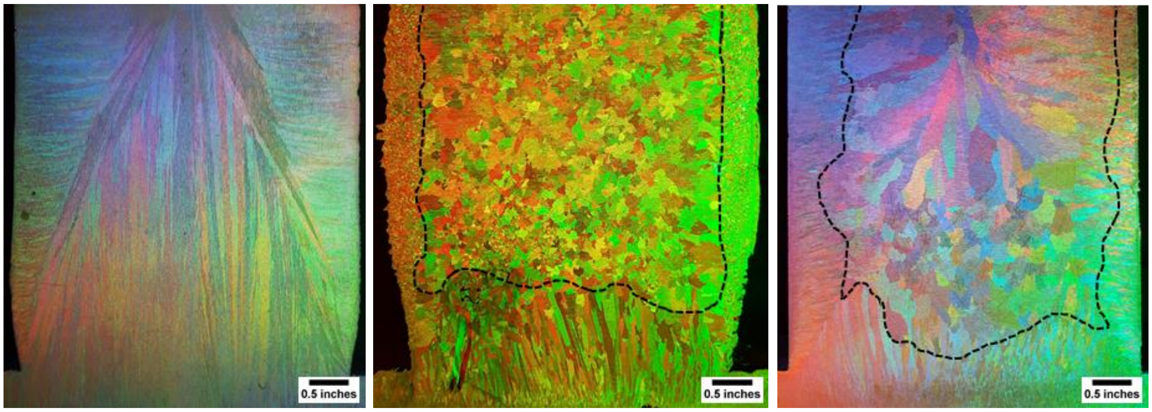

(a) (b) (c)

Figure 8. Optical image of etched macrostructure in vertical section of cast cylinder for (a) base, (b) Heat #1, and (c) Heat #2.

The macrostructure of the directionally solidified, base 316L stainless steel without any grain refining additions is shown in Figure 8(a). The structure is fully columnar with the columnar grains growing from the chill up to 5” (125 mm) into the casting. At the top casting regions, columnar dendrites growing from the sides of the mold cavity interrupted growth of vertical dendrites. Implementing the *in-situ* method for Heat #1 yields a grain refined structure shown in Figure 8(b). The length of the columnar zone from the chill plate is about 1” (25 mm) and the equiaxed grain size is relatively small. Employing the master alloy method in Heat #2 also yields the grain refined structure shown in Figure 8(c). The extent of the columnar zone from the chill plate is smaller at 0.5” (12 mm) while the equiaxed grain size is larger than observed in Heat #1. Both methods achieve refinement of the structure when compared to the base melt that used no grain refining additions.

To compare the extent of the columnar zone in both grain refined castings, the columnar-to-equiaxed transition (CET) was outlined with a dashed line in Figure 8. At different heights in the casting, the length of columnar grains growing from both walls were measured and averaged. A linear intercept method specified by the ASTM standard E112-13 was used to determine the grain size within the equiaxed zone at different heights in the casting. A grain refining factor (R) used by the authors in previous studies was employed to quantify the extent of refinement at each height (R = 0 for fully columnar structure and R = 1 for fully refined, equiaxed structure).[22] All measurements and calculated results are outlined in Table 5.

The equiaxed grain size for both methods increases with increasing distance away from the chill plate. This may be a result of insufficient dispersal of the nuclei throughout the casting because of changing cooling conditions, inclusion floatation, and/or clustering. It should be noted, that the grain refining process used in Heat #2 was much more effective at minimizing the extent of the columnar zone originating from the chill plate than Heat #1. The grain refining factor remains relatively constant for Heat #1 throughout the casting while it gradually decreases with increasing distance away from the chill plate for Heat #2.

This may indicate that the distribution of nuclei in Heat #2 is not homogeneous throughout the casting.

Table 5. Characterization of grain refinement for both castings at different distances (inch) from the chill plate.

Parameter	Heat #1: *In-situ*			Heat #2: Master Alloy		
	1 inch	3 inch	5 inch	1 inch	3 inch	5 inch
Equiaxed grain size, mm	-	2.4 ± 0.2	3.0 ± 0.1	1.9 ± 0.2	4.0 ± 0.4	6.7 ± 0.1
Columnar grain length, mm	-	11.9 ± 0.9	12.2 ± 0.4	10.4 ± 1.3	11.3 ± 0.5	16.0 ± 1.1
Grain refining factor, R	0.00	0.80	0.80	0.82	0.81	0.73

The most common type of *TiN* morphology observed in Heat #1 was *TiN* co-precipitated on to spinel cores. The line scan of this complex inclusion is shown in Figure 9(a). Also, clustering of *TiN* inclusions was observed in the middle and upper casting locations as illustrated in Figure 9(b).

A variety of *TiN* morphologies were observed in the casting from Heat #2. The first type were round, partially dissolved, mono-phase *TiN* precipitates originating from the master alloy which is shown in Figure 10(a). The second type were small, faceted, mono-phase *TiN* precipitates that had fragmented from the larger master alloy nuclei as is shown in Figure 10(b). The third type were newly developed, faceted *TiN* with alumina cores shown in Figure 10(c). Clustering of the second type occurred in a few regions in the upper casting sections as can be seen in Figure 10(d).

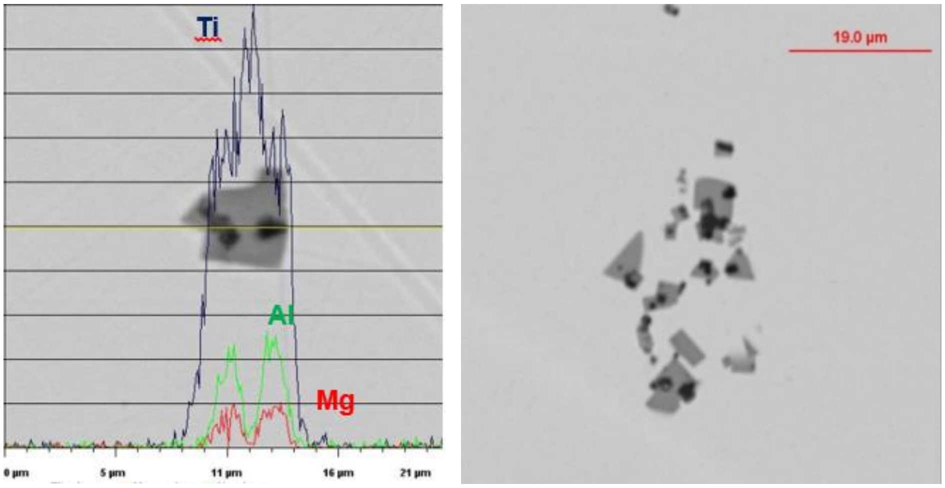

(a) (b)

Figure 9. *In-situ* method: line scan of complex *TiN* inclusions co-precipitated on *Mg-Al* spinel core (a) and inclusion clustering (b).

Inclusion analysis in Heat #2 showed that the actual process of master alloy dissolution in the melt could involve partial fragmentation, dissolution, and/or re-precipitation of *TiN* on existing alumina particles upon melt cooling as shown schematically in Figure 11.

The ternary diagrams which represented the large inclusion families at a mid-casting height of 3” (76 mm) for both refining methods are shown in Figure 12. For the Heat #1 *in-situ* method, the main inclusion classes are documented on the ternary diagram near the *Ti-N* binary line for *TiN* and within the *Ti-Mg-Al* ternary region for spinel as can be seen in Figure 12(a). There were no spinel inclusions in the Heat #2 master alloy method and the main precipitates were mono-phase *TiN* particles shown in Figure 12(b). This is significant because the master alloy method can introduce a specific type and number of nuclei into melt. It is also performed with less supersaturation of *Ti* and *N* in the melt compared to the supersaturation required for the Heat #1 *in-situ* method.

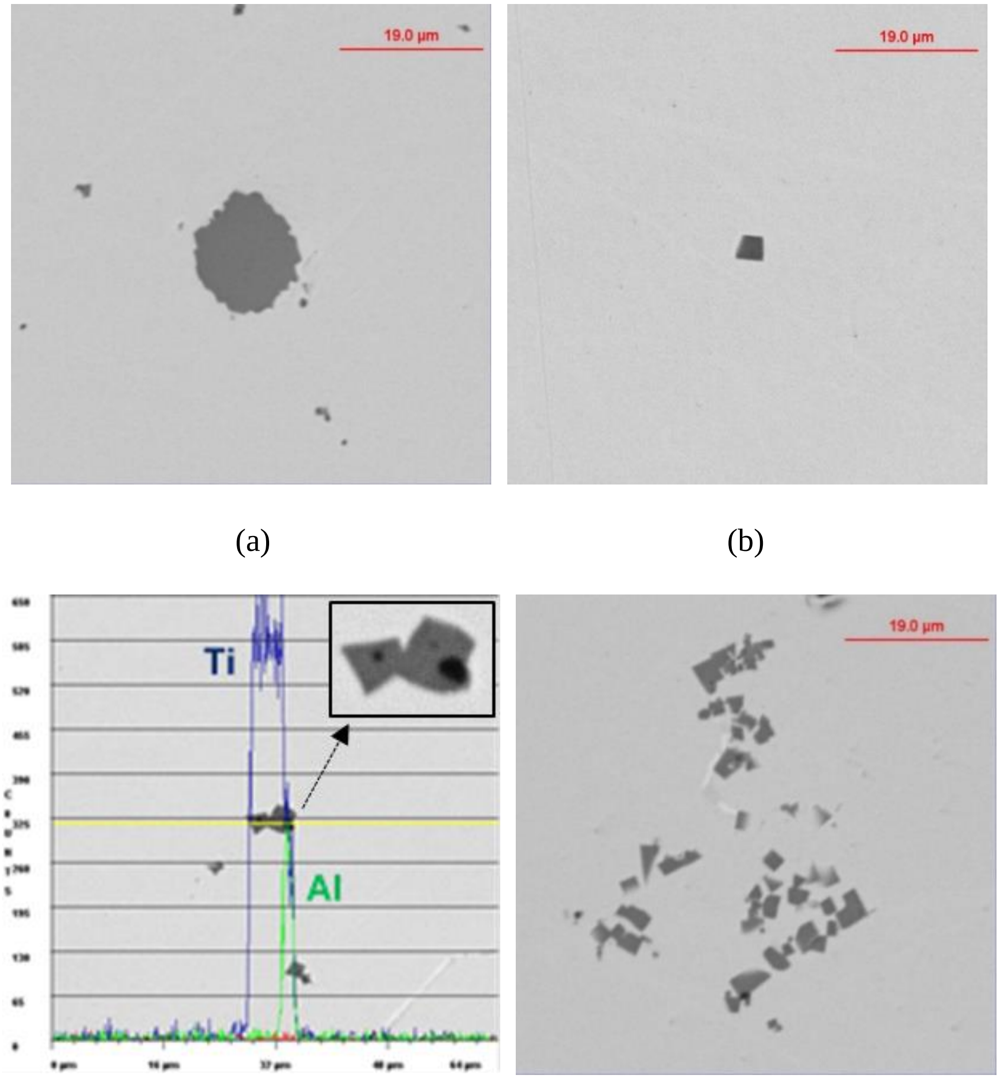

(a) (b)

(c) (d)

Figure 10. Types of inclusions observed in the casting from #Heat 2: (a) large, partially dissolved, mono-phase TiN precipitates originating from the master alloy, (b) small, faceted, dispersed mono-phase *TiN* fragments, (c) line scan of newly developed, faceted *TiN* with alumina cores, and (d) clustering of dispersed mono-phase *TiN* inclusions in the upper casting section.

The non-metallic inclusion size distribution plot is shown in Figure 13. Both heats showed near lognormal inclusion size distributions, while Heat #2 master alloy method had less variation in inclusion size. Heat #1 has a greater number of large inclusions (> 3 μm) and less small inclusions (< 3 μm) compared to Heat #2. One reason for this is that the *in-situ* method is prone to coarsening behavior in the ladle and upon solidification in the mold because of *Ti-N* supersaturation in the melt. Another reason may be related to the tendency for spinel inclusions to cluster thus resulting in larger inclusion conglomerates.

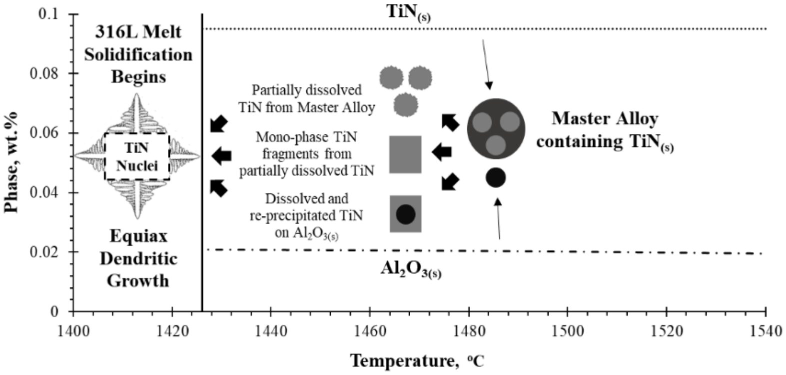

Figure 11. Possible mechanisms of heterogeneous nuclei formation in master alloy inoculated melt.

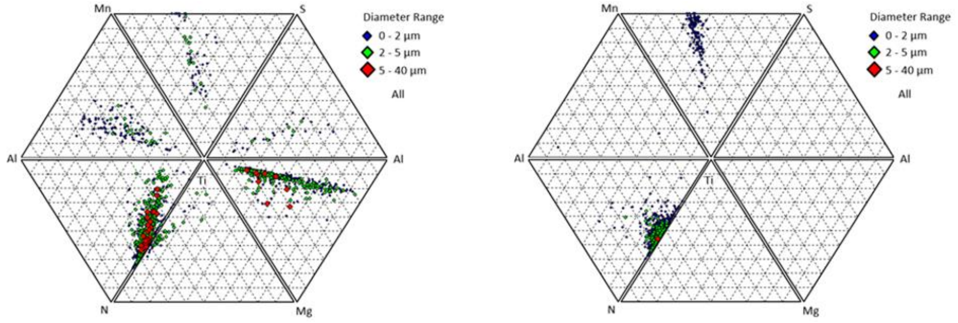

(a) (b)

Figure 12. Ternary diagrams of inclusion families in the middle section of castings produced in Heat #1 (a) and Heat #2 (b).

It is also important to note that most of the inclusions in Heat #2 have diameters that are less than 5 μm while almost half of the *TiN* nuclei in the master alloy had diameters that were greater than 5 μm (Figure 4(b)). It indicates that complicated processes take place during master alloy dissolution, including fragmentation and re-precipitation from solution on to solid alumina cores.

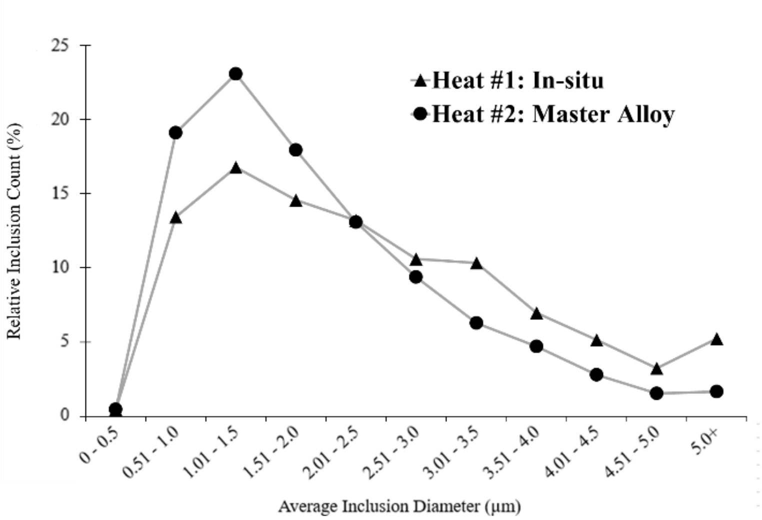

Figure 13. Comparison of inclusion sizes recorded in the castings of Heat #1 and Heat #2.

The *TiN* clustering tendency was verified using a statistical tool that compares the nearest neighboring distances (NND) of inclusions recorded during automated ASPEX analysis and the NND of a computer generated, ideal random distribution at the same area density number (*E*-ratio). The corresponding variances in experimental NND and for an ideal random distribution were also compared (*V*-ratio). This procedure was suggested to characterize the spatial distribution structure of precipitates in the casting.[41] These classifications include clustering, ordering, or random spatial distribution of precipitates and are determined by plotting the two ratios within a quadrant that predicts the 2D spatial distribution structure of inclusions. The four possible types of particle distributions are: (i) ideal random distribution ($V = 1$; $E = 1$), (ii) clustering and random ($V > 1$; $E < 1$), (iii) clusters ($V < 1$; $E < 1$), and (iv) ordered ($V < 1$; $E > 1$). The plot of experimentally measured NND for two heats at different casting heights is shown in Figure 14(a). Heat #2 exhibits an inclusion structure that is much closer to the ideal random distribution than Heat #1 at all heights throughout the casting. This may be related to the elimination of spinel as well as better control of the amount and size of nuclei in the final casting when using master alloy additions. These factors assist in the reduction of inclusion clustering. Clustering tendency of inclusions can be observed in SEM images taken from both castings at low magnification. These images are shown in Figure 14(b) for the castings of Heat #1 and Figure 14(c) for Heat #2.

4. DISCUSSION

Two solidification-based, grain refining melt practices for austenitic 316L stainless steel were designed, performed, and the resulting structures and precipitates were compared. The first method, tested in Heat #1, used *in-situ* formation of TiN nuclei by co-precipitation on pre-existing spinel inclusions in the melt. Decreasing equilibrium concentrations of dissolved Ti and N and quantity of spinel inclusions in the melt are two factors that promote the continuous nucleation and growth of TiN particles during cooling of the melt until liquidus temperature. These TiN precipitates could serve as active nucleation sites for primary austenite dendrites; however, at the same time, they have the tendency to cluster in the casting. The second method, tested in Heat #2, used a master alloy addition with preformed mono-phase TiN nuclei. These nuclei can survive in the melt in a variety of different morphologies such as dispersed mono-phase, partially dissolved, and re-precipitated with oxide cores.

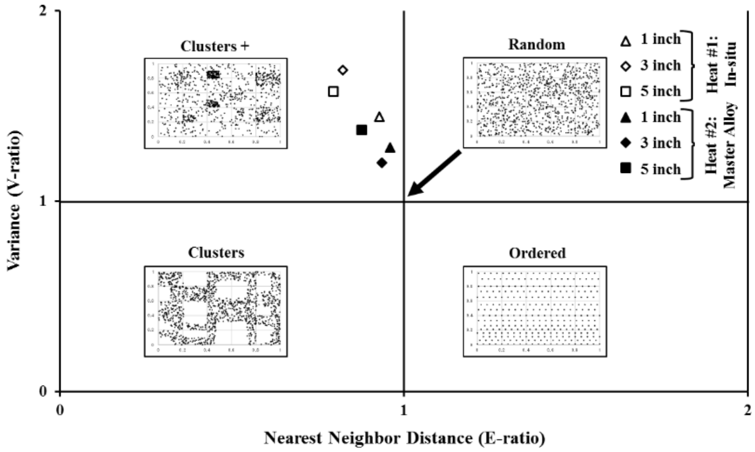

(a)

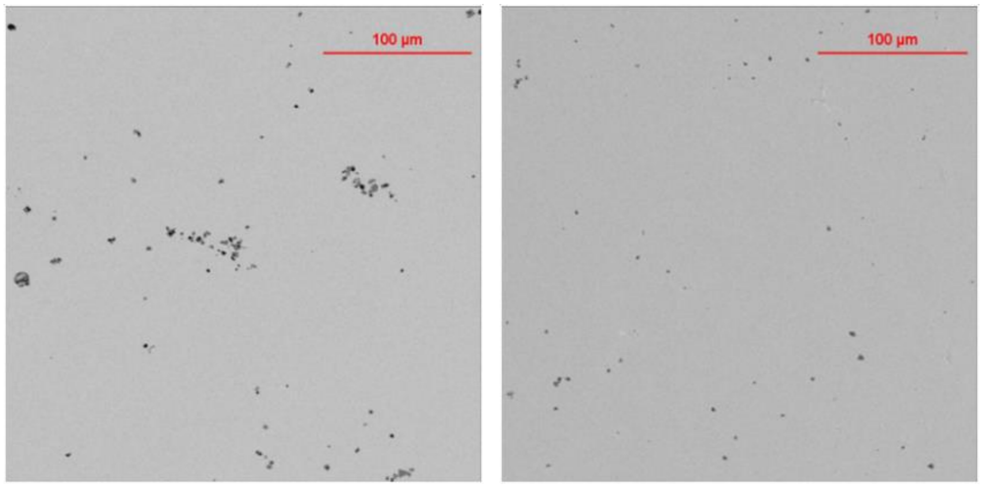

(b) (c)

Figure 14. Predicted 2D spatial distribution of inclusions at heights throughout each casting (a) and observation of clustering tendency at low SEM magnification in Heat #1 (b) and Heat #2 (c) taken from the middle section of the castings.

Both methods produced a grain refined structure but to varying extents. Heat #1 had smaller equiaxed grains but a larger columnar zone. Heat #2 had larger equiaxed grains but a smaller columnar zone. In addition, inclusion analysis of both castings revealed that Heat #1 contained mostly *TiN* with spinel cores, while Heat #2 contained mostly mono-phase *TiN* inclusions and some re-precipitated *TiN* with alumina cores. Both castings had an average inclusion diameter occurring within the desired range of 1 to 3 μm but Heat #2 had an overall smaller inclusion diameter. The inclusions in Heat #1 had a higher tendency of clustering than in Heat #2. Inclusion density remained relatively constant throughout the casting of Heat #1 while it decreased gradually with increasing distance away from the chill plate for Heat #2.

Therefore, in both heats, *TiN* dispersoids initiated heterogeneous nucleation of primary austenite dendrites but these two grain refining methods demonstrated significant differences in nucleation activity. The *TiN* nuclei efficiency in these two methods led to an analysis of the possible effects of a geometry factor. Heterogeneous nucleation is significantly affected by geometry of the substrate, including critical nuclei dimension and shape of the substrate.[42] Analysis of the shape of *TiN* precipitates in Heat #1 indicated that they had an angular, faceted geometry with some clusters having multiple intersecting boundaries with sharp angles close to 90^{o} (see Figure 9(b)). In contrast, homogeneous mono-phase *TiN* precipitates in the master alloy were spherical in shape (see Figure 4). During dissolution of the master alloy in the melt, the shape of the *TiN* nuclei changes with a variety of possible morphologies (see Figure 10) and becomes less clustered than in Heat #1.

Furthermore, a method of electrolytic extraction was utilized to observe the 3D morphology of precipitates contained within the as-cast austenitic matrix from both castings. The procedure uses 2% TEA solution (2 v/v% triethanolamine, 1 w/v% tetramethylammonium chloride, methanol) subjected to a 50 mA current. After extraction, the solution is stirred and filtered to capture the suspended inclusions. This is similar to the method used by Janis et al. to extract non-metallic inclusions and clusters from a variety of steel alloys.[43] Images of the inclusions were taken using a Hitachi S-4700 FESEM scanning electron microscope (Figure 15). A variety of straight and sharp contact angles in clustered *TiN*-spinel inclusions are observed.

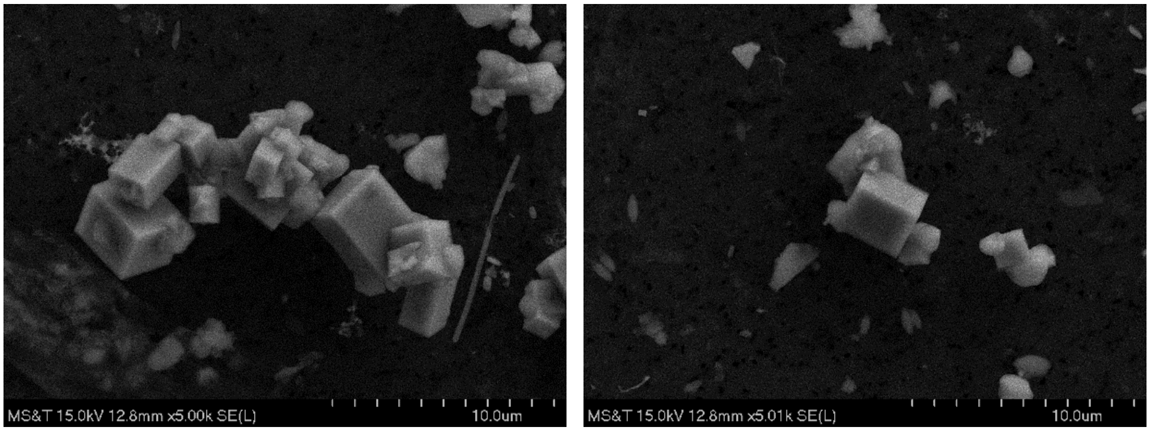

(a) (b)

Figure 15. Clustered *TiN* with spinel core inclusions extracted from casting Heat #1 (a) and faceted fragments and small clusters with alumina cores extracted from casting Heat #2 (b).

In this article, the effect of the surface topology on the activity of potential nucleation sites was analyzed by using SE-FIT software.[44] This software simulates a shape of interface geometry of an object (gas, liquid or solid) with a minimum surface energy while considering supporting surface restrictions and contact angle. Such methodology was used by Quested et al. to analyze athermal (time dependent) nucleation in aluminum alloys.[45] In this work, the relative effects of contact angle and substrate geometry were evaluated from the simulated surface curvature. Heterogeneous nucleation activity was analyzed using $f(\theta)$ function. From classical heterogeneous nucleation theory:

$$\Delta G_{heter} = \Delta G_{homo} * f(\theta) \tag{1}$$

where: ΔG_{heter} and ΔG_{homo} are the free energies of heterogeneous and homogeneous nucleation; and $f(\theta)$ is a function of contact angle, θ, and support geometry. For nucleation on a flat support without boundary restrictions, function $f(\theta)$ equals:

$$f(\theta) = 0.25(2 + \cos\theta)(1 - \cos\theta)^2 \tag{2}$$

The simulation cases were done for different contact angles and supporting, folded surface geometries which were varied by a half angle (α-Angle). These supporting surface geometries include a flat surface (90^{o} α-Angle), a 120^{o} folded surface (60^{o} α-Angle), and a 60^{o} folded surface (30^{o} α-Angle) for the same constant volume of nuclei. For a flat supporting surface without boundary restriction, simulated $f(\theta)$ for a spherical cap was similar to results of the analytical Eq. (2) (see Figure 16), thus indicating that decreasing contact angle, θ, minimizes the energy of heterogeneous nuclei formation and decreases the critical melt undercooling necessary to start nuclei growth. The simulated shape of the liquid droplet inside the 60^{o} folded surface at the same contact angle θ for both surfaces indicated that in this case the energy of heterogeneous nuclei formation will be significantly decreased when compared to a flat surface.

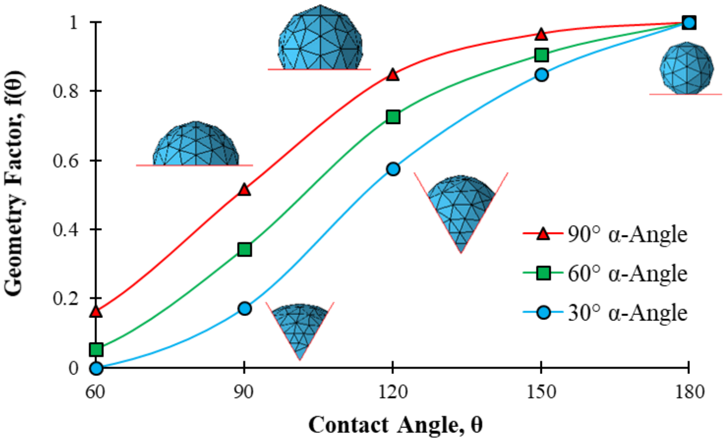

Figure 16. Joint effects of contact angle, *θ*, and nuclei surface geometry on *f(θ)* function related to decreasing free energy of heterogeneous nucleation (surface geometry with minimal energy was simulated with SE-FIT/Surface Evolver software).

Therefore, the simulation of an equilibrium nuclei surface that affects minimum energy on different types of solid surfaces showed that the nucleus geometry is an important factor of heterogeneous nucleation. The folded faceted *TiN* particle topology observed in Heat #1 has advantages when compared to globular *TiN* particles transferred from the master alloy in Heat #2. To prove the heterogeneous nucleation activity of folded *TiN* particle co-precipitated on *Mg-Al* spinel, Electron Backscattered Diffraction (EBSD) analysis was performed for a sample with fine equiaxed grains taken from the casting of Heat #1 at a 3” (76 mm) height from the chill and near the mold wall. EBSD analysis was performed at relatively low magnifications to observe the macrostructure with several grains shown in Figure 17(a), and at higher magnification to detect phase crystallographic orientation near a folded *TiN* particle seen in Figure 17 (b-d).

Some *TiN* inclusions were found on the center of larger austenite grains; however, other inclusions were found at the boundaries between smaller grains and sometimes even located on a triple junction of austenite grains as illustrated in Figure 17(a). It is typically considered that if a precipitate is located in the center of a grain it could be a heterogeneous nucleation site whereas if an inclusion is at the grain boundary it was considered to be not active during grain nucleation. However, EBSD orientation map of a folded *TiN* inclusion at the boundary of two austenite grains indicates the possibility of high nucleation activity associated with this precipitate. The lattice orientation map suggests that this inclusion nucleated two or more grains simultaneously. Two visible austenite grains, without a precipitate in the middle of each grain, are interacting with the same *TiN* nucleus. This may indicate that both grains nucleated and grew from this nucleus until the austenite grains impinged upon each other, thus creating a grain boundary which starts at the sharp corners of the nucleus. A possible nucleation sites with close orientation of austenite grains with complex nuclei are shown in Figure 17(c) by arrows. If this *TiN* inclusion was not active and was pushed to the boundary by growing austenite grains, there would be no such orientation matching.

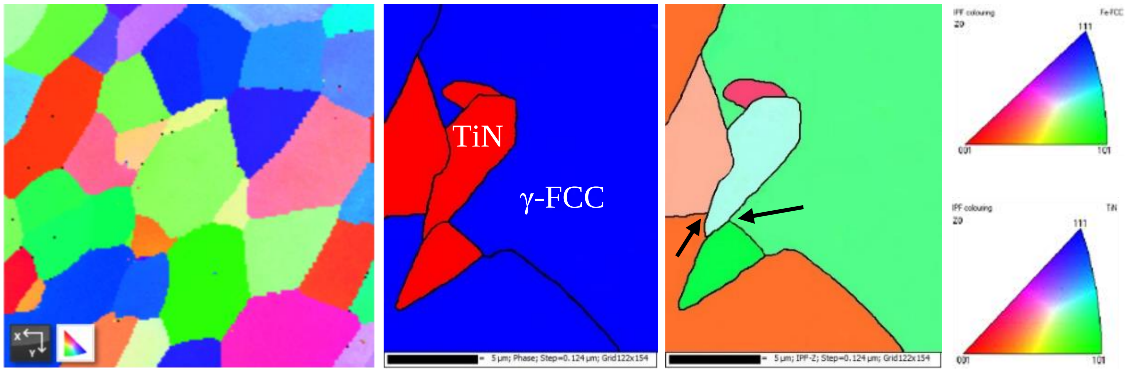

(a) (b) (c) (d)

Figure 17. Low magnification EBSD grain orientation map showing equiaxed austenite grains with *TiN* particles (black dots) (a), high magnification phase maps showing *TiN* in red and austenite in blue (b), and phase lattice orientations (c, d). The possible starting nucleation sites for two austenite grains are indicated by arrows in (c).

The experimental tests of two grain refinement methods showed that each method has advantages and disadvantages. The master alloy inoculation melting practice could provide a process that has less clustering, better control of inclusion size; however, the *in-situ* inoculation generates more active nucleation sites. Further development of the master alloy melting practice could provide a process that is safer (no volatile additions), more flexible (nuclei can be added at any location in the process) and achieves grain refinement with less inclusions (no spinel, nuclei quantity proportional to the amount of master alloy addition).

5. CONCLUSION

Two grain refining methods that introduce titanium nitride (*TiN*) particles into the melt by *in-situ* co-precipitation on to *Mg-Al* spinel and with a master alloy addition introducing preformed *TiN* particles were compared. Grain refinement of 316L alloy in a bottom chilled mold configuration was achieved with both methods. The *in-situ* inoculation method had finer equiaxed grains whereas the master alloy inoculation method had a smaller columnar zone originating from the chill plate. Analysis of inclusions in the casting revealed that spinel was eliminated, clustering tendency was reduced, and *TiN* inclusions were smaller in diameter when using master alloy additions. It was suggested that the difference in grain refining efficiency of *TiN* nuclei in both methods was attributed to the geometrical differences in inclusion morphology. Simulations of free surface of a droplet on different supporting shapes showed that the free energy of heterogeneous nucleation is lowest for a 60^{o} folded interface when compared to a flat surface. High heterogeneous nuclei activity for *TiN* clusters with sharp, folded interfaces was observed at grain boundaries during EBSD analysis of a sample taken from the *in-situ* inoculated casting.

REFERENCES

1. H. Hossam: *JMMCE*, 2014, vol. 2 (5), pp 428-69.
2. M. Maalekian: *The Effects of Alloying Elements on Steels (I)*, 2007.
3. J.F. Wallace: *JOM*, 1963, vol. 15 (5), pp. 372-76.
4. Z. Liu: *Metall. Mater. Trans. A*, 2017, vol. 48 (10), pp. 4755-76.
5. Y. Itoh, T. Okajima, and K. Tashiro: *ISIJ Int.*, 1981, vol. 21 (6), pp. 397-404.
6. A. Abugh and I.K. Kuncy: *JESR*, 2013, vol. 19 (1), pp. 7-12.
7. X.R. Chen, H. Zhong, C.J. Song, and Q.J. Jie: *Adv. Mater. Res.*, 2013, vol. 683, pp. 626-30.
8. H. Takeuchi et al.: *ISIJ Int.*, 1981, vol. 21 (2), pp. 109-116.
9. Y. Itoh, T. Okajima, H. Maede, and K. Tashiro: *ISIJ Int.*, 1982, vol. 22 (3), pp. 223-29.
10. X.Q. Wu et al.: *JMEP*, 1999, vol. 8 (5), pp. 525-30.
11. S. Zhou, H. Li, and J. Rao: *China Foundry*, 2007, vol. 4 (3), pp. 198-201.
12. S. Zhou et al.: *J. Cent. S. Univer. Tech.*, 2009, vol. 16 (3), pp. 360-64.
13. Y. Xu, E. Wang, Z. Li, and A Deng: *J. Iron Steel Res. Int.*, 2017, vol. 24 (5), pp. 483-89.
14. B. Chalmers: Principles of Solid., *Wiley*, 1964, pp. 62-90.
15. M. Flemings: Solid. Processing, *McGraw-Hill*, 1974, pp. 290-327.
16. W. Kurz, D. Fisher: Fund. of Solid., *Trans. Tech. Publications*, 1986, pp. 21-45.
17. B. Bramfitt: *Metall. Trans.*, 1970, vol. 1 (7), pp. 1987-95.
18. S.N. Lekakh, N.I. Medvedeva: *Comput. Mater. Sci.*, 2015, vol. 106, pp. 149-54.

19. N. Tyas: *A Dissertation at the University of Cambridge*, 2000.

20. C. Van der Eijk and J. Walmsley: *ISS Electric Furnace Conf.*, 2001, pp. 51-60.

21. D. Siafakas et al.: *Metals*, 2017, vol. 7 (6), ID 186.

22. S.N. Lekakh et al.: *Metall. Mater. Trans. B*, 2017, vol. 48 (1), pp. 406-19.

23. T. Inada: *A Master's Thesis at Massachusetts Institute of Technology*, 1999.

24. D. Siafakas: *Thesis at Jönköping University*, 2017.

25. M. Andersson et al.: *European Commission*, 2011.

26. R. Tuttle: *Office of Naval Research*, 2009.

27. F. Pan et al.: *Materials*, 2016, vol. 9 (6), pp. 1-19.

28. R. Tuttle: *Office of Naval Research*, 2010.

29. C. Van der Eijk et al.: *ISIJ Int.*, 2009, vol. 49 (7), pp. 1046-50.

30. H. Suito: *ISIJ Int.*, 2001, vol. 41 (7), pp. 748-56.

31. A.L. Greer: *Phil. Trans. R. Soc. Lond. A*, 2003, vol. 361, pp. 479-95.

32. E.S. Dahle: *A Master Thesis at the Norwegian University of Science and Technology*, 2011.

33. M. Mizumoto, S. Sasaki, T. Ohgai, and A. Kagawa*: Int. J. Cast Met. Res.*, 2008, vol. 21 (1-4), pp. 49-55.

34. C. Wang et al.: *Metall. Mater. Trans. A*, 2010, Vol. 41 (7), pp. 1616-20.

35. S.N. Lekakh, R. O'Malley, M. Emmendorfer, and B. Hrebec: *ISIJ Int.*, 2017, vol. 57 (5), pp. 824-32.

36. Factsage 7.0 software, *GTT-Technologies*, Aachen. www.gtt-technologies.de.

37. D. Kruger and A. Garbers-Craig: *Metall. Mater. Trans. B*, 2017, vol. 48 (3), pp. 1514-32.

38. X. Yin et al.: *Metall. Mater. Trans. B*, 2016, vol. 47 (6), pp. 3274-84.

39. Thermo-Calc 2016a software, *Thermo-Calc Software Inc.*, Sweden. www.thermocalc.com.

40. M. Harris et al.: *AISTech Proceedings*, 2015, pp. 3315-25.

41. S.N. Lekakh: *IJMC*, 2017, vol. 11 (4), pp. 743-48.

42. M. Qian: *Acta Mater.*, 2007, vol. 55 (3), pp. 943-53.

43. D. Janis, R. Inoue, A. Karasev, and P. Jönsson: *Adv. Mater. Sci. Engr.*, 2014, vol. 5 (2), pp. 1-7.

44. SE-FIT Software, *Portland State University*, www.se-fit.com.

45. T.E. Quested and A.L. Greer: *Acta Mater.*, 2005, vol. 53 (9), pp. 2683-92.

III. EFFECT OF GRAIN REFINING ON PROPERTIES OF SUPERAUSTENITIC STAINLESS STEEL

Dustin A. Arvola, Mark C. Emmendorfer, Ronald J. O'Malley,

Simon N. Lekakh, Laura N. Bartlett

Missouri University of Science and Technology

Materials Science & Engineering Dept.

1400 N Bishop, Rolla, MO, U.S.A., 65409

Keywords: superaustenitic stainless steel, grain refinement, segregation, mechanical properties, machinability, corrosion resistance

ABSTRACT

A grain refined structure in high alloy *19Cr-17Ni-6Mo* superaustenitic stainless steel was achieved by applying melt inoculation treatments. This caused the in-situ formation of titanium nitrides (*TiN*) on to preexisting spinel ($MgAl_2O_4$) inclusions thus promoting heterogeneous nucleation of the austenite during solidification. Both a base and grain refined alloy were cast under laboratory conditions into a sand mold producing a heavy section, 100 lb cylindrical casting. These castings were subjected to a typical homogenization heat treatment used in industry for superaustenitic steel; however, no coarsening or additional refining of the as-cast grain structure were observed in either the base or grain refined steels. An automated ASPEX SEM/EDX analysis was used to analyze non-metallic inclusions and interdendritic *Cr*, *Ni*, and *Mo* segregation. It was found that the grain refined structure was more effective at reducing interdendritic segregation after heat treatment than the base steel. The experimentally measured segregations were compared to thermodynamically simulated.

The properties of an unmodified base and inoculated steels were examined in this work. Tensile testing of both scenarios in the heat-treated condition revealed improvements in ultimate tensile strength, ductility, and yield strength for the refined material. The room temperature impact properties experienced a slight decrease in the average value of impact strength, but showed improved stability compared to the base steel. Fixed volume machining tests were conducted for material in the base and inoculated condition. The machining results showed that the inoculated steel has a slightly improved machinability. This is due to the finer grain size of the modified steel which offsets the higher volume fraction of non-metallic inclusions. Corrosion testing was performed at an elevated temperature (ASTM A262-15 Practice B) and at room temperature (ASTM G48-11 Method A) to determine corrosion rate and pitting characteristics. The inoculated alloy compared to the base alloy exhibited a decrease in corrosion rate, but an increase in mass loss due to pitting. Characterization of base *vs* inoculated high alloy superaustenitic stainless steel reveals the merits of using an inoculation method during the steelmaking process to improve the properties of cast products.

1. INTRODUCTION

It is widely accepted that both the microstructure (internal structure) and macrostructure (grain structure) strongly influence many of the macroscopic properties of steels. Grain boundary strengthening, described by the Hall-Petch relationship, has proven to be an effective and often cheap method for improving the mechanical properties. The concept of reducing the average grain size in the microstructure has driven many modern innovations in electromagnetic stirring (EMS), heat treatments, and rolling/working processes. The capability to commercially produce fine-grained (from 1 μm to 5 μm) and ultrafine-grained (less than 1 μm) steels has become common practice in steel mill operations. These grain refining methods, however, are not viable options in foundry practice for austenitic stainless steels. Mechanical working is often limited to forging for net shaped castings, and grain refinement by heat treatment cannot be effectively employed for single phase alloys. Therefore, solidification-based inoculation practices provide the best alternative for refining the as-cast structure of austenitic stainless steels.

However, few inoculants exist for steelmaking applications partly because of the high temperature stability necessary for the nucleant to survive within the melt. The inherent difficulty to nucleate austenite further limits the number of available inoculants for austenitic stainless steel. Some of the non-metallic inclusions that have been proven experimentally to be stable, heterogeneous nuclei for the nucleation of austenite phase includes: spinel[1], Ti-containing inclusions[2,3], and rare earth metals (REM)-oxides and sulfides[4-6]. Recent work by the authors has implemented the *in-situ* formation of titanium nitrides (TiN) on to preexisting spinel ($MgAl_2O_4$) inclusions to grain refine high alloy *Cr-Ni-Mo* superaustenitic stainless steels.[7] The structure was refined from an average grain size of 2400 μm to 500 μm. The same grain refining melt practice was adopted for the alloy in this study.

Superaustenitic stainless steels are often categorized as having alloying elements (particularly nickel, copper, nitrogen, and/or molybdenum) that are higher than the conventional 300-series stainless steels. These stainless steels are fully austenitic in the as-cast form. The additional nickel content increases the resistance to reducing environments, and the additional molybdenum, copper, and nitrogen improves the resistance to pitting corrosion in chlorides.[8] Therefore, these alloys are highly resistant to corrosion in high-temperature applications, chloride-containing environments, and a number of other acidic mediums. These alloys are superior in applications where other stainless steels would fail by pitting or stress corrosion cracking.[8] The selected superaustenitic stainless steel for this study is similar in composition to the high *Mo* ACI-ASTM CK3MCuN alloy. John DuPont et al. spent nearly a decade optimizing heat treatments to improve the corrosion resistance of as-cast CK3MCuN alloy. Microstructural characterization of this alloy in the as-cast form exhibits primary γ-austenite dendrites with brittle, *Mo*-rich σ-phase forming in the interdendritic regions due to segregation during solidification.[9] This segregation causes the dendrite cores to be depleted of *Mo* (susceptible to corrosive attack), and the interdendritic regions are weakened by σ-phase (decrease in mechanical properties).[9] A post-casting heat treatment can be employed to homogenize the *Mo* throughout the matrix and dissolve the interdendritic σ-phase. It was found that near-complete homogenization and dissolution of the as-cast alloy could be achieved with a heat treatment of 1205 ^{o}C (2201 ^{o}F) for four hours corresponding to an improvement in the corrosion resistance.[9]

A relationship between the grain size and corrosion rate of stainless steel has yet to be determined. However, it has been postulated by numerous authors that corrosion rate is directly proportional to the grain size for metals that demonstrate some level of passivity like stainless steels.[10] Corrosion resistance is also dependent on other factors. Li et al. investigated the effect of temperature on the corrosion behavior of superaustenitic stainless steel submerged in phosphoric acid solution. It was determined that increasing the operating temperature contributed to a degradation in the corrosion resistance of the alloy in particular by the increased dissolution of MnS inclusions in the matrix.[11] Therefore, inclusion type and quantity can also effect the corrosion characteristics of stainless steel alloys. Grain size can also affect the mechanical properties of the alloy. The Hall-Petch relation is shown in Eq. (1):

$$\sigma_y = \sigma_o + k_{HP}/\sqrt{d} \tag{1}$$

where: σ_y is the yield strength, σ_o the bulk stress, k_{HP} a material constant, and d the grain size. This general equation demonstrates that the strength of a variety of metals is inversely proportional to grain size. Yuan Li et al. conducted a review of the Hall-Petch relation using experimental datasets collected by other authors for a variety of metals. It was concluded that the datasets for iron and steel are well-fitted to the Hall-Petch equation.[12] In particular, AISI 316L and 301 austenitic stainless steels exhibit the same behavior of increased strength with decreasing grain size.[12] Huabing Li et al. performed a study of the microstructure evolution and mechanical properties of friction stir welding superaustenitic stainless steel. It was found that reducing the average grain size of the base metal from 62.7 μm to 1.3 μm in the stir zone led to improvements in tensile strength (+20 MPa), yield strength (+65 MPa), and hardness (+87.3 Hv).[13] A reduction in the elongation was also noted (-28%) despite the traditional fine grain strengthening theory that suggests grain refinement simultaneously increases the tensile strength, yield strength, hardness, toughness, and ductility of most metals.[13] The dependence of strength, elongation, and toughness *vs* grain size was also investigated for metallic structural materials. It was observed that decreasing grain size resulted in an increase in yield strength (Hall-Petch relation), decrease in elongation (inversely proportional), and an initial increase then decrease in toughness (parabolic function).[14]

In addition to the verification of the effect of grain refinement on mechanical properties and corrosion resistance, the possible changes in machinability were also evaluated. The definition of machinability is the ease of a material to be machined. This can be evaluated by several parameters: tool life, tool forces, surface roughness of the workpiece, and chip formation.[15] The tool life criterion is one of the more common practices of defining the machinability of a material.[16] Superaustenitic stainless steel is known to be very difficult to machine. This is because of the high alloying content namely *Cr*, *Ni*, and *Mo* which are added for better corrosion resistance and mechanical properties.[17] Problems associated with machining this kind of stainless steel include: excessive tool wear in the forms of flank wear, notch wear, crater wear, edge chipping, and built-up edge.[17-19] It is more common to find research on the machinability of 304 and 316 austenitic stainless steel; however, there is little research done on the machinability of superaustenitic stainless steel. Previous research has investigated the effect of grain size on the machinability of 304 stainless steel. Komatsu et al. studied the effect of grain size during micro-milling.[20] They found that when the grain size was decreased from 9 μm to 1.5 μm the surface finish was significantly improved by reduction of burr formation during machining. Jiang et al. studied the effect of grain size on the tool life during machining of 304L.[21] They varied the grain size by varying the holding temperature after hot-working to promote grain growth. Tool wear increased as grain size increased. Many researchers studied the effect of abrasive inclusions on machinability of different steels.[22-26] Their findings agree that tool life is decreased when machining a steel with a higher volume fraction of inclusions compared to machining a cleaner steel. No research was found that investigated the combined effects of grain size reduction and the presence of abrasive inclusions on machinability of a steel.

In this article, the effect of grain refinement on the properties of an inoculated superaustenitic stainless steel alloy will be investigated. The casting process, heat treatment, structure characterization, segregation behavior, and inclusion analysis will be explained. The properties of interest include mechanical properties, machinability, and corrosion resistance.

2. EXPERIMENTAL SET-UP

2.1. CAST STEELS AND SAMPLING

Two pairs of experimental heats were conducted in a 100 lb coreless induction furnace, and details of inoculation treatment for grain refinement were described elsewhere.[7] The charge material used in all heats were ingots possessing the desired base composition of the targeted superaustenitic stainless steel alloy. These ingots were melted under an argon cover. A set of two unmodified (base) heats underwent a deoxidizing treatment by adding aluminum and calcium wire to the tap stream during furnace tap into the ladle. The furnace was tapped at a temperature of 1640 ^{o}C. The melt was then poured at a temperature of 1500 ^{o}C into a no-bake, silica sand mold shown in Figure 1(a) thus producing a cylindrical casting with a 100 mm diameter. The melt treatment in Figure 1(b) indicates the steps of the casting process in the pair of inoculated heats which targeted grain refinement. The melt was deoxidized with aluminum, calcium treated, and argon stirred.

Nitrogen content of the melt was adjusted by an addition of nitrided ferrochrome in the furnace just before tapping into the ladle at a temperature of 1640 ^oC. Nuclei forming additions of *Mg-Al-Ti* were made in the ladle just prior to pouring into the mold at 1500 ^oC. One casting from each set (base and refined) was used to study microstructure and mechanical properties while the remaining two castings from each set were used for the machinability tests

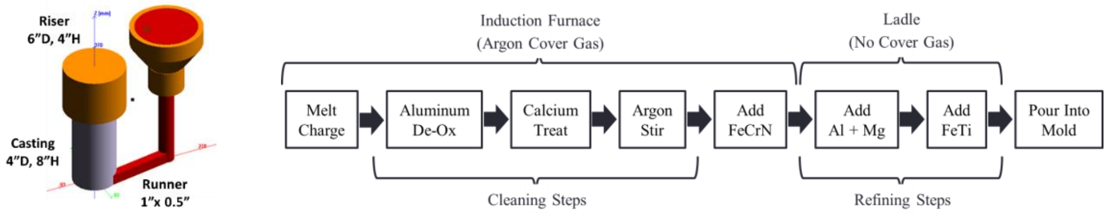

(a) (b)

Figure 1. Mold design (a) and a layout of the grain refining melt treatment (b) used in this study.

An outline of the composition achieved in both heats are outlined in Table 1. Both heats had a carbon content of 0.03 wt.%. These values were collected by spectrometer and LECO combustion analyzer. The biggest difference in heat design can be observed in the quantity of nuclei forming elements *Mg-Al-Ti-N*.

Table 1. Chemistries of experimental heats, wt.%.

Heat	Base Elements						Nuclei Formers			
	Si	*Mn*	*Cr*	*Mo*	*Ni*	*Cu*	*Mg*	*Al*	*Ti*	*N*
Base	0.63	0.54	19.2	6.08	17.1	0.64	0.000	0.01	0.00	0.093
Refined	0.78	0.54	18.9	5.92	17.4	0.65	0.009	0.08	0.07	0.091

Heat treatment of the casted alloy was performed to eliminate segregation, σ-phase, and any other secondary phases. The heat treatment procedure is outlined in ASTM standard A744/A744M-13 for CK3MCuN alloy. It is specified that the alloy be heated from room temperature to a minimum temperature of 1200^{o}C (2200^{o}F), held at this temperature for a minimum of 4 hours, and quenched in water back to room temperature. This procedure was modified to include intermediate soaking temperatures to ensure equilibrated conditions of the casting at the desired heat treatment temperature.

A variety of samples were taken from the first casting of each set. Locations in the casting where samples were taken are shown in Figure 2 and have been coded for test identification. Figure 2(a) shows a transverse section taken at a height of 5" in the casting which is near the location labeled 'Top of Mold' in Figure 2(b). Figure 2(b) is a longitudinal, cross-section of the casting that is about 4" tall. Sample dimensions are dictated by the test being performed and will be discussed in proceeding sections of this article. The second casting from each set was used for the machinability study.

Outlined in Table 2 are the tests that correspond to each sample illustrated in Figure 2. These tests include pitting corrosion, intergranular corrosion, segregation study, inclusion analysis, tensile testing, and impact testing. The details of these tests and the machinability trials of the recast material will be discussed in proceeding sections of this article. Tests that correspond to each sample are marked with a 'X' and the segregation study indicates which samples are in as-cast and heat-treated forms.

2.2. STRUCTURE CHARACTERIZATION

The grain structure before heat treatment was determined by sectioning and macro-etching each casting to reveal the macrostructure. A solution of 5 parts hydrochloric acid, 2 parts hydrogen peroxide, and 3 parts distilled water was used for etching these samples. Optical images of the macrostructure were taken using a combination of red, green, and/or blue light filters to reveal grain orientations.

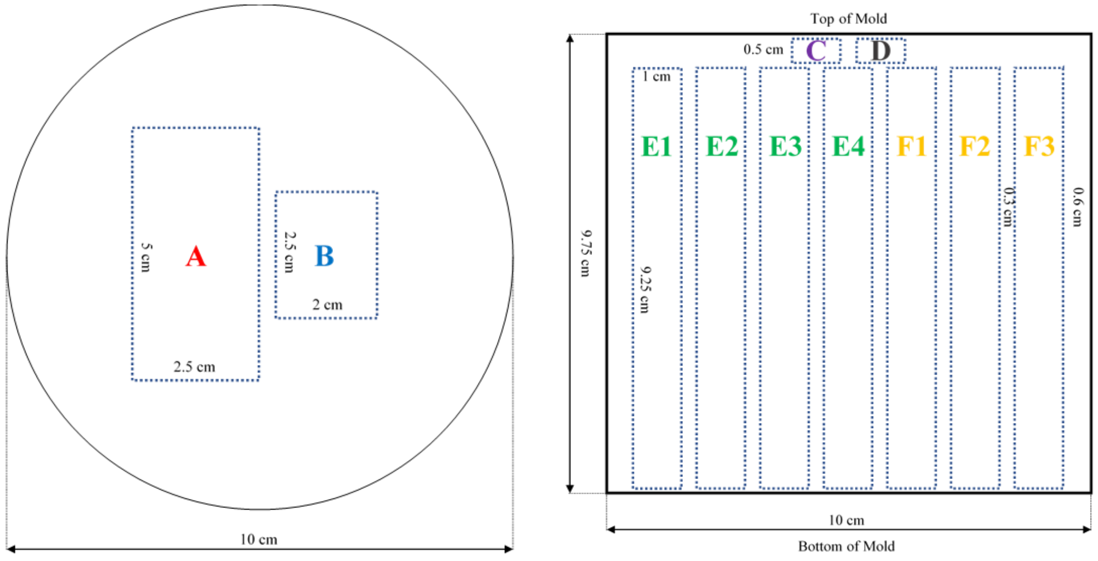

(a) (b)

Figure 2. Sample location in the experimental casting: top of mold (a) and vertical cross-section (b).

Table 2. Tests corresponding to sample identities shown in Figure 2.

Sample ID	Pitting Corrosion	Intergranular Corrosion	Segregation Study	Inclusion Analysis	Tensile Testing	Impact Testing
A	-	X	-	-	-	-
B	X	-	-	-	-	-
C	-	-	As-Cast	-	-	-
D	-	-	Heat Treated	X	-	-
E1-4	-	-	-	-	X	-
F1-3	-	-	-	-	-	X

The length of columnar grains growing from both walls were measured and averaged. A linear intercept method specified by the ASTM standard E112-13 was used to determine the grain size within the equiaxed zone at different heights in the casting. A grain refining factor (R) used by the authors in previous studies was employed to quantify the extent of refinement at each height (R = 0 for fully columnar structure and R = 1 for fully refined, equiaxed structure).[7] The grain refining factor is shown in Eq. (2):

$$R = \frac{D - 2 \times L_{columnar}}{D} \tag{2}$$

where: D is the diameter of the transverse section of the casting; and $L_{columnar}$ is the length of the columnar grains growing from one side of the mold. This same procedure was implemented to identify and characterize the macrostructure after heat treatment. The purpose was to identify the effect that heat treatment has on the as-cast grain size. A segregation study of the base and refined alloy before and after heat treatment was investigated. Two samples were taken from each set of castings. One was in the as-cast form (Sample C) while the other was in the heat-treated form (Sample D). These samples were mounted in Bakelite and polished in the following order: 360 grit→400 grit→600 grit→1200 grit→3 µm diamond paste→0.1 µm diamond paste. Eight SEM images of each sample were taken in ASPEX system using a back scattered electron detector that is sensitive to atomic number to reveal the extent of segregation in the interdendritic regions. These images were processed in ImageJ software to produce a binary image where area fraction of segregation can be quantified as is shown in Figure 3.

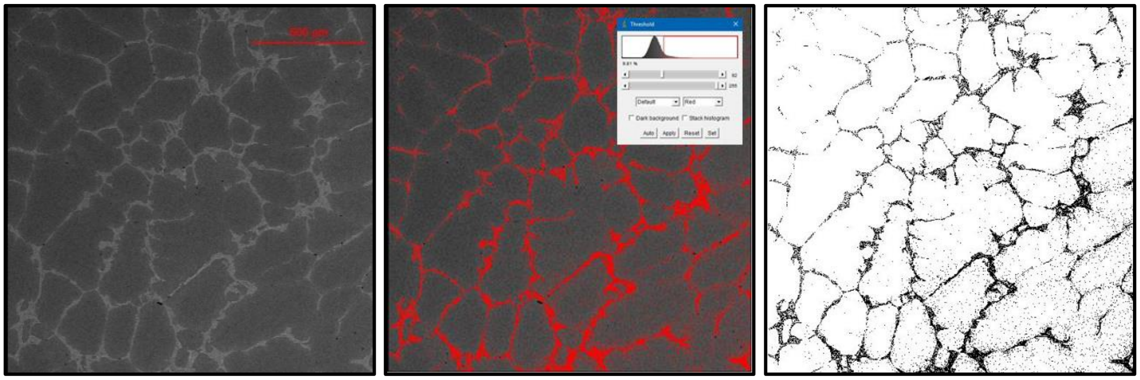

(a) (b) (c)

Figure 3. Methodology of evaluation of segregation: Original SEM image (a), adjusting thresholds (b), final binary image where area fraction of the segregated regions can be measured (c).

The segregated regions were classified into three main segregating elements (*Cr*, *Ni*, *Mo*) which were identified and measured using EDX in the ASPEX system. A ratio (*K*) of the concentration of each element in the segregated regions vs. the matrix was used to examine the concentration of the segregated regions as is shown in Eq. (3). The structure can be homogeneous ($K = 0$), the interdendritic region can be element rich ($K > 0$), or the interdendritic region can be element lean ($K < 0$):

$$K = (C_{interdendritic} - C_{matrix})/C_{matrix} \tag{3}$$

Multiplying the *K*-ratio by the estimated area fraction of the segregated region gives an approximation of the total element content in the segregated regions known as a segregation index shown in Eq. (4). Comparing segregation index before and after heat treatment will provide insight into the diffusion behavior of segregated elements in the base and refined alloys.

$$Segregation\ Index\ (SI) = K * Total\ Segregated\ Area, \% \tag{4}$$

Counting and classifying of inclusions was also performed using ASPEX SEM/EDX automated inclusion analyzer applying methodology described in article.[27] A total of 2,000 inclusions were counted per sample. These results were plotted on to joint ternary diagrams where each point presented three active elements in the recorded inclusion, and a table of the relevant inclusion statistics was generated.

2.3. CHARACTERIZATION OF PROPERTIES

Tensile and impact properties were characterized accordingly to the procedures outlined in ASTM standard A370-17a. For tensile testing, a small-size tensile bar of nominal diameter 0.25” was selected. Tensile bars were machined from Samples E1-4 on a CNC lathe. The ultimate tensile strength, yield strength, and strain for each alloy was determined from the stress-strain curves. These curves were obtained using an MTS Landmark servo-hydraulic test system running at a crosshead speed of 0.100 in/min while collecting data at 10 Hz. For impact properties, standard full-size Charpy V-notch specimens were used. Room temperature impact values were obtained using a Tinius Olsen Charpy testing machine.

Machining test specimens were prepared according to the schematic shown in Figure 5. The second heat in each casting set were carried out specifically to produce large specimens for the comprehensive machinability study. The chemistry of the heats is similar to those shown in Table 1. These castings were also heat treated accordingly to the heat schedule outlined in section 2.1. The as-cast surface layer was removed prior to starting each test. A live center was also used to increase the rigidity during machining. The machining tests were carried out on a HAAS TL-1 CNC lathe. The machining parameters were chosen for this study: cutting velocity 53 m/min, depth of cut 0.81 mm, feed rate 0.13 mm/rev, and dry cutting condition. A Sandvik Coromant SNMG 431 QM-235 coated cemented carbide tool was used for this study. Two fixed volume machining tests were completed for each condition to test the repeatability of the machining conditions. The test was completed after machining about 309 cm^3 of material. The progressive flank wear was measured throughout the test, and the final flank wear was recorded. The material with the lower final flank wear exhibited better machinability. Because material was removed during machining, the only qualitative observation of the real macrostructure was done visually on fine machined surface each time after several machining steps.

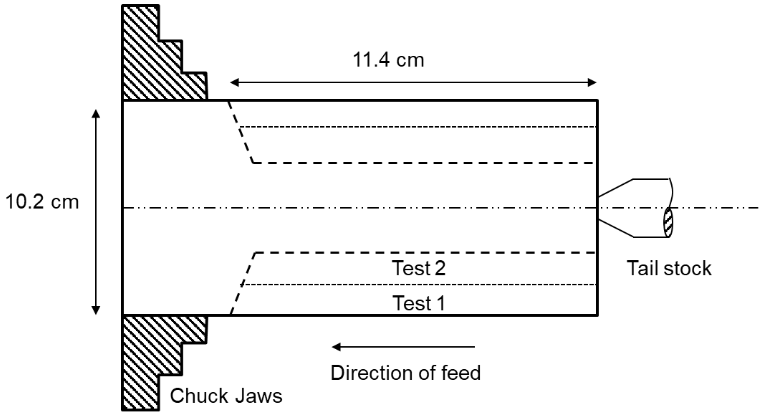

Figure 4. Machining test specimen.

Machine chips were collected and analyzed in a SEM to determine the influence of non-metallic inclusions on chip formation. The worn surfaces of the cutting tools were also investigated. These analyses were completed to determine the synergistic effects of non-metallic inclusions and grain size on machinability of superaustenitic stainless steel.

Two types of corrosion were of interest in this study. The first is intergranular corrosion outlined in ASTM standard A262-15 Practice B which submerges Sample B of the alloy in boiling ferric sulfate-sulfuric acid solution (≈ 100 °C) for 120 continuous hours. The initial mass and dimensions of the sample were measured before testing. After testing, the sample mass was remeasured and the corrosion rate was calculated using Eq. (5):

$$Mils\ per\ yr = (472 * 7305 * W)/(A * t * d) \tag{5}$$

where: W is weight loss in grams; A is the total surface area of the alloy exposed to the acidic solution; t is the time of exposure in hours; and d is the density of *Cr-Ni-Mo* steels at 8.00 g/cm^3. The second type of corrosion is pitting corrosion outlined in ASTM standard G48-11 Method A which submerges Sample A of the alloy in ferric chloride solution for a minimum of 72 hours at a constant temperature of 22 ± 2 °C. The test time was extended to 120 hours to ensure a measurable mass loss in the base alloy. The initial mass of the sample was measured. After testing, the sample mass was remeasured and the mass loss was calculated. Additionally, the surface features of the sample were characterized using a NANOVEA PS50 Optical Profilometer.

3. RESULTS & DISCUSSION

3.1. MACRO- AND MICRO-STRUCTURE

The macrostructure of the base and refined alloys are shown in Figure 5 for both as-cast and heat-treated conditions. Figure 5 (a,b) are the as-cast base alloy and (c) is the structure after heat treatment. Figure 5 (d,e) are the as-cast refined alloy and (f) is the structure after heat treatment. It is observed that the grain size of the refined alloy is much smaller than that of the base alloy.

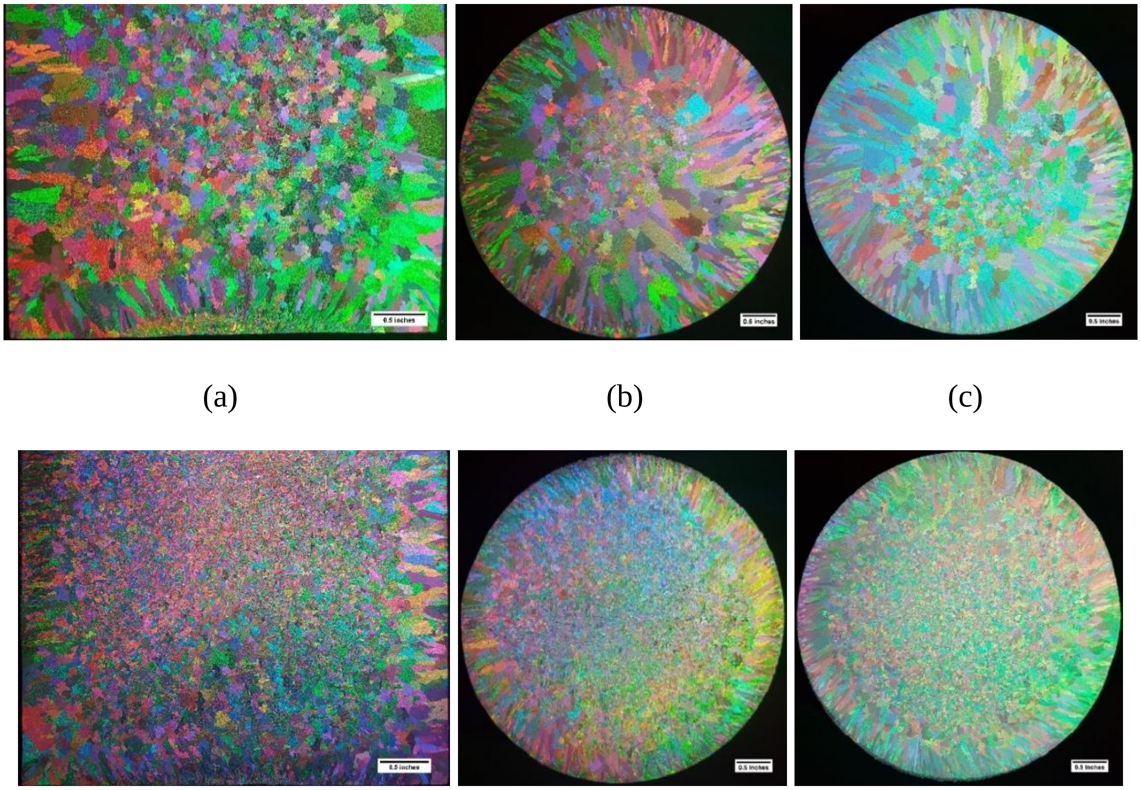

(a) (b) (c)

(d) (e) (f)

Figure 5. Macro-etched images of the base alloy in as-cast condition (a,b) and heat-treated condition (c); refined alloy in as-cast condition (d,e) and heat-treated condition (f).

To quantify the extent of grain refinement in both castings, ImageJ software was used to measure the equiaxed and columnar grain sizes in Figure 5 (b,c) and (e,f) (10 measurements each). These measurements are summarized in Table 3, and reveal that the refined alloy has a smaller average equiaxed and columnar grain size than the base alloy. Additionally, the as-cast grain size (equiaxed or columnar) does not appear to coarsen significantly after heat treatment. The as-cast columnar grains of the base alloy tend to be less uniform in size resulting in a larger variation in the measured value. Therefore, the difference in columnar grain size before and after heat treatment may be more related to how the grains were measured and less about the heat treatment changing the grain size. The grain refining factor (*R*) was then calculated using the columnar zone length. The grain refining factor of the base alloy changes in value as a result of the variation in columnar grain length. However, the as-cast grain size of the refined alloy remains intact after heat treatment thus the grain refining factor remains the same. This is significant because the grain size achieved by the designed inoculation practice is not affected by the post-process heat treatment.

Table 3. Grain size statistics of the base and refined alloys before and after heat treatment.

	Base		Refined	
Heat Treatment	Before	After	Before	After
Equiaxed grain size, mm	2.36 ± 0.10	2.36 ± 0.22	0.70 ± 0.01	0.69 ± 0.01
Columnar zone length, mm	22.4 ± 1.2	15.2 ± 1.0	9.38 ± 0.80	10.2 ± 0.6
Grain refining factor, R	0.65	0.76	0.85	0.83

Microstructural characterization of the as-cast, base alloy reveals islands of interdendritic segregation containing fine and coarse secondary phases as is shown in Figure 6(a). Further examination by elemental line scan reveals that the segregated regions are rich in *Cr* and *Mo* and deficient in *Ni* as is shown in Figure 6(b). An examination of the microstructural evaluation of as-cast CK3MCuN alloy, which is similar to the alloy in this study, was performed by the Steel Founders' Society of America.[28] In their evaluation, "islands" of segregation containing coarse and fine irregular-shaped secondary phases were observed extensively in the interdendritic regions and along grain boundaries. Through staining techniques, the fine irregular-shaped secondary phases within the islands were identified as σ-phase. Electron dispersive spectroscopy (EDS) analysis also revealed that the σ-phase was richer in *Cr* and *Mo* than the matrix. The coarse, irregular-shaped secondary phases within the islands remained unstained and EDS analysis revealed that it contained higher *Cr* and *Mo* concentrations than the σ-phase. These secondary phases were considered to be complex *Cr/Mo* carbides. It was also noted from this evaluation that all secondary phases within the islands were dissolved after solution annealing at 1260 ^{o}C (2300 ^{o}F) and water quenching.[28] Therefore, proper heat treatment is crucial for the homogenization of *Cr-Ni-Mo* throughout the matrix and the dissolution of secondary phases. Both an improper heat treatment and a coarse cast structure will result in the degradation of the alloy's properties.

The segregated regions were quantified for the base and refined alloys before and after heat treatment. SEM images for each condition are shown in Figure 7: base as-cast (a) and heat treated (b), and refined as-cast (c) and heat treated (d). Heat treatment has an observable effect of homogenizing the matrix and dissolving secondary phases. The calculated area percentage of segregation is included in each image and represents the average area fraction for the eight SEM images taken for each condition. It should be noted that the refined alloy has less segregation than the base alloy both in the as-cast and heat-treated conditions.

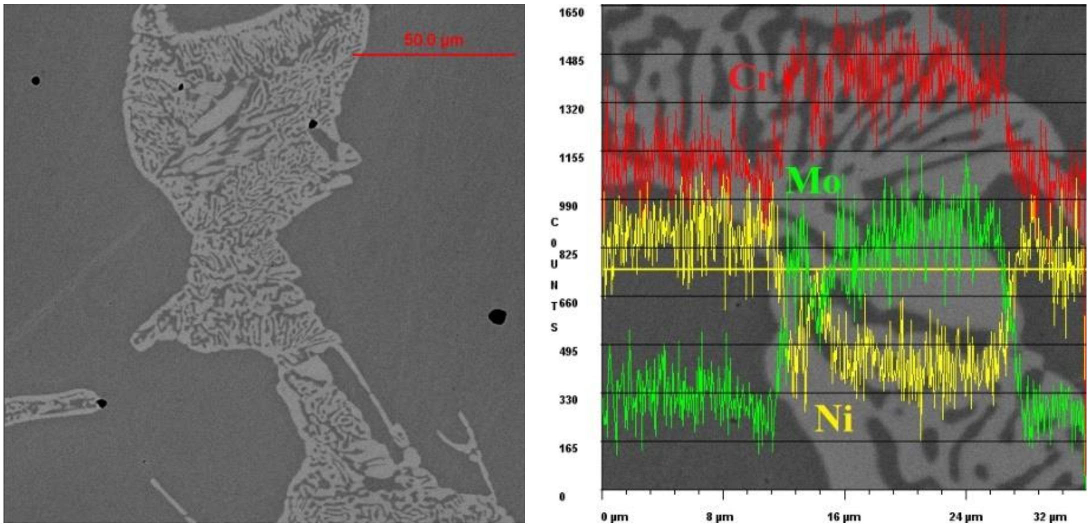

(a) (b)

Figure 6. As-cast microstructure of base alloy showing secondary phases formed in the segregated regions (a); corresponding elemental line scan of the segregated region at higher magnification (b).

The calculated segregation index verifies that a significant reduction in segregation occurs after heat treatment of both alloys which is shown in Figure 8. This is a result of homogenization of the matrix due to dissolution of secondary phases with diffusion of *Cr* and *Mo* into the matrix and *Ni* into the segregated regions. Segregation index shows that the segregated regions are rich in *Cr* and *Mo* and deficient of *Ni*. In the as-cast condition, both alloys exhibit similar amounts of segregation. However, in the heat-treated condition the refined alloy has less segregated elements indicating better homogenization of the segregated elements. Grain refinement increases the length of grain boundaries which provides more diffusion paths for the segregated elements during heat treatment resulting in a higher diffusion rate.[29] Diffusion rate along grain boundaries will always be higher than the diffusion rate through the matrix/lattice.

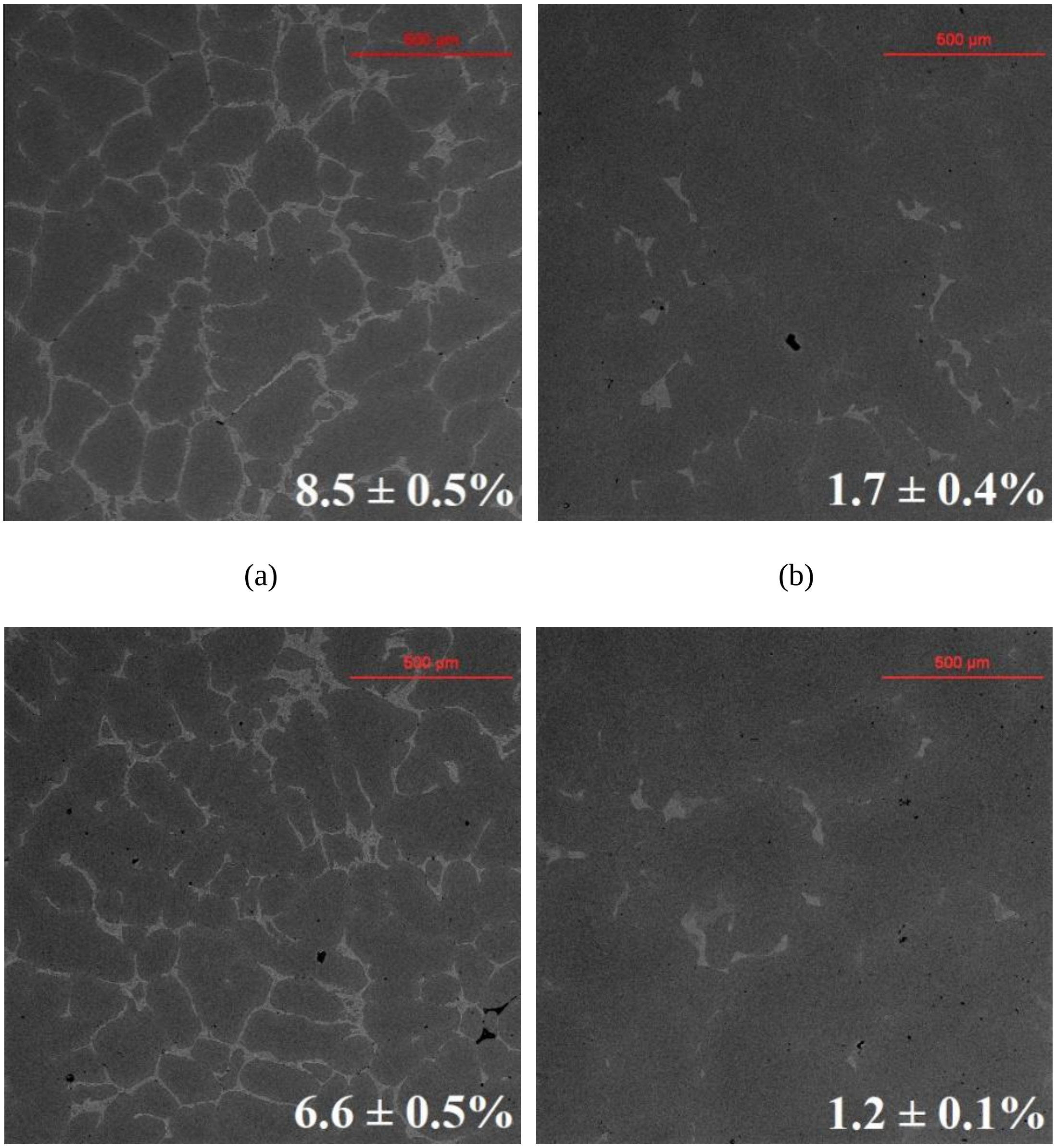

(a) (b)

(c) (d)

Figure 7. SEM images of the segregated elements in the interdendritic regions for the base alloy: as-cast (a) and heat treated (b); and the refined alloy: as-cast (c) and heat treated (d).

The calculated area fraction of segregation in the as-cast base and refined alloys were used to estimate the fraction of enriched liquid remaining just prior to solidification.

These values were plotted against the corresponding *K*-ratio of *Cr*, *Ni*, and *Mo* in the segregated regions *vs* the matrix shown in Figure 9. A rectangular area EDX scan of the segregated region that contains secondary phases was used to approximate the composition of the enriched liquid (averaging the composition of secondary phases).

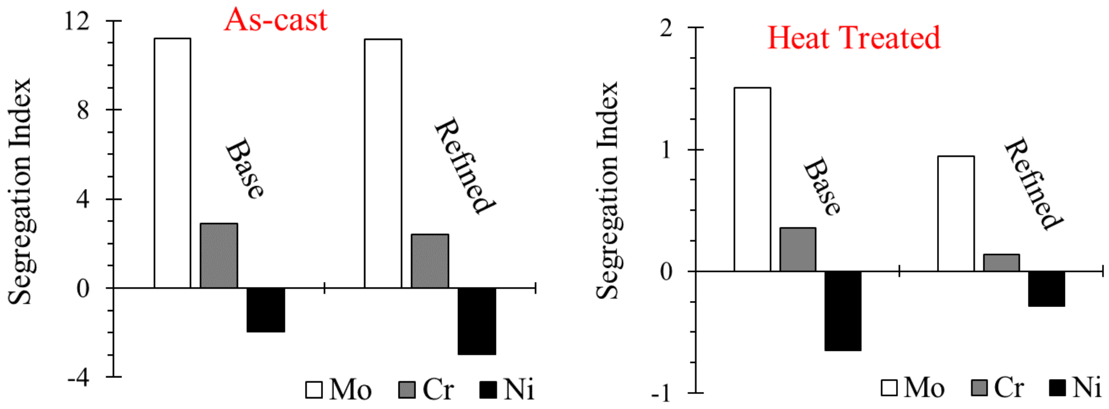

Figure 8. Element distribution in the segregated regions of the base and refined alloys in the as-cast and heat-treated conditions.

It was assumed that a limited amount of solid-state diffusion into and out of the segregated regions would occur during cooling of the casting because: (i) *Cr*, *Ni*, and *Mo* diffuse much slower than interstitial atoms and (ii) the cooling rate is fast enough to prevent homogenization of the matrix. These experimental values were compared with thermodynamic equilibrium and Scheil solidification simulations which were performed with FactSage 7.0 software using FactPS and FSstel databases.[30] The experimental values agree with the simulated Scheil solidification model indicating the consumption of *Ni* during the formation of austenite dendrites, the rejection of *Cr*-*Mo* into the liquid from the austenite dendrites, and the solidification of the enriched liquid which is then followed by the formation of secondary phases (σ-phase, *Cr/Mo* carbides) upon cooling.

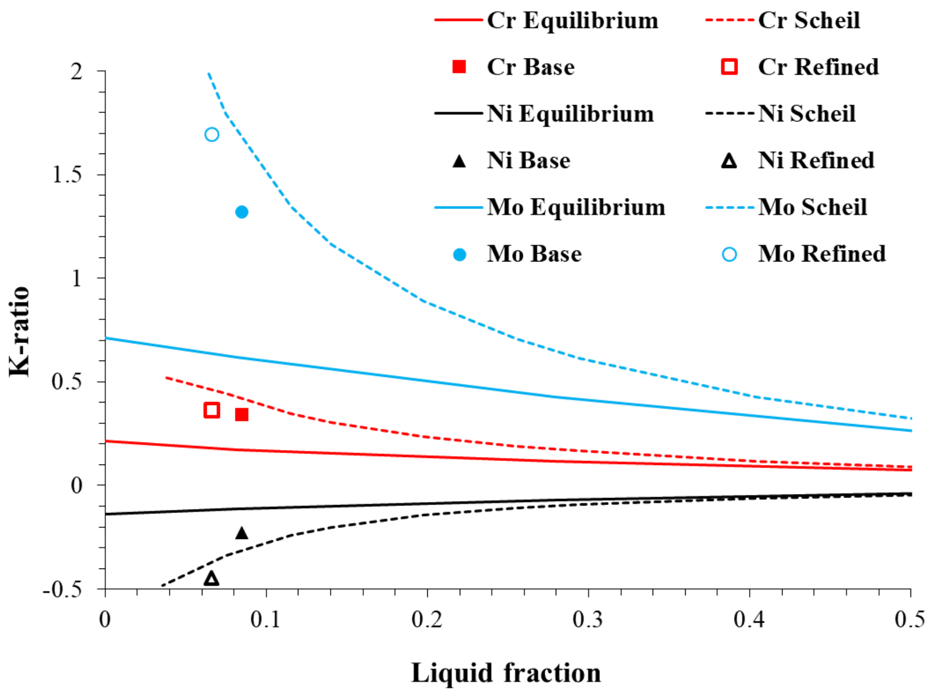

Figure 9. Comparison of thermodynamically simulated (equilibrium and Scheil solidification models) and experimental segregations (EDX collected concentrations) observed in the as-cast condition.

To evaluate non-metallic inclusion family, a total of 2,000 inclusions were quantified and classified in each alloy using an automated SEM/EDX ASPEX inclusion analyzer.[27] The main inclusion recorded in the base alloy was complex *Al-Mn-Si-Ca* inclusions. The primary inclusion in the refined alloy was titanium nitrides (*TiN*) and *Al-Mg* spinel. An elemental line scan of the *TiN* and spinel is shown in Figure 10(a) where the detected elements are *Mg-Al-Ti*. A 3D SEM image of an electrolytically extracted *TiN* and spinel inclusions are shown in Figure 10(b). These non-metallic inclusions have sharp edges and the tendency to cluster.[7]

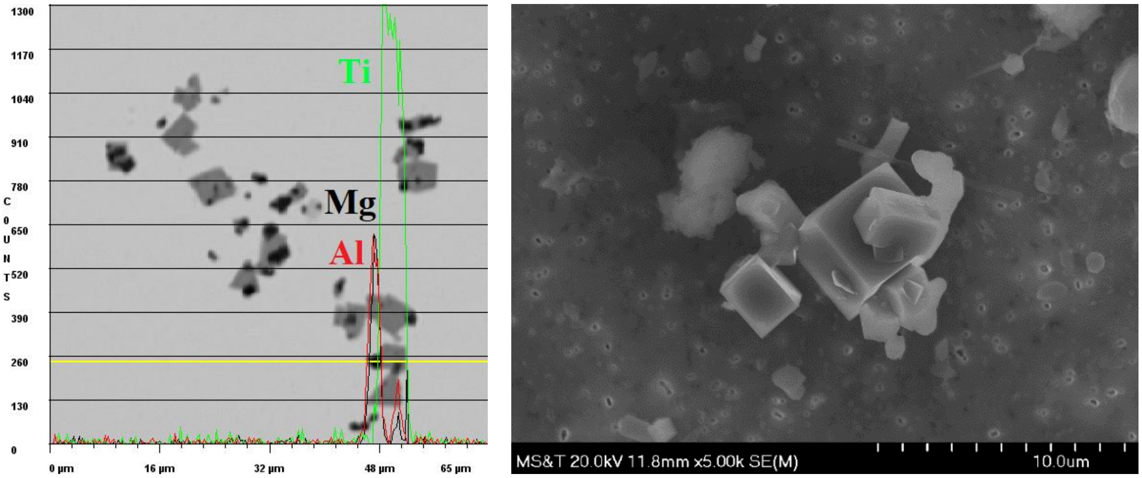

(a) (b)

Figure 10. Elemental line scan of *TiN* (gray) precipitated on *Al-Mg* spinel cores (dark) inclusions (a); SEM image of extracted *TiN* with visible spinel cores inclusions.

A summary of the inclusion statistics is outlined in Table 4. Area fraction is the amount of inclusions recorded across the total scan area. Inclusion density is the number of inclusions recorded per area unit. The average inclusion composition normalized to 100% is listed in wt.%. The refined alloy has nearly three times the amount of inclusions compared to the base alloy.

3.2. EFFECT OF GRAIN REFINEMENT ON PROPERTIES

Tensile test. The results of tensile testing in the heat-treated condition are summarized in Figure 11. The stress-strain curve for both alloys are shown in Figure 11(a). An increase in the tensile strength and ductility can be seen from this plot. The ultimate tensile strength increased by 9%, yield strength increased by 13%, and ductility increased by 9%. The corresponding values with standard deviation are shown also in Figure 11(b,c) with both the engineering and true values provided.

Table 4. Inclusion statistics and average inclusion chemistry (wt.%) of the base and refined alloys.

Steel	Area Fraction, ppm	Inclusion Density, #/mm^2	N	Mg	Al	Si	S	Ca	Ti	Mn
Base	365	57	0	1	40	14	4	7	0	34
Refined	910	183	17	5	10	6	2	5	46	10

The increase in strength is most likely caused by the decrease in grain size. The increase in ductility may be related to the additional reduction in segregation of the refined alloy that was previously discussed.

Toughness. Superaustenic stainless steel has a combination of high strength, large elongation and medium toughness when compared to austenitic steels alloyed with less *Mo*. Room temperature impact strength slightly decreased for the refined alloy which is illustrated in Figure 12(a). An SEM image of the fracture surface of the base alloy is shown in Figure 12(b). At the bottom of some of the craters were *Al-Mn-Si-Ca* inclusions that acted as weak points for fracture to occur. Most of the craters did not have inclusions in them. However, the refined alloy in Figure 12(c) possessed many more craters most with inclusions in them. The round inclusions are *MnS* while the black spots at the bottom of some of the craters are *TiN* and spinel. The increased number of inclusions act as crack initiation sites and often is where fracture occurs. The large standard deviation of the base alloy may be a result of orientation of the columnar grains relative to the direction of impact force while the smaller deviation of the refined alloy may be indicative of uniform grain size relative to the direction of impact force.

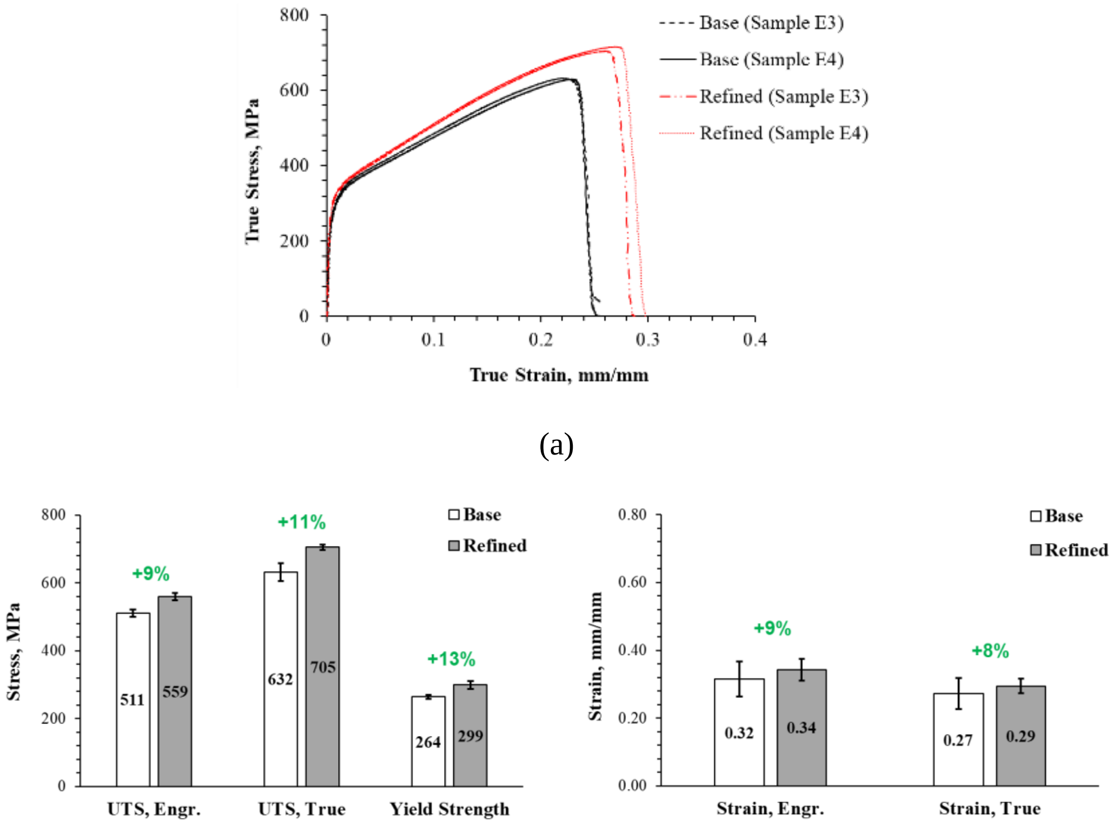

(a)

(b) (c)

Figure 11. Stress-strain curves (a) and results for tensile tests (b) and (c) of the base and refined steels.

Machining. Heavy section castings from superaustenitic steel were subjected to intensive machining. The effect of grain refinement on machinability was verified on the second set of experimental castings. The average grain size was qualitatively estimated during machining for the top, middle, and bottom position of cut section in the base and inoculated castings, and are shown in Table 5. The casting from the base steel has a significantly coarser grain size overall when compared to the refined casting. The refined casting has a finer grain size due to the addition of active nuclei in the melting process. For example, the top section the base casting has a grain size of 8.0 mm while the refined casting has a grain size of 2.9 mm; however, in studied heavy section casting, the grain size near the chilled bottom are similar in both conditions.

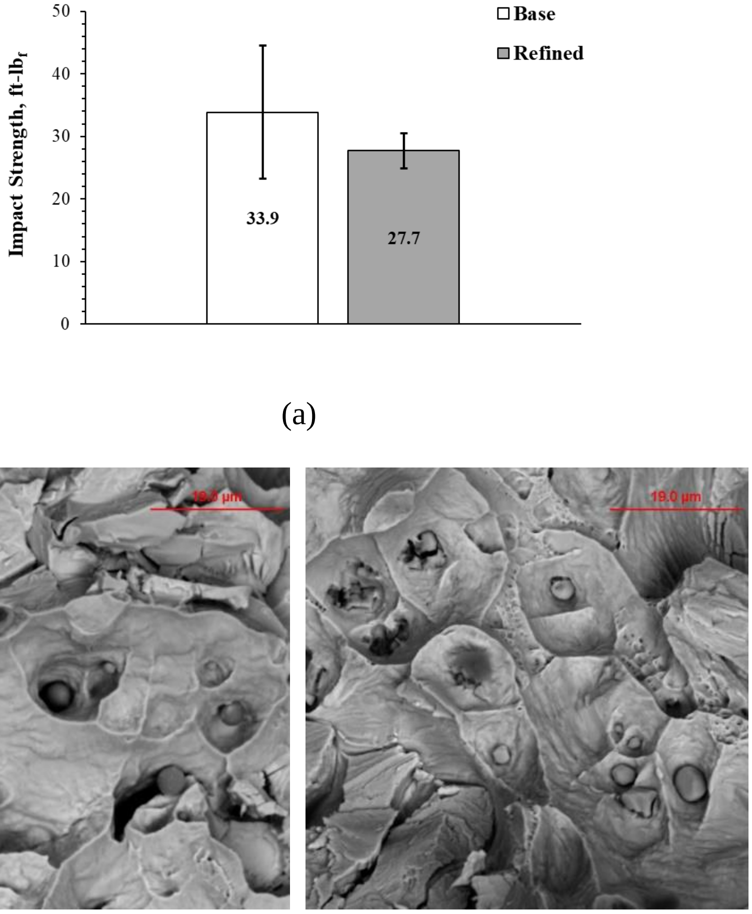

(a)

(b) (c)

Figure 12. Impact strength (a) and SEM images of fracture of base (b) and refined (c) steels.

Table 5. Average grain size for the unmodified and modified steels.

Parameter	Base			Refined		
	Bottom	Middle	Top	Bottom	Middle	Top
Average grain size, mm	3.3	6.6	8.0	2.7	4.7	2.9

The progressive flank wear measurements from the machining tests can be seen in Figure 13. The refined castings had a final flank wear value of 0.188 mm, although the base castings had a final flank value of around 0.21 mm after machining an equivalent volume of material. The second test showed good repeatability of measured flank wear. This results in a 13% decrease in flank wear for the refined casting when machining under the same cutting conditions, and giving the refined castings a slightly improved machinability.

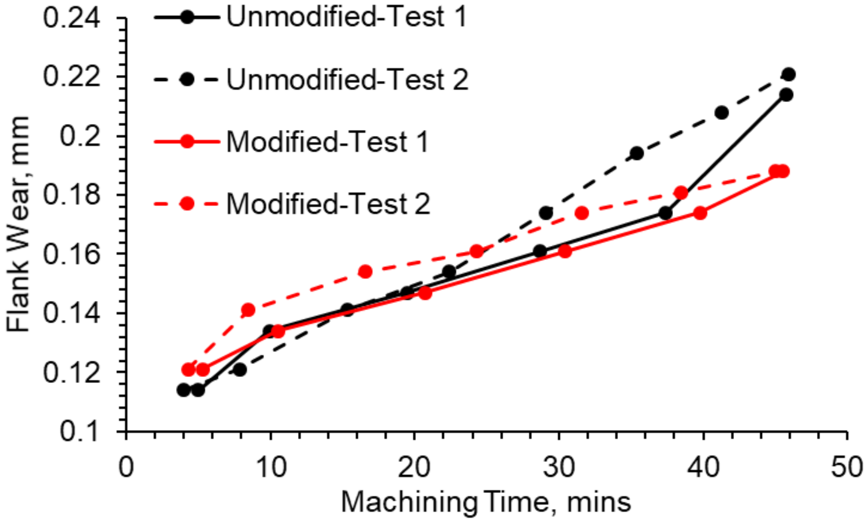

Figure 13. Progressive flank wear curves for the base and refined steels. The machining parameters were chosen for this study: cutting velocity 53 m/min, depth of cut 0.81 mm, feed rate 0.13 mm/rev, and dry cutting condition.

There are several factors that could affect the machinability in grain refined steels including grain size, segregations and non-metallic inclusions. A decrease in grain size and segregations was observed for the refined alloy using *TiN* and *Al-Mg* spinel inclusions. The inclusions present in the base casting are complex oxides containing *Mn-Al-Ti* and some *MnS* inclusions. Overall, the inclusion populations are consistent throughout the machining volume when comparing the top and the bottom locations. However, the inclusion population density was nearly 4 times larger in the refined alloy.

Jiang et al. varied the grain size of a 304 stainless steel by hot working, and observed that the finer grain size specimens exhibited better machinability.[21] Holappa et al. reported a clean steel will have a detrimental effect on machinability.[22] Multiple authors show that the presence of abrasive oxide inclusions in different steels will lead to an increase in tool wear, and that a higher volume fraction of abrasive inclusions decrease tool life.[23-25] From these reported results it seems that the presence of specific types of inclusions can be beneficial for machinability, but too many abrasive inclusions can lead to aggressive tool wear. No previous studies investigate the combined effects of non-metallic inclusions and grain size. The benefit of the finer grain size of the modified steel offsets the negative effect of abrasive non-metallic inclusions present in the steel.

The cutting tools used in both steels showed built-up edge, flank wear, some chipping wear, and excessive notch wear. The rake surface of the worn cutting tools shown in Figure 14 was investigated. Figures 14(a,b) are the surfaces of the cutting tools for the base and refined steels respectively. A noticeable difference in the region of the rake surface that the chips flow over was observed between these two steels. Inclusions present in both the base and refined steels were found in the chip flow region. Table 6 shows the elemental makeup of the inclusions found on the machining tool. The same type of complex oxide found in the case of the base condition. It can also be seen that in the case of the refined condition *TiN* and $MgAl_2O_4$ spinel inclusions were observed on the cutting tool.

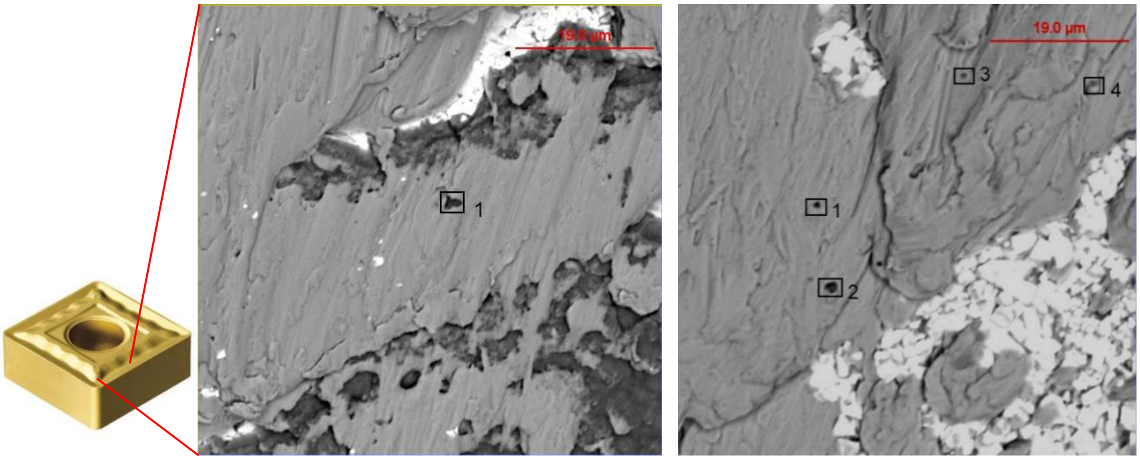

(a) (b)

Figure 14. The SEM image of rake surface of the cutting tool used for machining the base steel (a) and the refined steel (b). The chemical composition of the inclusions observed on the rake surface are listed in the table below.

Table 6. EDX Results of the Inclusions Found on the Rake Surface of the Cutting Tool.

Steel	Area	*Cr*	*Mn*	*N*	*Ti*	*Al*	*Mg*
Base	1	47.3	39.7	-	6.7	6.3	-
Refined	1	-	-	-	-	79.7	20.3
	2	-	-	-	-	77.5	22.5
	3	-	-	22.2	77.8	-	-
	4	-	-	30.2	66.7	-	-

Machine chips for both base and refined conditions were also observed in SEM. The serrated type of chips shown in Figure 15(a) were formed under the machining conditions for both steels. Higher magnification of the SEM images in Figure 15(b,c) show a region of the machine chip from the refined steel that was heavily deformed during machining. The EDX results from points 1, 2, and 3 can be seen in Table 7**.** Area 1 is the matrix which consists of *Fe*, *Cr*, *Ni*, and *Mo*. Area 2 is a fractured *TiN* inclusion, and the other voids above the crack are visible in Figure 15(c) which showed signals of fractured *TiN* inclusions. Area 3 is a second phase that is rich in *Cr* and *Mo*, but lean in *Ni* this is evident of the σ-phase found in high alloyed stainless steels. This phase is obviously brittle due to it being fractured in multiple areas.[9] Both steels have σ-phase present in the steel, which can weaken the matrix material during machining. The refined steel has a higher volume fraction of inclusions which fractured during machining. This could lead to a lower force required for machining. Zanatta et al. found fractured *Ti(C,N)* inclusions in their chip analysis when machining VP100 mold steel.[26] They measured cutting forces during machining and showed a decrease in cutting forces when machining steel with elevated *Ti* content, in the form of *Ti(C,N)* inclusions. They claimed this could be due to the fracture of the inclusions during machining. Singh et al. also observed a decrease in tool forces during machining a steel with a higher volume fraction of hard inclusions.[24] However, both studies show an increase in flank wear when machining steels with a higher volume fraction of hard inclusions. The lower flank wear reported in this study could be due to the finer grain size of the modified steel which balances the negative effect of the higher volume fraction of *TiN* inclusions.

Corrosion. The results of two types of corrosion tests for both alloys are summarized in Figure 16 for pitting (a) and intergranular (b) corrosion. The mass loss from pitting corrosion was nearly four times higher for the refined steel compared to the base steel, however, corrosion rate was lower in refined steels. This contradiction in results could be related to the different corrosion mechanisms.

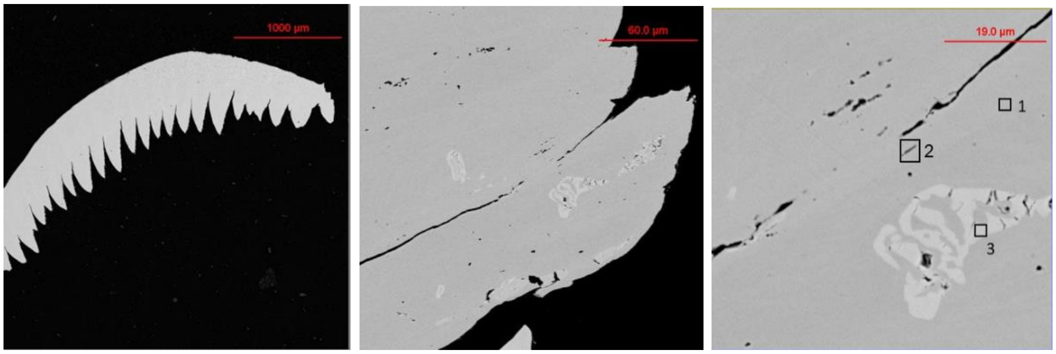

(a) (b) (c)

Figure 15. SEM image of a representative machine chip collected during machining (a) (both steels had serrated chips present in machining), (b) and (c) are higher magnification SEM images of a machine chip showing fractured σ-phase and *TiN* inclusions. The EDX results of the points in (c) can be seen in the table below.

Table 7. EDX analysis (wt.%) of the points shown in Figure 15(c).

Area	*Fe*	*Cr*	*Ni*	*Mo*	*Ti*
1	53.2	22.7	18	4.8	-
2	42.8	18.1	15.1	4	18
3	50.2	27.3	11.4	9.3	-

The degradation of corrosion resistance to pitting is caused by concentration gradients in the matrix around the *TiN* and spinel inclusions which create areas that are susceptible to dissolving in the ferric chloride solution. These inclusions create weak points for the corrosive solution to penetrate the sample and create deep pits shown in Figure 17. The maximum pit depth recorded in the base alloy was 101 µm and in the refined alloy was

134 µm. Minimizing the clustering of *TiN* and spinel inclusions may reduce the mass losses from pitting corrosion experienced in the refined alloy. However, the results of the intergranular corrosion test show an improved 30% decrease in the corrosion rate of the refined alloy compared to the base alloy shown in Figure 17(b). This may be related to the reduced overall segregation that was achieved in the refined alloy.

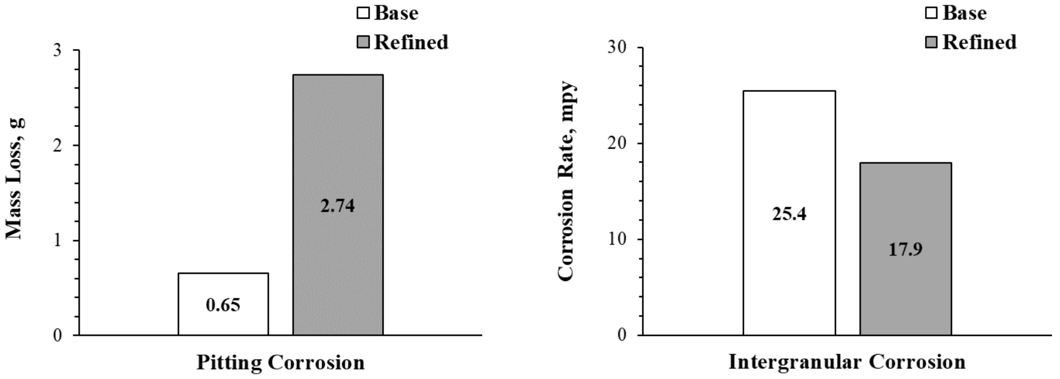

(a) (b)

Figure 16. Corrosion test results: (a) ASTM G48-11 Method A and (b) ASTM A262-15 Practice B.

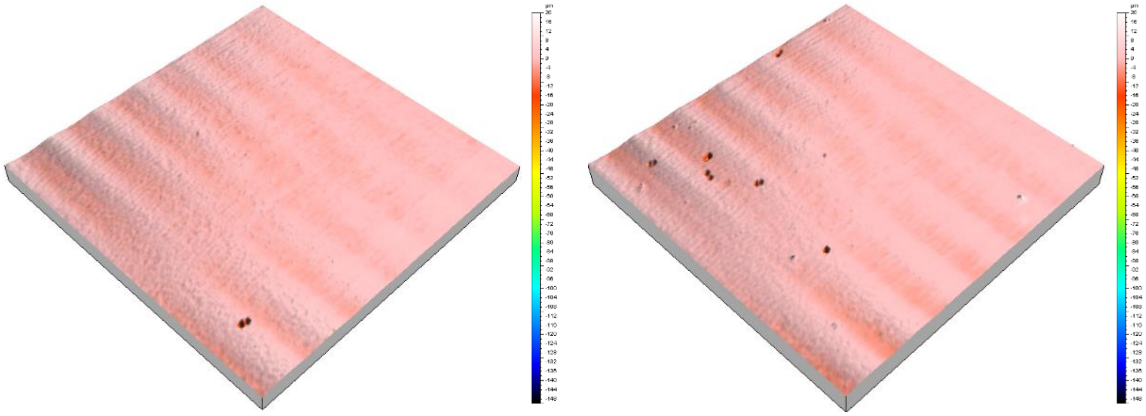

(a) (b)

Figure 17. Optical profile of pitting corrosion for base (a) and refined (b) steels.

4. CONCLUSION

The properties of an unmodified (base) and grain refined (refined) superaustenitic stainless steel were characterized in this work. Grain refinement was achieved by melt inoculation that promoted the co-precipitation of TiN on to $MgAl_2O_4$ inclusions that act as heterogeneous nuclei for austenite during solidification. These castings were subjected to a homogenization heat treatment. No coarsening or additional grain refining of the as-cast grain structure were observed after heat treatment in either the base or refined alloys. Examination of the segregation behavior revealed that the grain refined structure was more effective at dissolving secondary phases and homogenizing the matrix after heat treatment than the base alloy. Comparison of the measured experimental segregations *vs* thermodynamic simulations shows the segregated regions have compositions similar to the enriched liquid predicted by Scheil solidification model.

The tensile properties of the refined alloy show a 9% increase in ultimate tensile strength, a 13% increase in yield strength, and a 9% increase in ductility compared to the base alloy. The increases in strength are attributed to the reduction in grain size (Hall-Petch effect) while the increase in ductility may be a result of the improved homogenization of the segregated regions. Room temperature impact strength of the refined alloy slightly decreased which may be related to the increased quantity of inclusions that act as sites for crack initiation, propagation, and growth. However, refined steel has less variation of impact toughness which could be related to more isotropic grain orientation.

The refined steel exhibited slightly improved machinability by decreasing the final flank wear by 13% for the fixed volume of machined material when compared to the base steel. The fine grain size offset the negative effect of inclusions present in the modified steel when compared to the unmodified condition. Mass losses due to pitting corrosion were nearly four times larger for the refined alloy than the base alloy. These pits were caused by the dissolving of clustered *TiN* and spinel inclusions in ferric chloride solution. However, the refined alloy experienced a 30% decrease in corrosion rate during intergranular corrosion testing. This improvement may be related to the improved homogenization of the segregated regions.

Determination of whether the base or grain refined superaustenitic steels is better is purely based on application and operating conditions. The base alloy has better pitting corrosion resistance while the refined alloy has improved strength, machinability, and a decrease in intergranular corrosion rate.

REFERENCES

1. D. Siafakas, *Thesis at Jönköping University*, 2017.
2. M. Andersson et al., *European Commission*, 2011.
3. R. Tuttle, *Office of Naval Research*, 2009.
4. F. Pan et al., *Materials,* 2016, 9(6), pp. 1-19.
5. R. Tuttle, *Office of Naval Research*, 2010.
6. C. Van der Eijk et al., *ISIJ Int.*, 2009, 49(7), pp. 1046-50.
7. S. Lekakh et al., *Metall. Mater. Trans. B*, 2017, 48(1), pp. 406-19.
8. P. Schweitzer, Corrosion Engr. Handbook, 2nd ed., *CRC Press*, 2006, pp. 274.
9. J. DuPont, J. Farren, A. Stockdale, B. Leister, *U.S. Dept. of Energy*, 2004-2012.
10. K. Ralston, N. Birbilis, C. Davies, *Scr. Mater.*, 2010, 63(12), pp. 1201-04.
11. H. Li et al., *Int. J. Electrochem. Sci.*, 2015, 10(6), pp. 4832–48.

12. Y. Li, A. Bushby, D. Dunstan, *Proc. Royal Soc. A: Math. Phys. Eng. Sci.*, 2016, 472(2190).

13. L. Huabing et al., *Mater. Des.*, 2017, 118(22), pp. 207-17.

14. S. Li, G. Cui, *J. Appl. Phys.*, 2007, 101(8).

15. F. Klocke, A. Kuchle, Manufacturing Processes 1 Cutting, *Springer*, 2013.

16. N. Ånmark, A. Karasev, P. Jönsson, *Materials*, 2015, 8(2), pp. 751-83.

17. M. Alabdullah, A. Polishetty, J. Nomani, G. Littelfair, *Int. J. Adv. Manuf. Tech.*, 2016, 91(1-4), pp. 501-16.

18. M. Alabdullah, A. Polishetty, J. Nomani, *Materwiss Werksttech*, 2017, 48(3-4), pp. 190-197.

19. A. Polishetty, M. Alabdullah, G. Littelfair, *MATEC Web of Conferences*, 2017, 95.

20. T. Komatsu, T. Yoshino, T. Matsumura, S. Torizuka, *Procedia CIRP*, 2012, 1, pp. 150-55.

21. L. Jiang, Å. Roos, P. Liu, *Metall. Mater. Trans A*, 1997, 28(11), pp. 2415-22.

22. L. Holappa, A. Helle, *J. Mater. Process. Technol.*, 1995, 53(1-2), pp. 177-86.

23. Z. Hong, X. Wu, C. Kun, *Steel Research*, 1995, 66(2), pp. 72-76.

24. S. Singh, A. Chakrabarti, A. Chattopadhyay, *J. Mater. Process. Technol.*, 1997, 66(1-3), pp. 90-96.

25. G. Faulring, S. Ramalingam, *Metall. Trans. A*, 1979, 10(11), pp. 1781-88.

26. A. Zanatta, J. Gomes, J. Bressan, C. Barbosa, *Adv. Mater. Res.*, 2011, 223, pp. 464-72.

27. M. Harris et al., *AISTech Proceedings*, 2015, pp. 3315–25.

28. C. Lundin, S. Wen, W. Liu, G. Zhou, *Steel Founders' Society of America*, 2002, Report A-95

29. M. Mohebi-Moghadam,, *Thesis at Lehigh University*, 2015.

30. Factsage 7.0 software, GTT-Technologies, Aachen. www.gtt-technologies.de.

SECTION

4. CONCLUSION

The goal of this research project is to develop an industrially viable melting process that will control the crystallization macrostructure of austenitic grades of cast steels. Titanium nitride has proven to be an effective grain refiner of austenite, and spinel is known to be a favorable site for the epitaxial growth of titanium nitride. Therefore, theoretical simulation and experimental application has led to the development of a repeatable grain refining melt process for austenitic stainless steel 316L alloys.

The effect of solidification sequence on the establishment of a columnar-to-equiaxed transition (CET) was investigated. Images taken of the etched macrostructure for each experimental casting shows that single-phase solidification heat #1 and heat #3 achieved grain refinement while mixed ferrite-austenite solidification mode heat #2 did not. This was explained by the independence of growth between the primary ferrite and secondary austenite phases which results in more difficult thermal and growth conditions for equiaxed growth of the secondary phase. The absence of a CET and a mix of equiaxed ferrite grains and columnar austenite grains in the final structure can therefore be explained.

Two grain refining methods that introduced titanium nitride (TiN) into 316L melt by in-situ formation and by master alloy addition were designed, performed, compared and discussed. The master alloy method extended the equiaxed zone and improved the distribution of TiN in the casting (less clustering). However, this method showed less effective grain size refinement when compared to the in-situ method.

The effect of the developed grain refining melt practice on the properties of the castings was examined. Heat treatment had no effect on the as-cast grain size of the grain refined 316L and CK3MCuN stainless steels. Grain refined 316L stainless steel exhibited an increase in ultimate tensile strength (12%) and yield strength (21%), and a decrease in ductility (8%). There were also decreases in impact strength, pitting corrosion resistance, intergranular corrosion rate, and no change in hardness. Grain refined CK3MCuN stainless steel exhibited a reduction in segregation after heat treatment, and an increase in ultimate tensile strength (11%), yield strength (13%), and ductility (8%) in comparison to the unmodified scenario. There were also decreases in impact strength, pitting corrosion resistance, no change in hardness, and a decrease in intergranular corrosion rate.

5. FUTURE WORK

The following is a list of ideas for future work in the continuation of this research. The mechanisms contributing to the challenge of grain refining ferrite-austenite solidification mode stainless steels must be further investigated. Addressing this challenge will lead to the development of new inoculation treatments and techniques for duplex grades of stainless steels.

Additional development of novel master alloy designs need to be explored such as by wire feeding, powder, or in-mold applications. Dissolution trials of master alloy nuclei in a melt with different degrees of nitrogen supersaturation is crucial for gauging survivability of the nuclei.

Discover more effective heterogeneous nuclei for austenitic alloys. Additional inclusion engineering may include: preventing floatation of nuclei in the melt by having the nuclei co-precipitate on to a heavier oxide core; manipulating nuclei shape for more effective heterogeneous nucleation; and exploring cross soluble forms of potential heterogeneous nuclei to further decrease the amount of melt supersaturation required to form within the melt. One example includes the cross solubility of titanium nitride and titanium oxides.

Further characterization of refined alloy properties at elevated operating temperatures must be investigated. Austenitic stainless steel alloys are commonly used in extreme temperature applications.

APPENDIX

UNPUBLISHED WORKS

The work contained in this thesis was supported by the Peaslee Steel Manufacturing Research Center (PSMRC). Annual reports and semester presentations were given to inform industry members of current results and project progress. Interpretation of these results are outlined in the following PSMRC documents listed below:

1. D.A. Arvola, R.J. O'Malley, S.N. Lekakh, and L.N. Bartlett, PSMRC Meeting, December 1, 2016, Rolla Missouri.
2. D.A. Arvola, R.J. O'Malley, S.N. Lekakh, and L.N. Bartlett, PSMRC Meeting, May 4, 2017, Rolla Missouri.
3. D.A. Arvola, R.J. O'Malley, S.N. Lekakh, and L.N. Bartlett, "Year 4: Grain Refinement of Austenitic Grades and Low Alloy Carbon Steels in Heavy Section Castings," PSMRC Annual Report, Missouri S&T, 2017.
4. D.A. Arvola, R.J. O'Malley, S.N. Lekakh, and L.N. Bartlett, PSMRC Meeting, November 30, 2017, Rolla Missouri.
5. D.A. Arvola, R.J. O'Malley, S.N. Lekakh, and L.N. Bartlett, PSMRC Meeting, May 3, 2018, Rolla Missouri.
6. D.A. Arvola, R.J. O'Malley, S.N. Lekakh, and L.N. Bartlett, "Year 5: Grain Refinement of Austenitic Stainless Steel in Heavy Section Castings," PSMRC Annual Report, Missouri S&T, 2018.

BIBLIOGRAPHY

[1] W. Martienssen and H. Warlimont, “Iron and Steels,” *Springer Handbook of Condensed Matter and Materials Data*, Springer Science & Business Media, Germany, 2006, pp. 252-256.

[2] F. Campbell, “Stainless Steels,” *Elements of Metallurgy and Engineering Alloys*, ASM International, Ohio, 2008, pp. 12-34, 441-451.

[3] M. McGuire, “Austenitic Stainless Steels,” *Stainless Steels for Design Engineers*, ASM International, Ohio, 2008, pp. 69-90, 92.

[4] J. Campbell, “Post-casting processing,” *Complete Casting Handbook: Metal Casting Processes, Metallurgy, Techniques and Design*, Elsevier Ltd., United Kingdom, 2011, pp. 1067-1090.

[5] Z. Morita and T. Emi, “Manufacturing Process for Iron and Steel,” *Introduction to Iron and Steel Processing*, JFE 21st Century Foundation, Japan, 2003, pp. 2A.

[6] The Casting Process, *Carson Castings*, 2017

[7] S. Biswas, K. Peaslee, and S. Lekakh, “Increasing Melting Energy Efficiency in Steel Foundries,” *Transactions of the American Foundry Society*, Vol. 120, No. 45, April 2012, pp.449–456.

[8] T. Bowers and M. Flemings, “Structure of Dendrites at Chill Surfaces,” *Transactions of the Metallurgical Society of AIME*, Vol. 239, October 1967, pp. 1620-1625.

[9] Casting structure, *FOUNDRY LEXICON*, 2017.

[10] D. Porter and K. Easterling, “Solidification of Ingots and Castings,” *Phase Transformations in Metals and Alloys*, Chapman & Hall, United Kingdom, 1992, pp. 233-236.

[11] K. Tamtal and D. Karunakar, “Grain Refinement of Cast Alloys: A Review,” *National Conference on RAME*, Vol. 1, No.1, January 2014, pp. 1-14.

[12] P. Kumar and A. Choudhury, “A Brief Review on Grain Refinement In Steel Through Dynamic Strain Induced Transformation,” *Journal of Materials Science & Surface Engineering*, Vol. 4, No. 5, September 2016, pp. 436-443.

[13] J. Wallace, N. Church, and P. Wieser, "Grain Refinement of Steel Castings," *Journal of Metals*, Vol. 19, June 1967, pp. 44-51.

[14] M. Maalekian, “The Effects of Alloying Elements on Steels (I),” *Christian Doppler Laboratory for Early Stages of Precipitation*, October 2007.

[15] J. Wallace, “Grain Refinement of Steels,” *JOM,* Vol. 15, No. 5, April 1963, pp. 372-376.

[16] Z. Liu, “Review of Grain Refinement of Cast Metals Through Inoculation: Theories and Developments,” *Metallurgical and Materials Transactions A*, Vol. 48, No. 10, October 2017, pp. 4755-4776.

[17] Y. Itoh, T. Okajima, and K. Tashiro, “On Refining of Solidification Structure of Ferritic Stainless Steel by Vibration Method,” *ISIJ International,* Vol. 21, No. 6, January 1981, pp. 397-404.

[18] A. Abugh and I. Kuncy, “MICROSTRUCTURE AND MECHANICAL PROPERTIES OF VIBRATED CASTINGS AND WELDMENTS: A REVIEW JESR,” *Journal of Engineering Studies and Research,* Vol. 19, No. 1, 2013, pp. 7-12.

[19] X. Chen, H. Zhong, C. Song, and Q. Jie, “Effect of Forced Convection on Grain Refinement of S32205 Duplex Stainless Steel,” *Advanced Materials Research,* Vol. 683, April 2013, pp. 626-30.

[20] H. Takeuchi, H. Mori, Y. Ikehara, T. Komano, and T. Yanai, “The Effects of Electromagnetic Stirring on Solidification Structure of Continuously Cast SUS43O Stainless Steel Slabs,” *ISIJ International,* Vol. 21, No. 2, January 1981, pp. 109-116.

[21] Y. Itoh, T. Okajima, H. Maede, and K. Tashiro, “Refining of Solidification Structures of Continuously Cast Type 430 Stainless Steel Slabs by Electromagnetic Stirring,” *ISIJ International,* Vol. 22, No. 3, January 1982, pp. 223-229.

[22] X. Wu, Y. Yang, J. Zhang, G. Jia, and Z. Hu, “Structure Characteristics in Industrially Centrifugally Cast 25Cr20Ni Stainless Steel Tubes Solidified under Different Electromagnetic Field Intensity,” *JMEP,* Vol. 8, No. 5, October 1999, pp. 525-530.

[23] S. Zhou, H. Li, and J. Rao, “Effect of electromagnetic stirring on solidification structure of austenitic stainless steel in horizontal continuous casting,” *China Foundry*, Vol. 4, No. 3, 2007, pp. 198-201.

[24] S. Zhou, C. Bai, Y. Lei, Z. Ren, P. Cao, and Z. Yang, “Effect of low-frequency rotary electromagnetic-field on solidification structure of continuous casting austenitic stainless steel,” *J. Cent. S. Univer. Technol.*, Vol. 16, No. 3, June 2009, pp. 360-364

[25] Y. Xu, E. Wang, Z. Li, and A. Deng, “Effects of vertical electromagnetic stirring on grain refinement and macrosegregation control of bearing steel billet in continuous casting,” *J. Iron Steel Res. Int.*, Vol. 24, No. 5, May 2017, pp. 483-489.

[26] N. Tyas, “Grain refinement of austenitic stainless steel welds to facilitate ultrasonic inspection,” *Dissertation at University of Cambridge*, May 2000.

[27] D. Siafakas, T. Matsushita, Å. Lauenstein, J. Ekengård, and A. Jarfors, “The Influence of Deoxidation Practice on the As-Cast Grain Size of Austenitic Manganese Steels,” *Metals*, Vol. 7, No. 6, May 2017, ID 186.

[28] D. Siafakas, “On deoxidation practice and grain size of austenitic manganese steel,” *Thesis at Jönköping University*, 2017.

[29] C. Van der Eijk et al., “Grain size control in steel by means of dispersed non-metallic inclusions – GRAINCONT,” *European Commission*, 2011.

[30] R. Tuttle, “Solidification Based Grain Refinement in Steels,” *Office of Naval Research*, July 2009.

[31] F. Pan et al., “Review: Effects of Rare Earth Metals on Steel Microstructures,” *Materials*, Vol. 9, No. 6, May 2016, ID 417.

[32] R. Tuttle, “Solidification Based Grain Refinement in Steels,” *Office of Naval Research*, July 2010.

[33] C. Van der Eijk, Ø. Grong, F. Haakonsen, L. Klobeinsen, and G. Tranell, “Progress in the Development and Use of Grain Refiner Based on Cerium Sulfide or Titanium Compound for Carbon Steel,” *ISIJ International*, Vol. 49, No. 7, January 2009, pp. 1046-1050.

[34] G. Pervushinh and H. Suito, “Effect of Primary Deoxidation Products of Al_2O_3, ZrO_2, Ce_2O_3 and MgO on TiN Precipitation in Fe–10mass%Ni Alloy,” *ISIJ International*, Vol. 41, No. 7, January 2001, pp. 748-756.

[35] S. Lekakh, J. Ge, V. Richards, R. O’Malley, and J. TerBush, “Optimization of Melt Treatment for Austenitic Steel Grain Refinement,” *Metallurgical and Materials Transactions B*, Vol. 48, No. 1, February 2017, pp. 406-419.

[36] A. Greer, “Grain refinement of alloys by inoculation of melts,” *Philos. Trans. Royal Soc. A*, Vol. 361, No. 1804, March 2003, pp. 479-495.

[37] E. Dahle, “Grain Refinement of High Alloyed Steel With Cerium Addition,” *Thesis at Norwegian University of Science and Technology*, July 2011.

[38] C. Van der Eijk, J. Walmsley, O. Grong, and O. Klevan, “Grain refinement of fully austenitic stainless steels using a Fe-Cr-Si-Ce master alloy,” *Electric Furnace & Process Technology Conferences*, November 2001, pp. 51-60.

[39] M. Mizumoto, S. Sasaki, T. Ohgai, and A. Kagawa, “Development of new additive for grain refinement of austenitic stainless steel,” *Int. J. Cast Metal Res.*, Vol. 21, No. 1-4, August 2008, pp. 49-55.

[40] C. Wang et al., “Grain Refining of 409L Ferritic Stainless Steel Using Fe-Ti-N Master Alloy,” *Metallurgical and Materials Transactions A*, Vol. 41, No. 7, July 2010, pp. 1616-1620.

[41] D. Gaskell, “Reaction Equilibria in Systems Containing Components in Condensed Solution,” *Introduction to the Thermodynamics of Materials*, Taylor & Francis, New York, 2008, pp. 283-292, 450-455.

[42] J. Dantzig and M. Rappaz, “Nucleation,” *Solidification*, Taylor & Francis, Italy, 2009, pp. 249-285.

[43] B. Chalmers, “Nucleation,” *Principles of Solidification*, Wiley, New York, 1964, pp. 62-90.

[44] M. Flemings, “Nucleation and Interface Kinetics,” *Solidification Processing*, McGraw-Hill, New York, 1974, pp. 290-327.

[45] W. Kurz and D. Fisher, “Solidification Microstructure: Cells and Dendrites,” *Fundamentals of Solidification*, Trans. Tech. Publications, Switzerland, 1986, pp. 21-96.

[46] B. Bramfitt, “The Effect of Carbide and Nitride Additions on the Heterogeneous Nucleation Behavior of Liquid Iron,” *Metallurgical Transactions*, Vol. 1, No. 7, July 1970, pp. 1987-1995.

[47] S. Lekakh and N. Medvedeva, “Ab initio study of Fe adsorption on the (001) surface of transition metal carbides and nitrides,” *Computational Materials Science*, Vol. 106, August 2015, pp. 149-154.

[48] T. Inada, “TiN Inclusion Formation during the Solidification of Stainless Steel,” *Thesis at Massachusetts Institute of Technology*, June 1999.

[49] J. Hunt, “Steady state columnar and equiaxed growth of dendrites and eutectic,” *Materials Science and Engineering*, Vol. 65, No. 1, July 1984, pp. 75-83.

[50] J. Park, “Effect of inclusions on the solidification structures of ferritic stainless steel: Computational and experimental study of inclusion evolution,” *Calphad*, Vol. 35, No. 4, December 2011, pp. 455-462.

[51] M. Harris, O. Adaba, S. Lekakh, R. O’Malley, and V. Richards, “Improved Methodology for Automated SEM/EDS Non-Metallic Inclusion Analysis of Mini-Mill and Foundry Steels,” *AISTech Proceedings*, May 2015, pp. 3315-3325.

VITA

Dustin Alan Arvola was born in Fort Wayne, Indiana. Dustin participated in three internships within the steel industry during his undergraduate studies at Trine University. He was named by the Association for Iron and Steel Technology (AIST) as a Steel Premier Scholarship recipient in 2015. After graduating summa cum laude with a Bachelor of Science in Mechanical Engineering from Trine University in May 2016, Dustin decided to pursue his passion of cast metals by continuing his education.

Dustin began his master's degree at Missouri University of Science and Technology in August 2016. His research topic was solidification-based grain refinement of austenitic stainless steels through the Peaslee Steel Manufacturing Research Center (PSMRC) under the guidance of Dr. Ronald O'Malley, Dr. Simon Lekakh, and Dr. Laura Bartlett. During his time as a graduate research assistant, he designed and cast nearly one ton of stainless steel material for research purposes. He also authored a publication in conference proceedings and two journal articles.

While pursuing his degree, Dustin also participated in Material Advantage, American Foundry Society (AFS), Association for Iron and Steel Technology (AIST), Alpha Sigma Mu, and Council of Graduate Students. Dustin earned his Master of Science in Metallurgical Engineering from Missouri S&T in July 2018.